Growth, Characterization and Measurement of Epitaxial Sr_2RuO_4 Thin Films

Jing Cao

Hughes Hall, University of Cambridge

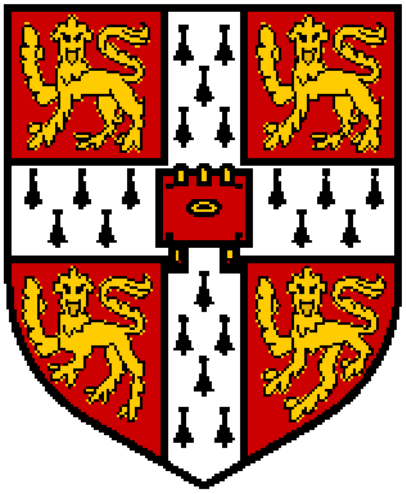

A dissertation submitted for the degree of Doctor of Philosophy at the

University of Cambridge

2017, June

Contents

Preface

This dissertation is submitted for the Degree of Philosophy in the University of Cambridge. The work has been carried out in the Department of Materials Science and Metallurgy under the supervision of Prof Mark Blamire since October 2013. This dissertation is the result of my own work and includes nothing which is the outcome of work done in collaboration except as specified in the text. No part of the work has been or is being submitted for any other degree, diploma or qualification at this or any other university. The dissertation is within the limit of 60,000 words.

Some of the main results in this thesis that have been published as paper or undergoing submission process are as follows:

Cao J, Massarotti D, Vickers M, Kursumovic A, Di Bernardo A, Robinson J, Tafuri F, Driscoll J, Blamire M, et al. Enhanced localized superconductivity in Sr_2RuO_4 thin film by pulsed laser deposition. Superconductor Science and Technology. 2016;29(9):095005.

J Cao, KHL Zhang, D Pingstone, VK Lazarov, A Kursumovic, JL MacManus-Driscoll, MG Blamire. Partial Superconducting Sr_2RuO_4 Thin Films on Nb-STO by Pulsed Laser Deposition. *In preparation.*

August, 2017
Cambridge, UK
Jing Cao

Abstract

In this thesis, the growth of c-axis oriented Sr_2RuO_4 thin films using pulsed laser deposition and their electrical transport properties are systematically discussed. The deposition and optimization process involved several progressive steps. Specifically, the first focus was on the Sr_2RuO_4 phase optimization in films grown on lattice-matched $(LaAlO_3)_{0.3}(SrAl_{0.5}Ta_{0.5}O_3)_{0.7}$ (LSAT) substrates. Film composition was found to be greatly influenced by changes in oxygen pressure, substrate temperature, target to substrate distance, and laser fluence. High oxygen pressure, low substrate temperature, large target to substrate distance, and high laser fluence increased the tendency to form the Ru-rich $SrRuO_3$ phase in the film. The second focus was on improving the electrical transport properties of Sr_2RuO_4 from metal-insulating to fully metallic and eventually to superconducting behavior.

It was observed that the full width at half maximum (FWHM) of the Sr_2RuO_4 (006) rocking curves in x-ray diffraction (XRD) scan was related to the quality of the electrical transport response. By fine tuning the deposition parameters to obtain low FWHM values, the electrical transport behavior of the Sr_2RuO_4 thin films was consistently improved from metal-insulating to fully metallic. In addition, localized superconductivity with enhanced superconducting transition temperature T_c onset was also observed among the fully metallic film. An in-depth study of the XRD results in fully metallic films indicated the existence of defects (intergrowths) along the c-axis direction, which caused localized c-axis tensile strain. The existence of structural defects within the film was likely to be responsible for the fact that only localized superconductivity was observed in the films. Furthermore, the enhanced superconducting transition temperature (T_c) relative to bulk single crystals is likely to be associated to localized strain in the film.

Finally, Nb doped $SrTiO_3$ substrates were used to achieve better quality growth of partial superconducting Sr_2RuO_4 thin films. Sr_2RuO_4 films grown on Nb doped $SrTiO_3$ substrates had smaller FWHM values and lower level of c-axis tensile strain compared to those on LSAT substrates. Various partially superconducting films with different

thicknesses and different superconducting T_c values are presented, and correlations between fabrication process, film crystalline quality as well as transport properties are discussed. This work provides better understanding of the importance of maximizing crystalline quality by delicate fine tuning of PLD deposition parameters to achieve high quality superconducting films.

Acknowledgement

My most sincere gratitude to my supervisor, Prof. Mark Blamire, who has offered me the chance to study in device materials group. I am so grateful for his patient guidance and encouragement on research and paper writing. It is a big pleasure to work with Dr. Jason Robinson. I benefited a lot from the delightful discussions with him. I would like to thank Dr. Angelo Di Bernardo, who systematically trained me in the early stage of my research. I would also like to thank Prof. Judith Driscoll for helping me avoid many detours in PLD. I would also like to show my sincere acknowledgement to Dr. Ahmed Kursumovic, who helped me overcome many difficulties in thin film growth and solve equipment problems. I would also like to thank Mary Vickers for many in-depth XRD knowledge. I would also like to thank my examiners Prof Zoe Barber from University of Cambridge and Prof Susannah Speller from University of Oxford, for giving me many helpful advice and suggestions to better shape my thesis.

Sincere thanks to all DMG colleagues, especially: Dr. Nadia Stelmashenko, for her clear-cut trainings; Dr. David Gustafson, for helping with the mini-cryofree; Dr. Prasanta Muduli, for many helpful discussions; Dr. Sam Crossley, who helped me build the inductance probe; Dr. Eun-Mi Choi, for the helpful XRD discussions; Dr. Shaoqun Jiang, for her nice cooking during many busy nights; help from Dr. Yuanzhou Gu, Dr. Zhuo Feng, and Dr. Wenjing Yan and other members are also appreciated.

This research could not be done without help from external collaborators. I would like to thank Prof. Francesco Tafuri and Dr. Davide Massarotti from Seconda Universita' degli Studi di Napoli and Complesso Universitario Monte Sant'Angelo for helping me with some of the low temperature transport measurements. I would also like to thank Prof. Kelvin Hongliang Zhang (Xiamen University), Dr. D Pingstone and Dr. Vlado Lazarov from University of York for helping me with the STEM characterization.

A big thank you to my family and friends. Thank you for being there and encouraging me when I faced difficulties and also for accompanying me enjoying the beautiful moments in Cambridge. Last but not least, I would like to thank Chinese Scholarship Council (CSC), for supporting my PhD studies in Cambridge.

Chapter 1 Introduction

Superconductivity is not a new concept and has already found applications such as in SQUID (superconducting quantum interference device) magnetometers which are versatile instruments for studying magnetic properties in materials. In our daily lives, superconducting materials are used in applications ranging from healthcare (magnetic resonance imaging) to transportation (maglev). In superconductors, some electrons interact to form Cooper pairs. In most cases, the spin of two electrons in a Cooper pair are aligned antiparallel to each other, and such kind of superconductors are known as spin singlet superconductors. They are the most common type of superconductors known to date, and include for example, the elemental superconductors like Nb, Al, standard alloy superconductors like NbTi, and the high temperature superconductors like $YBa_2Cu_3O_7$.

In a very small minority of superconductors known as the spin triplet superconductors, the spin of electrons in Cooper pairs are thought to be aligned parallel to each other. Theoretically, depending on the angular momentum of the Cooper pairs, spin triplet superconductors can be divided into *p*-wave and *f*-wave. However, spin triplet superconductors are not commonly nor convincingly observed. Considerable attention has been paid to searching and studying for the existence of spin triplet superconductors.

In 1994, a piece of Sr_2RuO_4 single crystal was found to exhibit superconductivity. This has attracted great interest among scientists because Sr_2RuO_4 is potentially a very rare example of an intrinsic *p*-wave spin triplet superconductor[1]. Although Sr_2RuO_4 may not be the only material which could have spin triplet pairing, its simple crystal structure perhaps makes it the best example to understand spin triplet superconductivity [2]. Therefore, it is highly expected that Sr_2RuO_4 could provide answers to many open questions such as whether superconductivity can exist in a spin triplet pairing and how different this is from spin singlet pairing.

So far, a lot of work has been carried out on Sr_2RuO_4, searching for evidence of

spin triplet superconductivity[3, 4]. The most convincing experiments are from nuclear magnetic resonance (NMR) and muon spin relaxation (μSR)[1, 5]. However, there are many more experiments giving some ambiguous results, especially those including the current-voltage characteristics of the interfaces between Sr_2RuO_4 and some other materials[2, 4, 6]. This inconsistency from different experiments has hindered scientists' understanding of Sr_2RuO_4.

One direct reason for the problem is that all the experiments used Sr_2RuO_4 single crystals. During the Sr_2RuO_4 single crystal growth using the floating zone method[7], Ru in the starting material can be easily turned into RuO_4, which is highly volatile[7]. To compensate for the Ru loss, usually an excess of Ru is normally added into the starting materials. Even though, the as-grown Sr_2RuO_4 single crystal rod is still inhomogeneous in terms of composition. It is very common that the outer surface of the Sr_2RuO_4 single crystals is deficient of Ru and the inner core contains Ru metal inclusions[7, 8]. Given the dimension of the as-grown Sr_2RuO_4 single crystal rod, which is normally about 80 mm x 4 mm x 3 mm[7], this has posed a great challenge to sample consistency. Samples for experimental use have to be cleaved from the rod and chosen with care. In most cases, the cleaved surfaces are not smooth, and there are always surface steps[2]. Moreover, there are different surface reconstructions[9] on the cleaved surfaces, which would alter the surface electronic state and lead to poor electrical contact to the *a*-*b* plane[10]. These problems have created many challenges to further processing, making it unfavorable for device fabrication[6, 11], which is important to the probing of the superconducting pairing state of Sr_2RuO_4. Therefore, it is not hard to understand why the previous experiments have ambiguous results.

These problems could be alleviated by using thin films. The growth of superconducting Sr_2RuO_4 thin films would enable in situ-device fabrication. In addition, Sr_2RuO_4 has a perovskite structure, making it an excellent candidate for device integration as it is chemically and structurally compatible with numerous oxides[12]. Furthermore, the good lattice matching between Sr_2RuO_4 with many other superconducting materials eliminates potential interface problems[13]. Thus, a

superconducting Sr_2RuO_4 thin film is highly desirable. Many research groups have devoted a lot of effort to growing superconducting Sr_2RuO_4 thin films, but no satisfactory results in terms of electrical transport properties have been reported to date. Before this work, only one superconducting Sr_2RuO_4 thin film has been reported, with the onset of superconducting transition (T_c) at 0.9 K[14], while the bulk T_c is 1.5 K. The primary challenge lies in the fact that *p*-wave superconductivity is extremely sensitive to impurities and disorder[15]: for example, structural disorders such as planar defects within the range of the *in-plane* coherence length (66 nm)[16] of Sr_2RuO_4 can easily suppress superconductivity[17]. Therefore, most attempts resulted in non-superconducting behavior with varying metal-insulator transition temperatures at low temperatures[17, 18].

This PhD research is primarily aimed at the growth and characterization of c-axis oriented Sr_2RuO_4 thin films using pulsed laser deposition. The detailed study of this thesis will be systematically discussed in the following chapters. Chapter 2 introduces the basic superconductivity theory and some concepts related to this research. Chapter 3 is a systematic literature review on past and current researches on Sr_2RuO_4. As another interesting part, the Sr_2RuO_4-Ru eutectic system was also introduced. Chapter 4 discusses the thin film growth principles, including the pulsed laser deposition technique used throughout the research. Chapter 5 describes all the characterization technique involved in this research. Chapter 6 to 8 are the experimental chapters. Chapter 6 is Sr_2RuO_4 thin film phase optimization and transport optimization. It mainly describes how the deposition parameters affect the film composition, quality and transport. Chapter 7 discusses the superconducting Sr_2RuO_4 thin film grown on LSAT substrate. In this chapter, the low temperature resistance as a function of temperature and current as a function of voltage measurements were performed in collaboration with Prof. Francesco Tafuri and Dr. Davide Massarotti. The equation used in Chapter 7 is discussed in the Appendix. In chapter 8, fabrication of superconducting Sr_2RuO_4 epitaxial thin films was on Nb-STO substrates was discussed. The STEM characterization was carried out in collaboration with Prof. Kelvin Hongliang Zhang,

Dr. D Pingstone and Dr. Vlado Lazarov. Chapter 9 is a summary and outlook based on the present work.

Chapter 2 Physical Theories

Electrical resistance of metals arises from scattering of conduction electrons. As temperature decreases, the scattering of electrons is also reduced due to reduction in the crystal lattice vibration speed and electron speed[19]. Therefore, for many metals/conductors, their resistances gradually decrease with decreasing temperature, approaching the residual resistance at 0 K. Unlike these conventional conductors, below a specific temperature, the *d.c.* resistance of a superconductor drops sharply to zero. This temperature is defined as the critical temperature (T_c) for superconductors. In practice, zero resistance means zero energy dissipation, which can be observed in the form of perpetual current in a superconductor loop.

A more fundamental characteristic of superconductors came in the year of 1933, when W. Meissner and R. Ochsenfeld[20] discovered the Meissner effect. It is the ability of a superconductor to completely expel an external magnetic field. Suppose a superconductor in the superconducting state is placed in a zero external field, and the external field is gradually turned on. According to the Meissner effect, the magnetic field inside the superconductor must be zero. Now consider things the other way. Suppose the superconductor is placed in an external field when it is at the normal state, in this case the magnetic field easily penetrates into the superconductor. However, as the temperature is cooled below the T_c, the magnetic field inside the superconductor is expelled.

The magnitude of the magnetic field that can be expelled by a superconductor is not infinite. When the external magnetic field becomes exceedingly strong that it exceeds the field that the superconductor can tolerate (defined as critical field), the superconductivity is destroyed. In fact, different superconductors behave differently when the applied field approaches the critical field. This is how superconductors are categorized into type I and type II superconductors.

For type I superconductors, the Meissner effect happens when the external magnetic field is lower than the critical field, H_c. Beyond the critical field,

superconductivity is destroyed and the superconductor behaves like a normal metal even though the temperature is still below T_c. On the other hand, type II superconductors behave differently. There are two levels of critical field in type II superconductors. When the external magnetic field is still weak, the Meissner effect is unaffected. Once the external field reaches the lower critical field, H_{c1}, magnetic field can penetrate into the superconductor in the form of vortices. The vortex consists of a region where supercurrent circulates around a small central core which is in the normal state. The magnetic field is able to pass through the superconductor inside the vortex cores, and the circulating supercurrents can screen out the magnetic field from the rest of the superconductor outside the vortex. The superconductor is thus said to be in a mixed state consisted of normal and superconducting regions. The density of the vortices increases as the field increases until the field exceeds the upper critical field, H_{c2}, and superconductivity is destroyed[19]. This process is shown in Figure 2.1.

In other words, superconductivity in type I superconductors is abruptly destroyed when the external magnetic field exceed its critical field. In contrast, for type II superconductor, there is a range of magnetic field from H_{c1} to H_{c2} at which the superconductor is in a mixed state before it is entirely destroyed upon reaching H_{c2}.

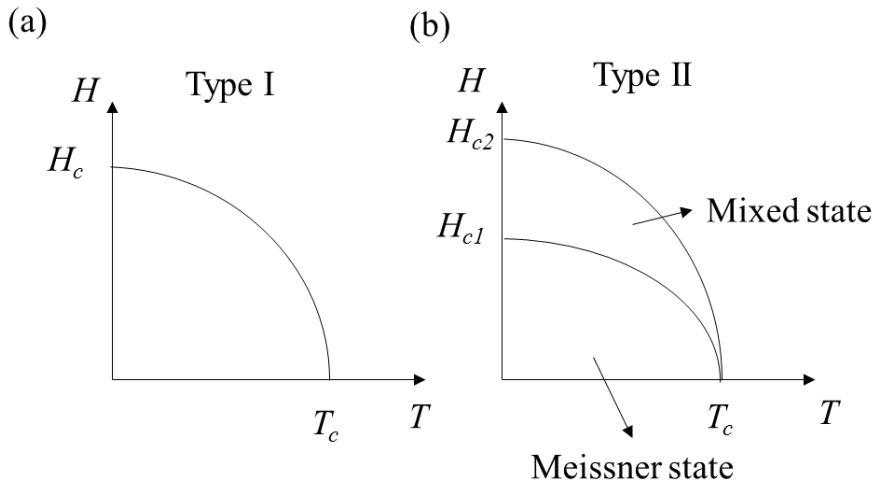

Figure 2.1 The H-T phase diagram of type I and type II superconductors. In type II superconductors the phase below H_{c1} is denoted the Meissner state, while the phase between H_{c1} and H_{c2} is the mixed state[19].

Many theories have been developed around superconductivity ever since its discovery. Here we will not go through all the details or complex derivations, but will mention some key theories and concepts.

2.1 Basic Superconductivity Theory

2.1.1 The Ginzburg-Landau Theory

For superconductors, the abrupt transition from the normal state to the superconducting state is a phase transition, which involves the change in their free energy. Analogous to water and ice which are two different states of the same matter, the normal state and the superconducting state are also different thermodynamic states of the same material. The fact that the transition is spontaneous at zero magnetic field indicates that the superconducting state is a more stable state at low temperatures. It means that under these conditions, the Gibbs free energy of the superconducting state is lower than that of the normal state. This forms the framework of the Ginzburg-Landau theory. Based on this, Ginzburg and Landau made the following postulation[21]:

$$f_s - f_n = \alpha|\psi|^2 + \frac{1}{2}\beta|\psi|^4 \quad (2.1),$$

where f_n and f_s are the free energy density for the normal and superconducting state, separately; α and β both depend on temperature and material. ψ is the wavefunction associated with the macroscopic superconducting state:

$$\psi = |\psi|e^{i\varphi} \quad (2.2),$$

where $\psi\psi^*$ is the density of superconducting electrons, and φ is a spatially varying phase[22]. ψ is also the superconducting order parameter. It is zero when the superconductor is at the normal state ($T > T_c$), but has a finite value at the superconducting state ($T \leq T_c$)[19]:

$$\psi = \begin{cases} 0 & T > T_c \\ \psi(T) \neq 0 & T \leq T_c \end{cases} \quad (2.3).$$

Two important lengths can be derived from the Ginzburg-Landau theory. The first one is the Ginzburg-Landau coherence length ξ[19]:

$$\xi(T) = \xi_0 |\frac{T-T_c}{T_c}|^{-1/2} \quad (2.4),$$

where ξ_0 is the coherence length at zero temperature. $\xi(T)$ can be understood as the length over which the order parameter can vary without unwanted energy increase. For example, in the situation where a superconductor is placed next to a normal metal, the order parameter is zero in the normal metal, but non-zero in the superconductor. Since the superconducting transition is a second order phase transition, the order parameter should be continuous. In this sense, the order parameter gradually changes from zero in the metal to a finite value after a distance ξ into the superconductor. This is illustrated in Figure 2.2, where ψ_0 is the value of the order parameter in the superconductor far away from the interface. The value of ψ as a function of distance from metal to superconductor can be found according to equation (2.5). The value of ξ(T) can be obtained from equation (2.4).

$$\psi(\mathrm{x}) = \psi_0 \tanh(\frac{x}{\sqrt{2}\xi(T)}) \quad (2.5)^{[19]}.$$

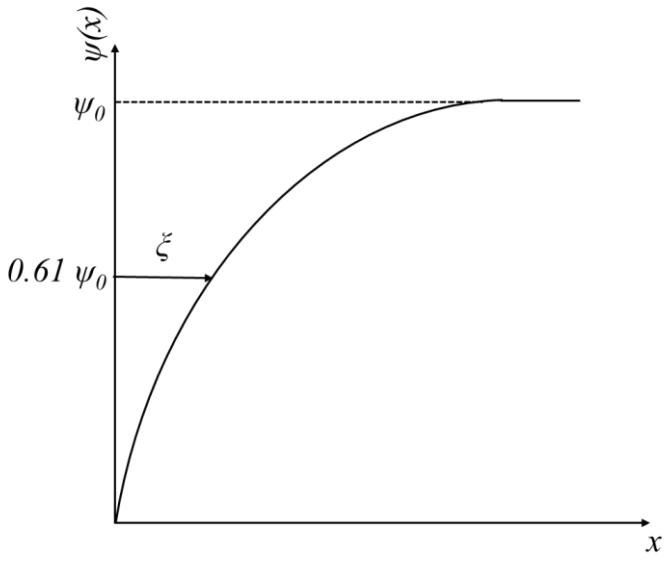

Figure 2.2 Ginzburg-Landau coherence length ξ in the case of a superconductor placed next to a normal metal. *x* is the distance from the normal metal to the superconductor[19].

The Ginzburg-Landau coherence length is an ideal case for superconductors. For a more common situation where a superconductor has impurities, the coherence length

of the superconductor decreases under the influence of impurity scattering. Pippard[23] pointed out that the coherence length of a superconductor in the presence of scattering events is related to the electron mean free path *l*:

$$\frac{1}{\xi} = \frac{1}{\xi_i} + \frac{1}{l} \quad (2.6),$$

where ξ_i is the coherence length of a superconductor in an ideal case, ξ is the actual coherence length of the superconductor in the presence of impurities.

The second important length scale is the Ginzburg-Landau penetration depth. Although a superconductor can expel an external magnetic field up to a finite value, the magnetic field can in fact penetrate into the superconductor by a certain depth, as shown in Figure 2.3. This is defined as the superconducting penetration depth: λ. For instance, if a superconductor with the thickness *d* ($d > \lambda$) is placed in a magnetic field, from the surface to the center of the superconductor, the magnetic field decayed exponentially to zero by the following equation[19]:

$$B_z(x) = B_z(0)e^{-\frac{x}{\lambda}} \quad (2.7),$$

where $B_z(0)$ is the external field at the surface, $B_z(x)$ is the magnetic field that penetrates into the superconductor, and *x* is the distance into the superconductor from its surface.

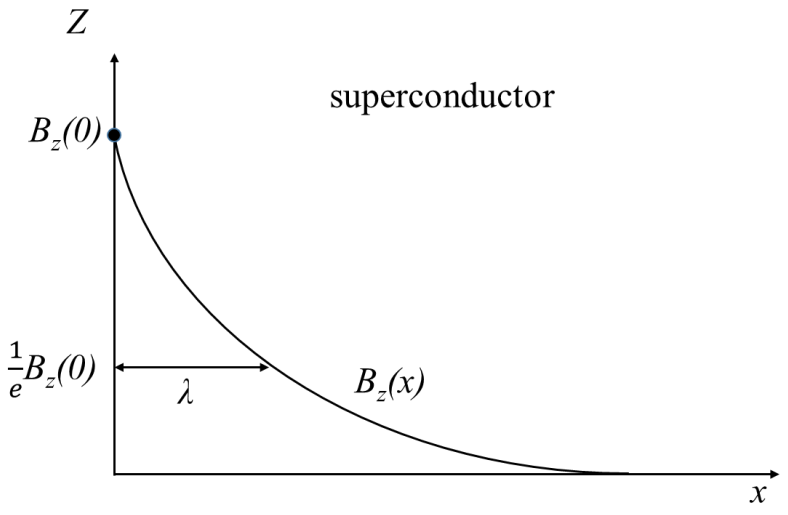

Figure 2.3 Illustration of superconducting penetration depth in one dimensional case. The *x*-*z* plane denotes the superconductor[24].

2.1.2 BCS Theory

Today the much more widely used theory is the BCS theory, provided by J. Bardeen, L. Cooper, and R. Schrieffer[25, 26]. The basic idea of the BCS theory is that the effective force between two electrons can be attractive rather than repulsive, and thus electrons can form into pairs in the superconducting state. This counter-intuitive idea arises from the interaction between electrons and the lattice. An electron can give momentum away to the lattice in the form of phonons, while another electron can absorb the phonon via the lattice. In this way, we can say that the electron interacts with another electron by exchanging phonons via the mediation of lattice.

The interaction can be intuitively understood in the following way. Owing to the fact that ions are much heavier than electrons, the elastic relaxation rate of ions are slower compared to electrons. Suppose an electron travelling in the lattice interacts with the surrounding ions, polarizing the ions in the process. This polarization inevitably 'distorts' the lattice. As electron travels much faster than the elastic relaxation rate of lattice distortion, there would be enough time for a second electron to interact with the ions, which were polarized by the first electron. In this sense, the two electrons are coupled into a pair, which is called the Cooper pair.

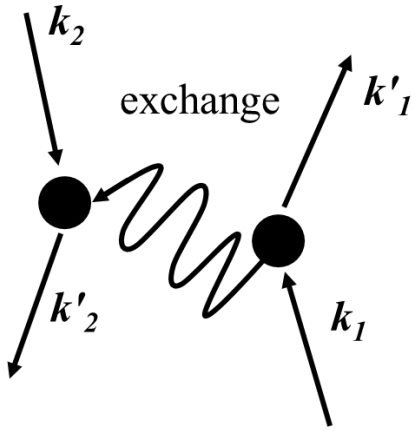

Figure 2.4 Electron-electron interactions via phonons[24].

In other words, an electron with the wave vector $\boldsymbol{k_1}$ in the crystal lattice can emit a phonon described by another wave vector $\boldsymbol{q}$, and thus its new momentum $\boldsymbol{k_1}'$ is given by $\boldsymbol{k_1}' = \boldsymbol{k_1} - \boldsymbol{q}$. This emitted phonon is then absorbed by a second upcoming electron $\boldsymbol{k_2}$,

and the new momentum $\boldsymbol{k_2}'$ is $\boldsymbol{k_2}' = \boldsymbol{k_2} + \boldsymbol{q}$. It is clear that $\boldsymbol{k_1} + \boldsymbol{k_2} = \boldsymbol{k_1}' + \boldsymbol{k_2}'$[19]. This process is shown in Figure 2.4.

Electrons obey both the Pauli exclusion and the Coulomb repulsion principle, therefore, the force between electrons is a combination under the two. The interaction force can be written as:

$$V_{eff} = |g_{eff}|^2 \frac{1}{\omega^2 - \omega_D{}^2} \quad (2.8),$$

where ω is the frequency of the phonons and ω_D is the Debye frequency of the phonons, g_{eff} is the coupling constant[19]. This interaction is attractive when $\omega < \omega_D$.

As a matter of fact, not all electrons in the superconductor participate in the pairing process. This attractive interaction only occurs near the Fermi surface, therefore only electrons with the energy close to the Fermi surface contribute to the superconductivity, while those far from the Fermi surface do not.

The difference between superconducting state and normal state (in terms of critical temperature, critical magnetic field, or critical current) indicated the existence of an energy gap (Δ). It is found that when the superconductor is in the normal state, there is no energy gap and the density of states ($g(\epsilon)$) is continuous up to the Fermi level; however, when the superconductor is in its superconducting state, there is an energy gap close to its Fermi level, and the density of states is changed, as shown in Figure 2.5. This energy gap can be understood as the minimum amount of energy to break a Cooper pair and create excitations. It is temperature dependent: it reaches a maximum when the temperature is zero, and is zero when temperature is at T_c, as shown in Figure 2.6. The BCS theory accurately gives the value of energy gap for a wide range of superconductors at $T = 0$:

$$\Delta(0) = 1.76 k_B T_c \quad (2.9)[21],$$

and another approximation when the temperature is close to T_c.

$$\frac{\Delta(T)}{\Delta(0)} = 1.74\left(1 - \frac{T}{T_c}\right)^{1/2} \quad (2.10)[21].$$

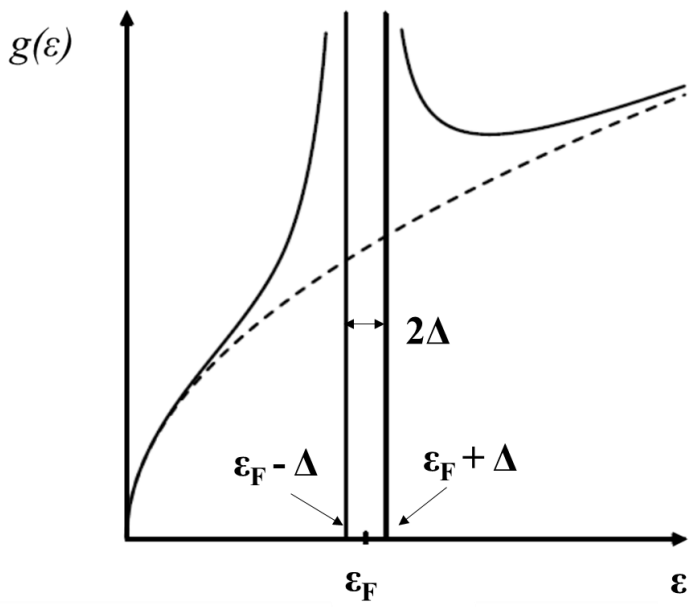

Figure 2.5 The BCS energy gap and density of states. The dashed line denotes the normal state, while the solid line denotes the superconducting state. *g(ε)* stands for the density of states and ε_F for the Fermi energy. The actual energy gap is very small and normally of the order of ~ 10^{-4} eV. The size of the energy gap in this plot is exaggerated in order to be clearly seen[19].

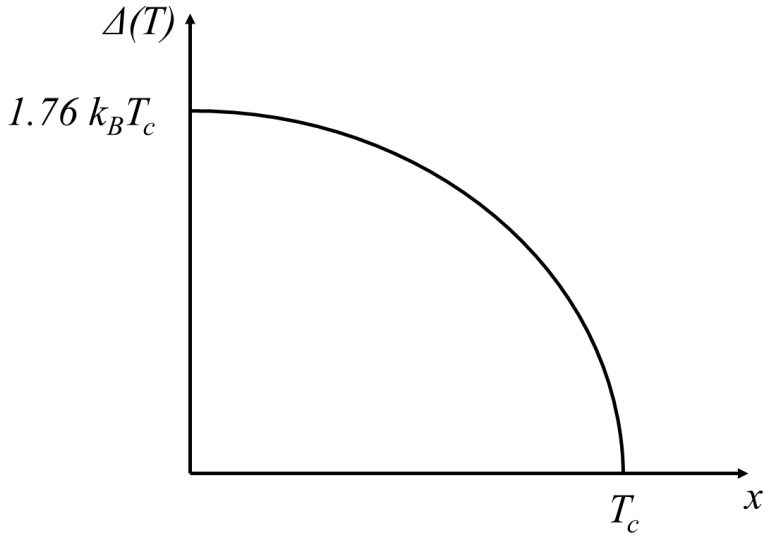

Figure2.6 Superconducting energy gap as a function of temperature[19].

Elementary particles can be divided into fermions and bosons according to their spin. Spin is a particle's angular momentum. Particles with integer spins are bosons, and those with half-integer spins are fermions. In this sense, electrons are fermions, and all fermions follow Pauli Exclusion Principle, which means no two identical fermions exist in the same quantum state. On the other hand, Cooper pairs are bosons, which means, unlike fermions, there is no limit to the number of Cooper pairs occupying the same quantum state. Therefore, all Cooper pairs are in the same quantum states and have the same wave function.

Undoubtedly the BCS theory has contributed very much to our understanding of superconductivity. In fact, these earlier theories are not mutually exclusive. It was realized by Gor'kov[27] that some part of the Ginzburg-Landau theory is equivalent to the BCS theory. For example, the Ginzburg-Landau order parameter ψ is not only directly related to the wavefunction for the Cooper pairs, but also directly proportional to the gap parameter Δ. Soon with the discovery and synthesis of new superconductors, it was found that not all superconductors conform to the traditional superconducting theories, and therefore new branches of superconductivity were defined - so-called unconventional superconductivity.

2.2 Unconventional Superconductivity

The BCS theory has paved the road for our present understanding of superconductivity, which explains well the conventional superconductors like Nb, Al, and technological superconductors like NbTi, Nb_3Sn, etc. However, for later discoveries like the high-temperature superconducting cuprate[28], the heavy-fermion compounds[29], the organic superconductors[30], Sr_2RuO_4[31], and the pnictide superconductors[32], the BCS theory alone is not adequate. These superconductors are therefore named as unconventional superconductors.

Unconventional superconductivity has been studied for more than twenty years, and despite many promising results, scientists so far have yet to find a clear origin or a satisfactory explanation for unconventional superconductivity. One reason for this is that the materials displaying unconventional superconductivity normally have very complex composition and complicated structures, which creates many difficulties for experimental control or theoretical modelling. Nevertheless, there are several characteristics that can help us distinguish a conventional superconductor and an unconventional superconductor. Therefore, in this section, we shall go through a very brief introduction of unconventional superconductivity.

We first introduce the concept of parity, which can be associated with the symmetry of a system under reflection. In most cases, a system or a fundamental particle can be represented by a function, f. Under reflection transformation, if $f(x) = f(-x)$, the system is said to have even parity; if $f(x) = -f(-x)$, the system is said to have odd parity.

Superconducting Cooper pairs are described by the wavefunction ψ, which has both an orbital part φ and a spin part σ:

$$\psi = \varphi \times \sigma \tag{2.11}$$

Electrons are fermions. By Fermi statistics, the wavefunction is antisymmetric under electron exchange. This means the orbital (φ) and spin part (σ) of the wavefunction have opposite exchange symmetries. To be specific, if the orbital part (φ) is symmetric, i.e. the orbital wavefunction is even parity, then the spin part (σ) is

antisymmetric. In this case, the angular momentum is an even number: 0, 2, …, corresponding to the *s*-wave, *d*-wave superconductor. In addition, there is only one state in this case and the electrons spins are antiparallel as shown below:

$$\sigma = \frac{1}{\sqrt{2}}(|\uparrow\downarrow\rangle - |\downarrow\uparrow\rangle) \quad (2.12)^{[19]},$$

where ↑ means the electron is spin up and ↓ means spin down. It is hence called the spin singlet state and the total spin S = 0.

If the orbital part (φ) is antisymmetric, which means the orbital wavefunction is odd parity, then the spin part (σ) is symmetric. In this case, the angular momentum is odd number: 1, 3, …, corresponding to the *p*-wave, *f*-wave superconductor. In addition, there are three possible states in this case and the total spin S = 1. This state is thus called the spin triplet state. In this state, the electron spins are parallel aligned, which means the electrons can both have spins up, or spins down, or in a superposition of spin up and spin down state[19] as shown equation 2.13. Table 2.1 is a summary of the superconducting pairing states.

$$\sigma = \begin{cases} |\uparrow\uparrow\rangle \\ |\downarrow\downarrow\rangle \\ \frac{1}{\sqrt{2}}(|\uparrow\downarrow\rangle + |\downarrow\uparrow\rangle) \end{cases} \quad (2.13)$$

Almost all the superconductors known to date, be it conventional or unconventional, are spin singlet. For example, the most familiar elemental superconductors like Nb are *s*-wave superconductors, while cuprates are widely accepted as *d*-wave. Spin triplet superconductors are rarely seen. There has always been the query searching for spin-triplet superconductivity with the question of how it differs from the spin-singlet superconductivity. To date, it is generally agreed that the heavy-fermion compound UPt_3[33, 34] is a spin-triplet superconductor. Another very promising candidate as a triplet superconductor is Sr_2RuO_4, which will be discussed in Chapter 3 and the rest of the thesis.

As mentioned before, the superconducting transition is a phase transition. In fact, a phase transition is always accompanied by one or more symmetry breakings. For example, as the temperature decreases, the phase of Fe can change from γ-Fe to α-Fe.

γ-Fe is a face centered cubic while α-Fe is a body centered cubic[35, 36]. The two phases have different symmetry groups defined by translations, rotations and reflection of the crystal lattice. Similarly, superconducting transition is also accompanied by spontaneous symmetry breaking. As a matter of fact, unconventional superconductors undergo more symmetry changes compared to conventional superconductors as the temperature goes below T_c [19, 37]. This part is beyond the scope of this study and will not be discussed.

Orbital angular momentum	Parity of orbital wavefunction	Spin state	example
s-wave	even	Singlet	Nb, Al, etc
p-wave	odd	Triplet	Sr_2RuO_4
d-wave	even	Singlet	cuprates
f-wave	odd	Triplet	UPt_3

Table 2.1 Superconducting states and their pairing states[4, 19]. *s*-wave superconductor is the so-called conventional superconductor.

Apart from that, in conventional superconductors, the non-magnetic scattering has little effect on superconductivity[4]. On the other hand, in unconventional superconductors, the scattering can totally destroy the superconductivity if the superconducting coherence length is longer than the mean free path[19].

Finally, it should be noted that spin triplet Cooper pairs also exist in some superconductor/ferromagnet/superconductor hybrid structures. Before discussing about the hybrid structures, it is important to understand the basic physical mechanisms of ferromagnetism. Ferromagnetism is the result of electron spin and Pauli exclusion principle. When two atoms with unpaired electrons meet, the orbitals of the unpaired outer valence electrons would overlap. According to the Pauli exclusion principle, only two electrons with opposite spins can occupy the same orbital, while those with parallel spins cannot. Therefore, for electrons with parallel spin, they can only occupy different orbitals. In this sense, the distance between electrons with parallel spin is bigger than

the distance between electrons with antiparallel spin. This means the Coulomb repulsion for electrons with parallel spin is smaller compared to electrons with opposite spins because they are further apart. Thus the exchange energy, which is the energy due to the repulsion between the two electrons is minimized, and electrons with parallel spins are more stable[38]. Hence, in ferromagnetic materials, two atoms prefer to have their electron spins in parallel direction (e.g. preventing the two electrons to form an orbital like in the case of opposite spin, which will result in strong coulomb repulsion and instability).

In relation to superconductor, specifically in spin singlet superconductors, the spin of electrons in the Cooper pairs is antiparallel. When a spin singlet superconductor is next to a ferromagnet, the spin singlet Cooper pairs decay rapidly inside the ferromagnet, with a decay length usually no more than 10 nm[39]. This is because of the exchange interaction mentioned above in the ferromagnet, which tends to align electron spins parallel to each other and thus break the phase coherence of the spin singlet Cooper pairs. In Figure 2.7 as shown by the oscillation curve, the decay length of the supercurrent in singlet junctions (Nb/Co/Nb) was simulated to give the decay length of approximately 10 nm.

To achieve a long decay length, spin triplet Cooper pairs (electron spins are parallel aligned) have to be generated in the ferromagnet, which do not decay through the exchange field[39, 40]. A straightforward approach to achieve this would be a spin triplet superconductor/ferromagnet junction[4]. However, no spin triplet superconductor is available to date to conduct such research.

An indirect way would be to generate spin triplet Cooper pairs via some spin singlet superconductor/ferromagnet/spin singlet superconductor hybrid structures. In order to obtain spin triplet Cooper pairs in those structures, the singlet Cooper pairs in the interface next to the superconductor side needs to be exposed to an inhomogeneous magnetization on the ferromagnet side[41], or in a variant, spin mixing and magnetic disorder at the interface[39, 42]. The details of this mechanism involves non trivial physics and will not be discussed in the present work.

An example is the Nb/Ho/Co/Ho/Nb structure[43], where Nb is an s-wave superconductor, Ho and Co are both ferromagnets. The magnetization of the two Ho layers were made non-collinear, so as to provide the necessary magnetization inhomoegeneity mentioned above for the spin triplet Cooper pairs. As indicated by the blue dots in Figure 2.7, the characteristic voltage of such junctions clearly demonstrates a much longer decay length of the supercurrent across the ferromagnet (Co), as compared with the Nb/Co/Nb control sample (the oscillation curve). This clearly indicates the existence of spin triplet Cooper pairs in the ferromagnet.

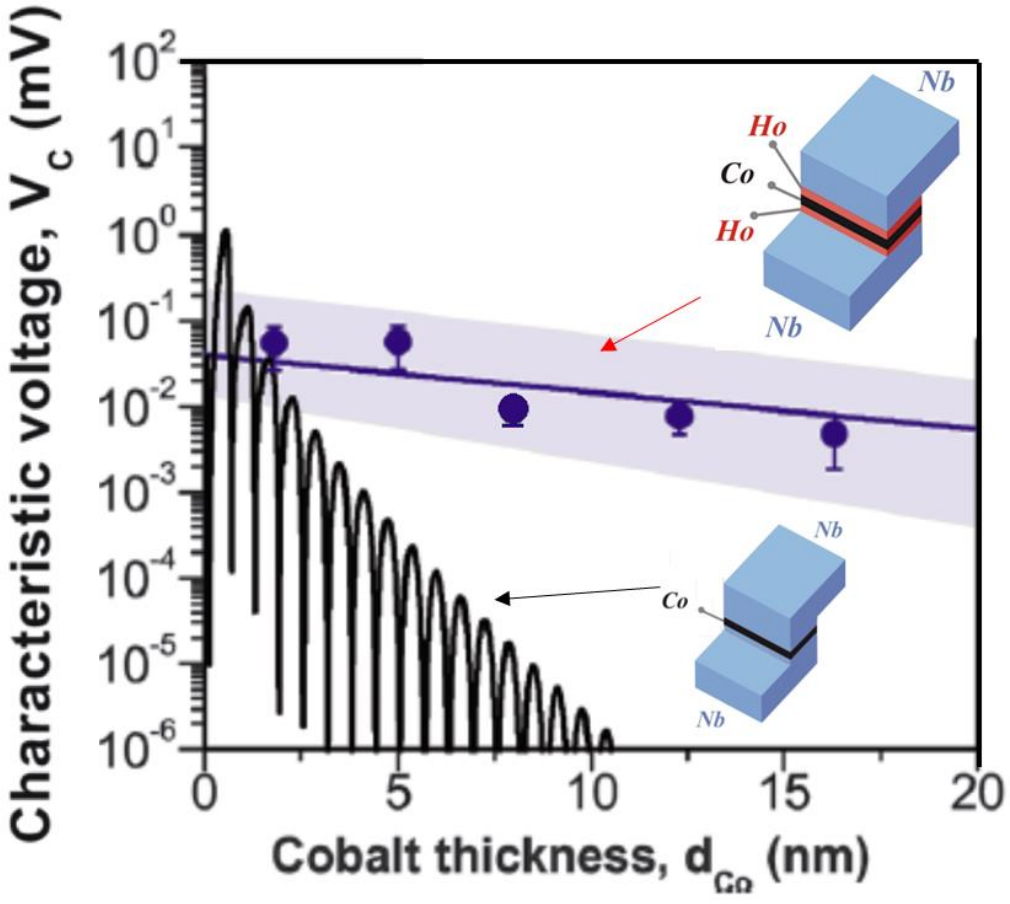

Figure 2.7 The decay of the characteristic voltage in Nb/Ho/Co/Ho/Nb junctions as a function of the Co thickness at 4.2 K. The oscillation curve is the theoretical fitting of the control data of Nb/Co/Nb[43].

Chapter 3 An Introduction to Sr_2RuO_4

In 1958, J. J. Randall and R. Ward synthesized an A_2BO_4 type new compound – Sr_2RuO_4[44]. There were not many studies on Sr_2RuO_4 until after the discovery of high-T_c superconductors[28], when scientists were looking for suitable substrates to grow high-T_c superconducting films. In 1992, F. Lichtenberg found that Sr_2RuO_4 is a very good substrate due to its high electrical conductivity and good lattice matching with high-T_c superconductors[13, 45]. Due to this finding, Sr_2RuO_4 gained some attention from the superconducting community. The big turning point came in 1994, when Y. Maeno measured the resistance of a piece of Sr_2RuO_4 single crystal and found a clear superconducting transition right below 1 K[31]. Since then, many research groups have been investigating the superconductivity in Sr_2RuO_4.

Back then, most of the attention was focused on its close structural similarity to the high-T_c superconducting cuprates[28]. Being the only copper free layered perovskite at that time, Sr_2RuO_4 seemed to be a perfect example to study the role of copper in the cuprates and understand the superconducting mechanism. Very soon after that, scientists realized that the superconductivity in Sr_2RuO_4 is not like that in the cuprates, but a different new phenomenon. In 1995, Rice and Sigrist suggested that the spin triplet pairing state[46] might be responsible for the superconductivity in Sr_2RuO_4. Most superconductors known to date are spin singlet paired. Spin triplet superconductivity is very rare and unusual. This promising aspect of Sr_2RuO_4 has made it one of the hottest topics ever since. At the moment, direct proof that Sr_2RuO_4 is a spin triplet *p*-wave superconductor has not been seen[1, 5], and there are many ambiguous results[2, 6]. However, many experimental and theoretical works have indirectly confirmed that, at least, Sr_2RuO_4 is an unconventional superconductor[3, 4]. Thus, considerable work has to be done in this aspect to gain further understanding of the material.

In this chapter, a systematic introduction on the progress and the established results about the materials science and electronic properties of Sr_2RuO_4 is presented.

Specifically, section 3.1 describes the normal state of Sr_2RuO_4, including its crystal structure and transport properties. Section 3.2 describes the superconducting state of Sr_2RuO_4, including its sensitivity to defects, and current review of some important publications on the discussion of superconducting mechanism of Sr_2RuO_4. Section 3.3 introduces the most widely used fabrication methods of Sr_2RuO_4, including floating zone method used to grow single crystals, and pulsed laser deposition to grow thin films. Section 3.4 briefly presents another material system related to Sr_2RuO_4, which is the Ru-Sr_2RuO_4 eutectic system. Section 3.5 discusses the pressure effects on the T_c of Sr_2RuO_4 single crystals.

3.1 Normal State of Sr_2RuO_4

3.1.1 Crystal Structure

It is important to understand the crystal structure of Sr_2RuO_4 before going into any details of its properties. Sr_2RuO_4 has a body-centered tetragonal structure with I4/mmm space group symmetry[31]. This structure is very similar to that of $La_{2-x}Ba_xCuO_4$ as shown in Figure 3.1(a). Sr_2RuO_4 is a member of a series of Ruddlesden-Popper phases: $Sr_{n+1}Ru_nO_{3n+1}$, where n represents the number of octahedra in one unit cell as shown in Figure 3.1(b). Members in the $Sr_{n+1}Ru_nO_{3n+1}$ series share similar crystal structures[47]. Two most widely studied materials are Sr_2RuO_4 (n=1) and $SrRuO_3$ (n = ∞). However, the transport properties of the two are remarkably different. While both materials are metallic at room temperature, Sr_2RuO_4 is superconductor below about 1.5 K, while $SrRuO_3$ is ferromagnetic below about 150 K[48]. The fact that both ferromagnetic and superconducting properties are observed within the same Ruddlesden-Popper series is one of the reasons for the speculation that triplet parity is possible in Sr_2RuO_4. At the moment, not many studies are conducted on the rest of the members in the $Sr_{n+1}Ru_nO_{3n+1}$ series[49, 50], and their properties are not clear at the moment, so we are not going to discuss them here.

Sr_2RuO_4 is both structurally and chemically stable. There is little evidence for any

structural distortion, and the temperature variation of the lattice parameters are comparable with that of $YBa_2Cu_3O_{7-\delta}$[45], making it an appropriate substrate for film deposition. At room temperature, the *in-plane* lattice parameter for Sr_2RuO_4 is about a = b = 0.3873 nm, and the *out-of-plane* parameter c = 1.27323 nm[31]. In addition, experiments have proven that no structural phase transition was observed by cooling the Sr_2RuO_4 crystals down to 100 mK, no structural phase transition was detected[4], and the structure remains tetragonal[51]. Furthermore, the T_c of Sr_2RuO_4 single crystals did not change considerably after high-temperature annealing in oxygen with the pressure ranges from 10^{-2} to 10^2 bar[52]. As will be discussed in this chapter, the T_c of Sr_2RuO_4 is extremely sensitive to disorder. Since little change in T_c after the O_2 annealing process was observed, this suggests there was little change in crystalline quality. This implies that the oxygen content in the Sr_2RuO_4 single crystal must be very close to stoichiometry under the oxygen pressure of 10^{-2} to 10^2 bar during annealing, and the annealing process did not alter the oxygen content in the crystal appreciably[52]. Currently there is no report on how the T_c of Sr_2RuO_4 responses to variations of oxygen content in oxygen nonstoichiometric Sr_2RuO_4. What is known is that Sr_2RuO_4 bears a close structural resemblance to cuprates as previously discussed, and the T_c of cuprates has a high dependency on oxygen content[53]. In $YBa_2Cu_3O_{7-x}$, for instance, oxygen content can alter its crystal structure[54] and the T_c value decreases as oxygen content (x) increased from 0 to 0.65[55].

(a) (b)

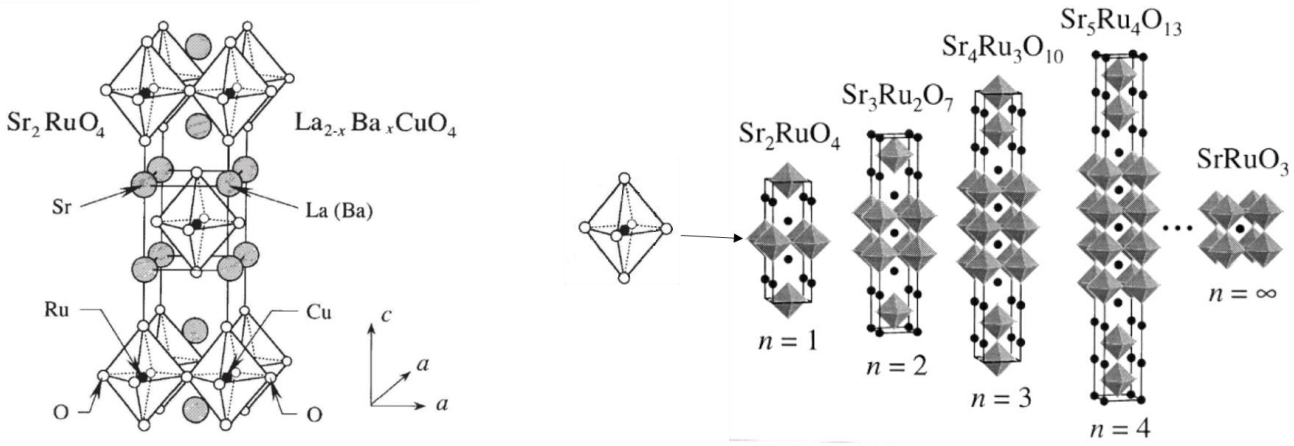

Figure 3.1 (a) The crystal structure of Sr_2RuO_4 and $La_{2-x}Ba_xCuO_4$. Ru and O form an octahedron with Ru in the center and O in the six apical positions[31]. (b) Crystal structures of the $Sr_{n+1}Ru_nO_{3n+1}$ Ruddlesden–Popper homologous series[47].

Moreover, no systematic studies have been carried out to examine the tolerance of Sr_2RuO_4 phase stability to variations in the Sr/Ru ratio. Nonetheless, being one part of the $Sr_{n+1}Ru_nO_{3n+1}$ Ruddlesden-Popper phases, Sr_2RuO_4 (n = 1) has the highest Sr/Ru ratio compared to the rest of the phases in the series, which is Sr/Ru = 2. For the rest of the phases with n > 1, the Sr/Ru ratio decreases from 2 to 1, and Sr/Ru = 1 is from the $SrRuO_3$ (n = ∞) phase. In other words, Sr_2RuO_4 has the highest Sr/Ru ratio while $SrRuO_3$ has the lowest Sr/Ru ratio in the series. This means that both $SrRuO_3$ and Sr_2RuO_4 have the most extreme compositions in terms of Sr/Ru ratio. Consequently, amongst the Ruddlesden-Popper series, $SrRuO_3$ and Sr_2RuO_4 should have the highest tolerance to non-stoichiometric variations in the Sr/Ru ratio.

3.1.2 Transport Properties

In terms of electrical transport properties, there are some differences in the temperature dependence of resistivities in both *in-plane* and *out-of-plane* direction of Sr_2RuO_4. As shown in Figure 3.2, the *in-plane* resistivity (ρ_{ab}) has a metallic behavior which shows resistivity decreasing with decreasing temperature. In contrast, the *out-of-*

plane resistivity (ρ_c) is totally different. Its resistivity first goes up as the temperature decreases from room temperature. The resistivity peaks at about 130 K, and starts decreasing upon further cooling. The difference between the *in-plane* and *out-of-plane* profiles can be associated with the structure of Sr_2RuO_4. In a layered material such as Sr_2RuO_4 which consists of SrO and RuO_2 layers, the RuO_2 is believed to be the major conductive layer while SrO is generally insulating[17]. In c-axis oiented Sr_2RuO_4, both SrO and RuO_2 layers are alternately stacked along the c plane (*out-of-plane*). Therefore, conductivity in the *in-plane* direction is much higher because electrons can travel along the conductive RuO_2 layer, whereas the conductivity in the *out-of-plane* direction is much lower because electrons have to travel between the conductive RuO_2 and insulating SrO layers[4]. Owing to this fact, it is obvious that the resistivity of Sr_2RuO_4 is highly anisotropic, with the ratio between *out-of-plane* and *in-plane* resistivity ρ_c/ρ_{ab} being about 220 at 290 K. This ratio further increases to about 850 at 2 K[31]. This resistivity anisotropy of Sr_2RuO_4 is not unique, but very common among layered superconducting materials. For example, in $YBa_2Cu_3O_{7-x}$, the ratio of ρ_c/ρ_{ab} is about 30 at 300 K[56]; while for $Bi_2Sr_{2.2}Ca_{0.8}Cu_2O_8$, the ratio of ρ_c/ρ_{ab} is in the magnitude of 10^5 at 300 K[57].

In addition, at temperatures below 25 K, a quadratic temperature dependency can be observed for both *in-plane* and *out-of-plane* resistivity. It can be fitted well to the equation: $\rho = \rho_0 + AT^2$, where A is a constant, and ρ_0 is the residual resistivity[58], as shown in the inset in Figure 3.2. This quadratic temperature dependency matches a theoretical model that at low temperatures the electron-electron interaction is the major contributing factor to electrical resistivity[45, 59]. From the inset in Figure 3.2, the constant A in equation $\rho = \rho_0 + AT^2$ can be calculated. They are 4×10^{-9} Ω*cm/K^2 and 5×10^{-6}Ω*cm/K^2 for *in-plane* and *out-of-plane* resistivity, respectively, which also implies a highly anisotropic nature.

Finally, although both the *in-plane* and *out-of-plane* resistivity at temperatures above 100 K display linear dependency on temperature, the slopes for the resistivities of the two directions are considerably different, with one positive and one negative. The

in-plane resistivity has positive slope which represents metallic behavior while the *out-of-plane* resistivity has negative slope which represents insulating behavior, consistent with my previous discussion.

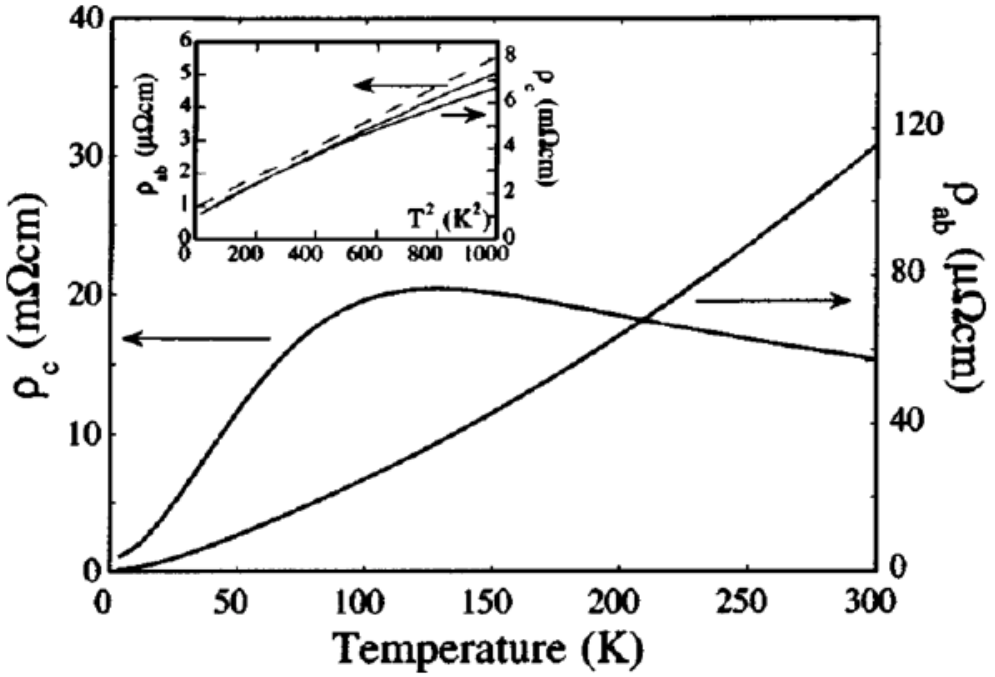

Figure 3.2 The *in-plane* and *out-of-plane* resistivity as a function of temperature for Sr_2RuO_4. The inset shows both the *in-plane* and *out-of-plane* resistivity quadratic dependency on temperature. The dashed line represents the fitting of $\rho = \rho_0 + AT^2$, and the solid lines represent the experimental data[58].

3.2 Superconducting State of Sr_2RuO_4

The discovery of superconductivity in Sr_2RuO_4 made scientists realize that copper is not a prerequisite to achieve superconductivity in layered perovskites. Although Sr_2RuO_4 bears a very close structural resemblance to that of $La_{2-x}Ba_xCuO_4$, the T_c is much lower compared to that of the cuprates. In fact, Sr_2RuO_4 has a totally different superconducting behavior to that of the cuprates. This is explained in the following parts.

When superconductivity in Sr_2RuO_4 was first discovered, as shown in Figure 3.3, the T_c was below 1 K. Now, with more advanced techniques for single crystal fabrication to reduce the concentration of impurities and defects, the experimental T_c is approaching its theoretical value, 1.5 K[15, 16]. This great progress has therefore enabled scientists to carry out many experiments to study the intrinsic superconducting parameters of Sr_2RuO_4. Table 3.1 is a brief summary of the current results on the measurements and estimations of several important Sr_2RuO_4 superconducting parameters.

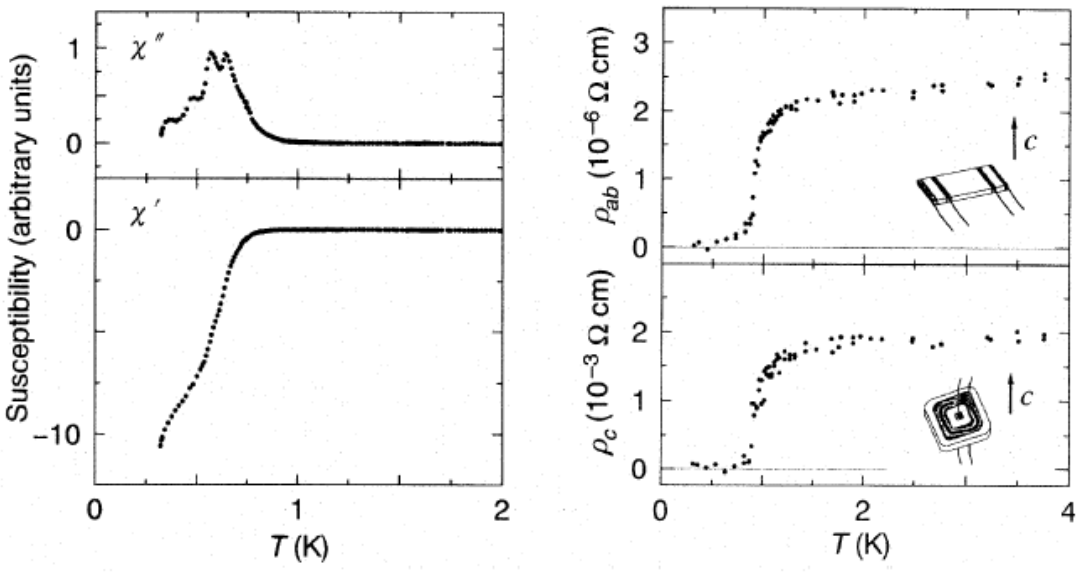

Figure 3.3 Magnetic susceptibility (left) and resistivity measurement (right) of Sr_2RuO_4 single crystals[31].

Superconducting parameters	*In-plane*	*Out-of-plane*
Upper critical field ($\mu_0 H_{c2}$)	1.5 T	0.075 T
Lower critical field ($\mu_0 H_{c1}$)	1 x 10^{-3} T	5 x 10^{-3} T
Coherence length (ξ)	660 Å	33 Å
Penetration depth (λ)	1520 Å	30000 Å

Table 3.1 *In-plane* and *out-of-plane* superconducting parameters of Sr_2RuO_4 at 0 K. High quality Sr_2RuO_4 single crystals (T_c about 1.49 K) were measured. [4, 16, 60-62]. Sr_2RuO_4 is a type II superconductor[4]. In the table, μ_0 is the permeability constant.

3.2.1 Sensitivity to Impurities and Structural Disorders

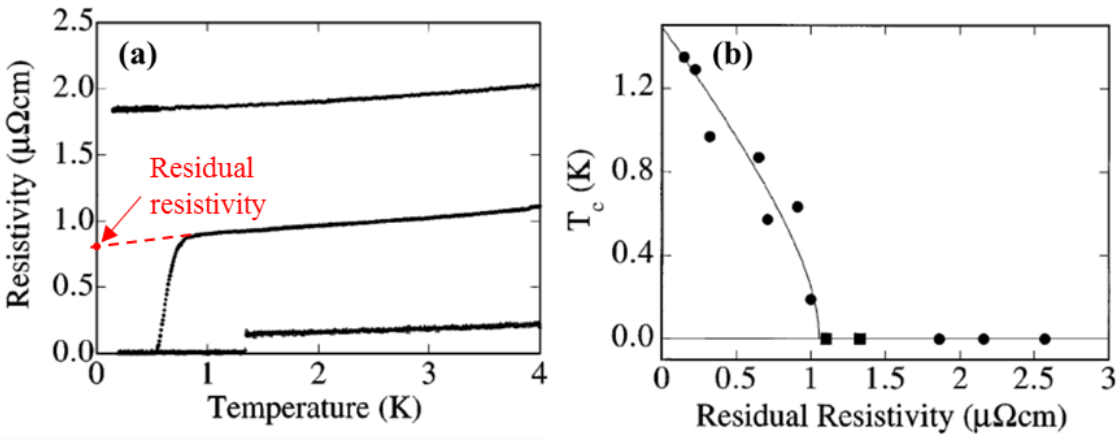

Figure 3.4 (a) Resistivity as a function of temperature of three Sr_2RuO_4 single crystals down to 130 mK: a non-superconducting Sr_2RuO_4, a superconducting Sr_2RuO_4 with T_c lower than 1 K, and a superconducting Sr_2RuO_4 with T_c about 1.5 K[15]; (b) T_c dependency on the residual resistivity of 12 pieces Sr_2RuO_4 single crystals[15].

A group of Sr_2RuO_4 single crystals ranging from non-superconducting to superconducting with T_c > 1 K were selected and their superconductivity dependency on the residual resistivity (ρ_0) was studied[15, 63]. In Figure 3.4(a), three Sr_2RuO_4 single crystals with different T_c were studied. As can be seen, the sample with the highest T_c and sharpest superconducting transition is the one with smallest residual resistivity. The residual resistivity of superconducting Sr_2RuO_4 is defined as the following: from the

superconducting onset transition, as shown in Figure 3.4(a), the resistivity curve can be extrapolated to T = 0 K as shown in the red dashed line. The value marked by the red dot at 0 K is defined as the residual resistivity for the superconductor.

In contrast, the non-superconducting sample has the highest residual resistivity, while another sample with a much lower T_c and a broad transition has a medium level of residual resistivity. Furthermore, a more general rule is shown in Figure 3.4(b), where more data were collected. With the increase in residual resistivity, the T_c is reduced and even being suppressed.

The residual resistivity is directly linked to the impurity amount in the sample, and the mean free path (l) of Sr_2RuO_4 can be estimated using the following equation:

$$l = \frac{2\pi\hbar d}{e^2 \rho_0 \sum_i k_F^i} \quad (3.1)^{[15]},$$

where $\sum_i k_F^i$ is known from the quantum oscillations[64], and d is the *out-of-plane* interlayer spacing of Sr_2RuO_4. Of all the data that has been reported, the mean free path for the cleanest sample[15] is about 700 nm, while for the incipient superconducting sample, the mean free path is about 90 nm, which is close to the value of the Sr_2RuO_4 *in-plane* coherence length of 66 nm[16]. Therefore, it can be concluded that superconductivity in Sr_2RuO_4 is destroyed when the mean free path is close to the coherence length[15, 65].

The elements in the impurities were also studied[15]. It was found that the impurities were non-magnetic. Traces of Ba and Ca were found, but Al and Si were dominant among the impurities, especially in samples with lower T_c. It was found that in superconducting Sr_2RuO_4 single crystal samples, the maximum amount of Al and Si are 50-100 ppm and 100 ppm, respectively. In the purest samples (T_c > 1.3 K), the Al or Si is less than 30 ppm[15].

Besides impurities, structural defects also affect the superconductivity in Sr_2RuO_4. By controlling the growth conditions, mainly the growth rate, the T_c for different batches of Sr_2RuO_4 single crystals vary a lot, while the impurities can still be maintained at low levels[15, 60]. Y. Inoue studied the microstructures of these Sr_2RuO_4 single crystals[66]. They found the existence of locally distributed planar defects, which

were perpendicular to the a-b planes. Especially in a sample with a much lower T_c (about 0.4 K), many such kind of defects were discovered, which were regarded as pair breakers for superconducting Sr_2RuO_4.

3.2.2 A Possible *p*-wave Spin Triplet Superconductor

The question of the superconductivity mechanism in Sr_2RuO_4 has continued ever since its discovery[31]. Early in 1995, Rice and Sigrist[46] made an very intriguing theoretical suggestion that the Sr_2RuO_4 is possibly an unconventional superconductor with a triplet pairing[4]. Soon after that, results from many experiments began showing up to support this speculation. Firstly, as described above, superconductivity in Sr_2RuO_4 is extremely sensitive to defects and impurities to the extent that its T_c can easily be suppressed by nonmagnetic impurities[15], which apparently suggested an unusual pairing. Secondly, the enhanced electron effective mass measured in Sr_2RuO_4 suggests a strong electron-electron interaction[31]. This is reminiscent of the unconventional heavy-fermion superconductors[59]. Apart from the examples listed above, there are many more findings that suggested a triplet pairing state for superconducting Sr_2RuO_4[67, 68]. Promising as these results are, none of them give direct proof of triplet superconductivity.

One of the most definitive measurements to determine the superconducting parity is the nuclear magnetic resonance (NMR) technique[46], which identifies the change in spin susceptibility of the Cooper pairs[69]. The spin susceptibility is the response of electron spin to magnetic field. Is it often used to distinguish between spin singlet and spin triplet pairing. For a spin singlet superconductor, the spin susceptibility of the superconducting Cooper pair reduces with decreasing temperature and finally diminishes to zero at 0 K[1, 69, 70]. Interestingly, in 1998, K. Ishida et al. reported the results of ^{17}O in Sr_2RuO_4 single crystals measured by NMR. The experiment revealed that the spin susceptibility remained constant below T_c. This is different from the result of the spin singlet superconductors, providing a strong indication that Sr_2RuO_4 is a spin triplet superconductor[1]. Another piece of persuasive evidence comes from the muon

spin relaxation (μSR) experiment. μSR is a helpful technique in detecting time reversal symmetry broken in superconductors. For all spin singlet superconductors, the time-reversal symmetry cannot be broken when the superconductor changed from the normal state to the superconducting state; while it can be broken below T_c for some spin triplet parings[5]. It was detected that below the T_c of Sr_2RuO_4, the time reversal symmetry was broken[5, 71], proving its pairing state as spin triplet.

However, the results from other experiments especially those involving the current-voltage characteristics of the interfaces between Sr_2RuO_4 and other superconductors resulted in some disputes. Since no superconducting Sr_2RuO_4 thin films grown so far can be reproduced or used, only single crystal Sr_2RuO_4 were used. Therefore, the experiments were limited. Moreover, good control of the high quality interface is very difficult. Therefore, all the experiments so far do not provide conclusive results.

To name a few, Jin et al[6] were among the earliest groups ever did this kind of study. In 1999, they designed a Pb-Sr_2RuO_4-Pb junction. In this junction, a decrease in the critical current (I_c) of the junction below the T_c of Sr_2RuO_4 was observed. This seemed to suggest an unusual paring for Sr_2RuO_4, as the exclusion between *s*-wave and *p*-wave order parameter suppressed the critical current of the junction just below the T_c of Sr_2RuO_4. However, their Sr_2RuO_4 crystals inevitably have the inclusion of Ru, which obscured the understanding of the results. In her later work in 2000 in a In/Sr_2RuO_4 junction, Jin[2] found the Josephson coupling can only happen in *in-plane* In/Sr_2RuO_4 junctions, not for *out-of-plane* junctions. This selection indicated that the order parameter for Sr_2RuO_4 could be *p*-wave, but equally could also be *d*-wave. Moreover, junctions with single crystals made displayed poor reproducibility and hence this could not be seen as strong proof. There have been many subsequent experiments. Although none of the results contradicted to the spin triplet state of Sr_2RuO_4, none of them is conclusive or can give a solid support due to the above problems. More work in the future is needed to unambiguously find the mechanism for superconductivity in Sr_2RuO_4.

Recalling the work that scientists have done in the past, the symmetry of the order parameter of high T_c superconductors, was only settled after phase-sensitive measurements were carried out[72, 73]. In phase-sensitive experiments, the phase rather than the amplitude of the superconductor order parameter is determined as a function of crystal orientation[74]. This is measured through the Josephson effect[11], which is the phenomenon of supercurrent flowing across a weak link normally coupled by two superconductors[19].

Similarly, this idea can also be used in the work of Sr_2RuO_4[4]. Although Josephson junctions made of Sr_2RuO_4 single crystal can also be used, the aforementioned problems about junction quality would continue to exist and hinder the interpretation of the results. Therefore, high quality superconducting Sr_2RuO_4 in a thin film form is preferred, which can facilitate the in-situ device fabrications. A possible phase-sensitive device for Sr_2RuO_4 is shown in Figure 3.5.

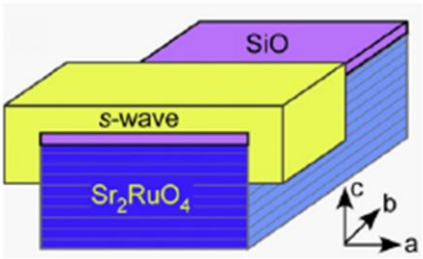

Figure 3.5 A schematic drawing of the phase-sensitive device for determining the pairing symmetry of Sr_2RuO_4. A magnetic field is applied along the junction plane[74].

The Josephson current through two Josephson junctions on the opposite faces of a spin triplet superconductor would be out-of-phase with one another by 180°, which means the intrinsic phase difference of the superconducting order parameter change by 180° after rotation[74]. In fact, in a device where the *s*-wave superconductor in Figure 3.5 was $Au_{0.5}In_{0.5}$ and Sr_2RuO_4 single crystal was used[11], a change of 180° in the superconducting order parameter was observed under rotation. This clearly demonstrates a *p*-wave pairing in Sr_2RuO_4. Nevertheless, reproducibility and quality of the junction is still the problem. Therefore, superconducting Sr_2RuO_4 thin films which

can be used in device fabrications are highly sought after.

3.3 Fabrication of Sr_2RuO_4

No reliable study on Sr_2RuO_4 can be carried out without the growth of high quality Sr_2RuO_4 samples. Sr_2RuO_4 single crystals and epitaxial Sr_2RuO_4 thin films are both being investigated. The related techniques are briefly discussed in the following parts.

3.3.1 Single Crystal Sr_2RuO_4

The most commonly used method to grow Sr_2RuO_4 single crystals is the floating zone method. The conventional setup is shown in Figure 3.6. In this process, a melting feeding rod is suspended on top of a seed material. The seed material can be either polycrystalline or single crystal Sr_2RuO_4. By moving both the feeding rod and the seed material simultaneously, the single crystal grows continuously on the seed material[7, 45].

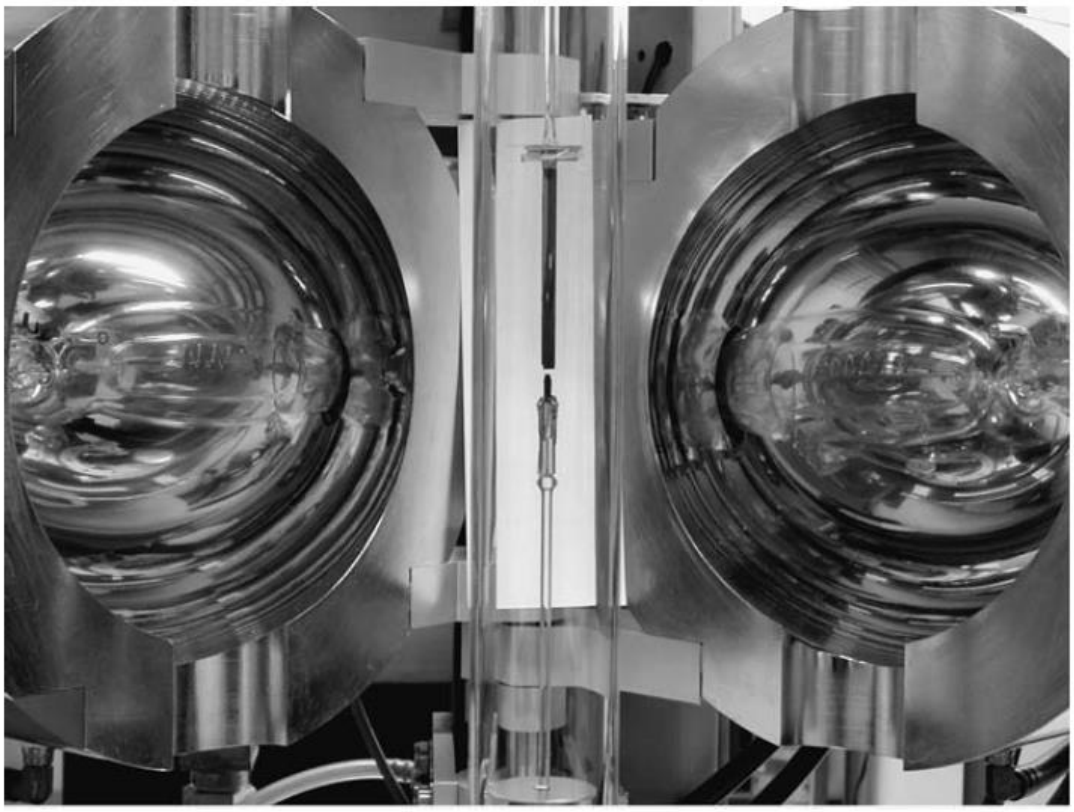

Figure 3.6 Photograph of the floating zone melting furnace[45].

In this process, the quality of the Sr_2RuO_4 single crystals depends on a few growth

conditions[7]. First is the growth rate, or the moving rate of the two rods. A higher growth rate results in serious defects in the sample, whereas a lower growth rate can easily lead to Ru deficiency, both of which yield a much lower T_c[7]. Second is the ratio of the starting powders. Due to the fact that RuO_2 can easily turn to the volatile gaseous RuO_4, the growth process gets complicated. The loss of RuO_2 results in phase segregation and volume shrinkage of the molten materials[13]. Therefore, an excess of RuO_2 powders is always added in the initial powders in order to compensate for the loss. It is crucial how much excess RuO_2 is added. An excess of 20% Ru in the feeding rods would result in the inclusion of other unwanted phases[7]. Nevertheless, with the addition of excess RuO_2, the surface of the as-grown crystal still had a rough polycrystalline appearance, while the core region has Ru inclusions. Hence, crystals for experimental use are chosen from the region between the core and the surface of the single crystal rod[13]. In other words, large samples are very difficult to prepare. The normal size for a crystal is 80 mm x 4 mm x 3 mm[7]. The photograph of a typical Sr_2RuO_4 single crystal is shown in Figure 3.7.

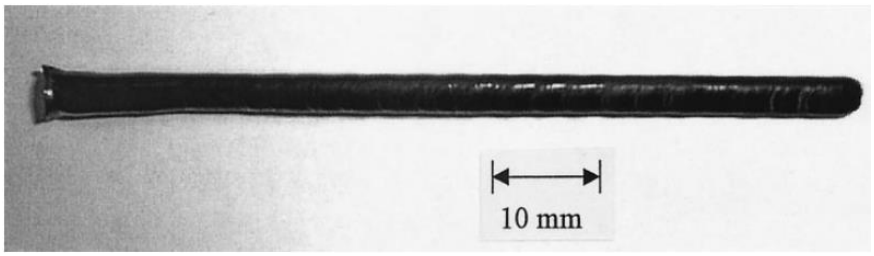

Figure 3.7 Photograph of a Sr_2RuO_4 single crystal grown by floating-zone method[7].

3.3.2 Thin Film Sr_2RuO_4

Growth of epitaxial thin film Sr_2RuO_4 on lattice-matched substrates is another alternative to achieve high quality samples. To date, techniques including both molecular-beam epitaxy (MBE)[75] and pulsed laser deposition (PLD) have been employed[14, 17, 18, 47, 76-81] to grow Sr_2RuO_4 thin films. However, results are far from satisfactory. For MBE growth, there was only one report on the growth of Sr_2RuO_4 thin films found in the literature[75] where monolayer doses of Sr and Ru were deposited

alternatively. However, no transport properties on the films were reported. Therefore, the advantages of using MBE to grow Sr_2RuO_4 thin films remains an open question. It is apparent that MBE is a less popular method to grow Sr_2RuO_4 thin films compared to PLD. One of the possible disadvantages of using MBE might be that: in order to achieve high quality films on a specific substrate, the atomic layer which is energetically preferred for the nucleation of Sr_2RuO_4 has to be determined. Since this work has yet to be done, the usage of MBE is limited.

Most growth of Sr_2RuO_4 thin films were carried out by PLD. Currently, epitaxial Sr_2RuO_4 thin films can be achieved, but most of the thin films have a metal-insulating transition at low temperatures. Reports of fully metallic Sr_2RuO_4 thin films growth are rare[77]. Prior to this work[76], there has only been one report[14], in 2010, on superconductivity in Sr_2RuO_4 thin films in the literature. To make things clear, the pulsed laser deposition parameters and results of the Sr_2RuO_4 thin films from all the publications have been summarized in Table 3.2. The deposition parameters vary a lot among different research groups, which indicates a very equipment-dependent growth condition of Sr_2RuO_4 for optimization.

The reason for the difficulty in growing fully metallic or even superconducting Sr_2RuO_4 thin films is still not clear yet. Given the fact that in single crystal Sr_2RuO_4, superconductivity can be easily destroyed by defects, it is reasonable to associate the non-superconducting Sr_2RuO_4 thin films with high levels of defects. Zurbuchen[17] studied the microscopic structure of Sr_2RuO_4 thin films and found many planar defects. These defects lie along the {011} Sr_2RuO_4 planes as shown in Figure 3.8(a)[78] and are called *out-of-phase* boundaries (OPBs). OPBs are common defects in complex oxides[82], caused by a fractional misalignment in the c-axis direction between two neighboring regions in the crystal[78]. In the Sr_2RuO_4 thin films as shown in Figure 3.8(a), the c-axis mis-registry across the OPB is 0.25 nm[78]. The defects either penetrate the whole film thickness, or are annihilated where pairs of opposite inclination meet, as shown in the schematic drawing in Figure 3.8(b). As a result, the continuity of the RuO_2 layer which is believed to be responsible for the conductivity is disrupted. Furthermore,

the distance between those defects are in the same order as the *in-plane* superconducting coherence length of Sr_2RuO_4. This may explain why reports on superconducting Sr_2RuO_4 thin films are almost non-existent.

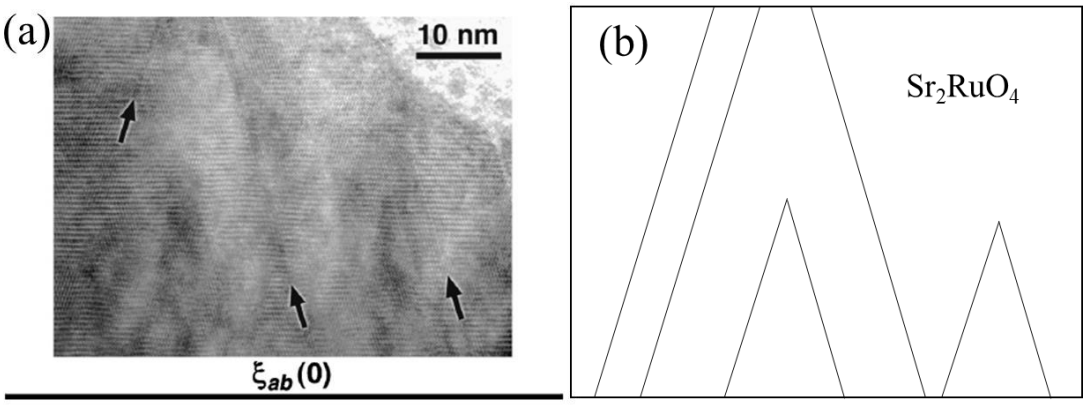

Figure 3.8 (a) TEM image of a Sr_2RuO_4 thin film with the common planar defects, some of which are represented by the arrows. The magnitude of the scale bar is equal to $\xi_{ab}(0)$ = 66 nm[17, 78]. (b) Schematic drawing of the OPBs in Sr_2RuO_4 films; diagonal lines represent OPBs. Two OPBs with opposing inclination have annihilated each other where they meet, while two OPBs with parallel inclination penetrate through the full thickness of the film[78].

Little is known about the nucleation mechanism of OPBs. A possible mechanism associated with the nucleation process was proposed and shown in Figure 3.9. Taking the growth of Sr_2RuO_4 films as an example, two SrO and one RuO_2 layers constitute the unit cell of Sr_2RuO_4. Therefore, many possible nucleation sequences of the layers can happen on the substrate. For example, on the $LaAlO_3$ substrate shown below, the growth of the Sr_2RuO_4 thin films can either choose SrO-RuO_2-SrO or RuO_2-SrO-SrO ordering[78]. If the two growth sequences both take place on the substrate, when two adjacent parts with different growth sequence meet, they will form an OPB.

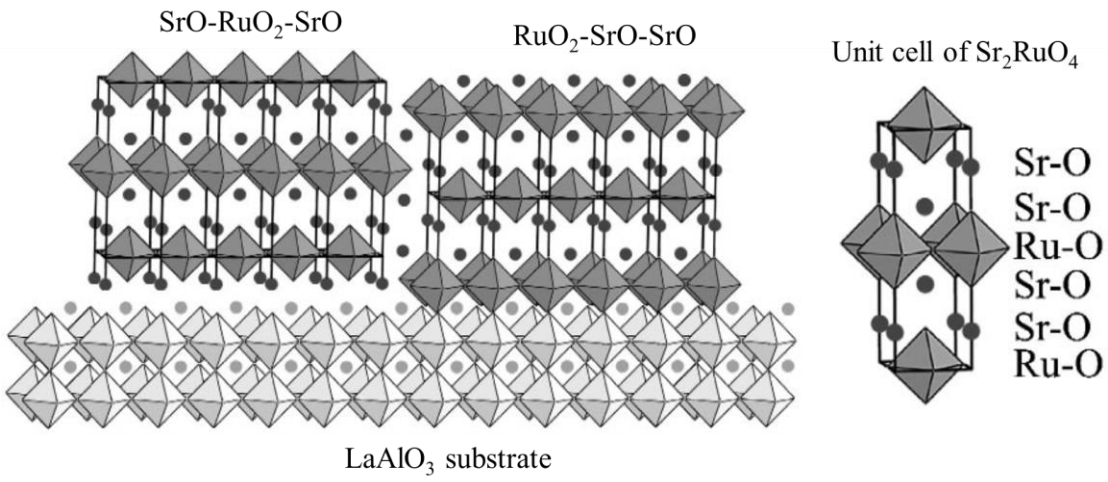

Figure 3.9 Possible OPB nucleation mechanism. The coordination octahedral of the ruthenium are shown, with circles representing Sr[78].

Reference	Temperature (℃)	Fluence (J/cm^2)	P_{o2} (mTorr)	Distance (cm)	Comments
S. Madhavan et al[18].	950 – 1050	3 – 4	1 – 2	7.5	metal-insulating between 70 – 160 K
D. G. Schlom et al[47, 77].	1000	2 – 3	0.003	not reported	$\rho_{300\ K}/\rho_{\ 4\ K}$ is 10 for the fully metallic film, while the others had metal-insulating transitions below 30 K.
M. A. Zurbuchen et al[17, 78].	1000	2.7	0.0008 – 0.005	7.5	Only one metallic film (the residual resistivity ρ_{ab} = 32 μΩ·cm), the others had metal-insulating transition below 50 K.
D. Reisinger et al[79].	950	1.2	20	not reported	not reported
Y. Krockenberger et al[14].	920	3	0.4	5	**Superconducting**, T_c from 0.9 K (onset) to 0.6 K (zero resistivity), $\rho_{300\ K}/\rho_{2\ K}$ is 82.
T. Ohnishi et al[80].	1100	0.43	7.5	not reported	not reported
Y. Takahashi et al[81].	1000	2.8	1.3	not reported	Metallic films, ρ_{ab} = 2.7 μΩ·cm (2 K).
J.Cao et al[76]. (my earlier work)	950	1.5	7.5	7.5	**Superconducting**, T_c onset is 1.9 K.

Table 3.2 All the reported growth parameters on *c*-axis epitaxial Sr_2RuO_4 thin film growth by pulsed laser deposition in the literature.

3.4 Sr_2RuO_4-Ru Eutectic System

While scientists have been keen on studying the nature of superconductivity in Sr_2RuO_4, another related system was discovered in 1998[8]. This is the eutectic Sr_2RuO_4-Ru system, which has a much higher T_c at 3 K. Sr_2RuO_4-Ru system is commonly seen in the core region of the Sr_2RuO_4 single crystal where the Ru content is more than 20%, or when the growth speed is fast[8]. Figure 3.10 is an optical microscopic photo of the Sr_2RuO_4-Ru eutectic system. Ru was distributed in the Sr_2RuO_4 matrix in the form of a lamellar pattern. This lamellar pattern is a typical eutectic solidification result[83]. The width of the Ru lamellar is about 1 μm, with the length and depth both in the range of 1 to 10 μm. The separation between two Ru lamellae is of the order of 10 μm[8]. The lattice parameters of Sr_2RuO_4 are the same for regions with or without Ru inclusions[8].

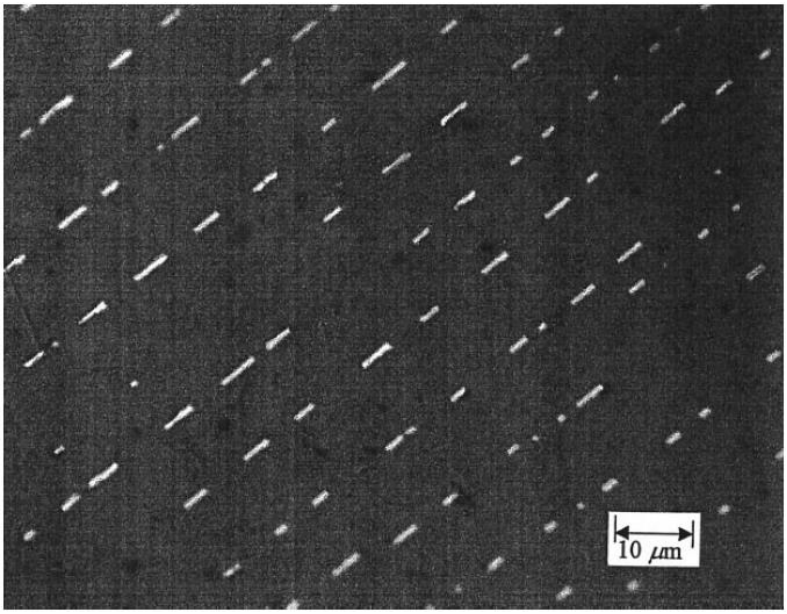

Figure. 3.10 Optical microscopy of (1 0 0) surface of the Sr_2RuO_4-Ru crystal. The bright areas are Ru metals and the black matrix is Sr_2RuO_4[7].

Separately, Sr_2RuO_4 is superconducting at 1.5 K while Ru is superconducting at 0.5 K. Interestingly, this Sr_2RuO_4-Ru eutectic system has a higher onset T_c at about 3

K. As shown in Figure 3.11(a) and Figure 3.11(b), Sr_2RuO_4-Ru eutectic system has very broad diamagnetic transition starting at 2.5 K compared to the very sharp transition at 1.45 K for pure Sr_2RuO_4. Similarly, the resistivity also undergoes a broad transition for Sr_2RuO_4-Ru eutectic system as shown in Figure 3.11(c). Nevertheless, the resistivity of the two systems remain indistinguishable at room temperature.

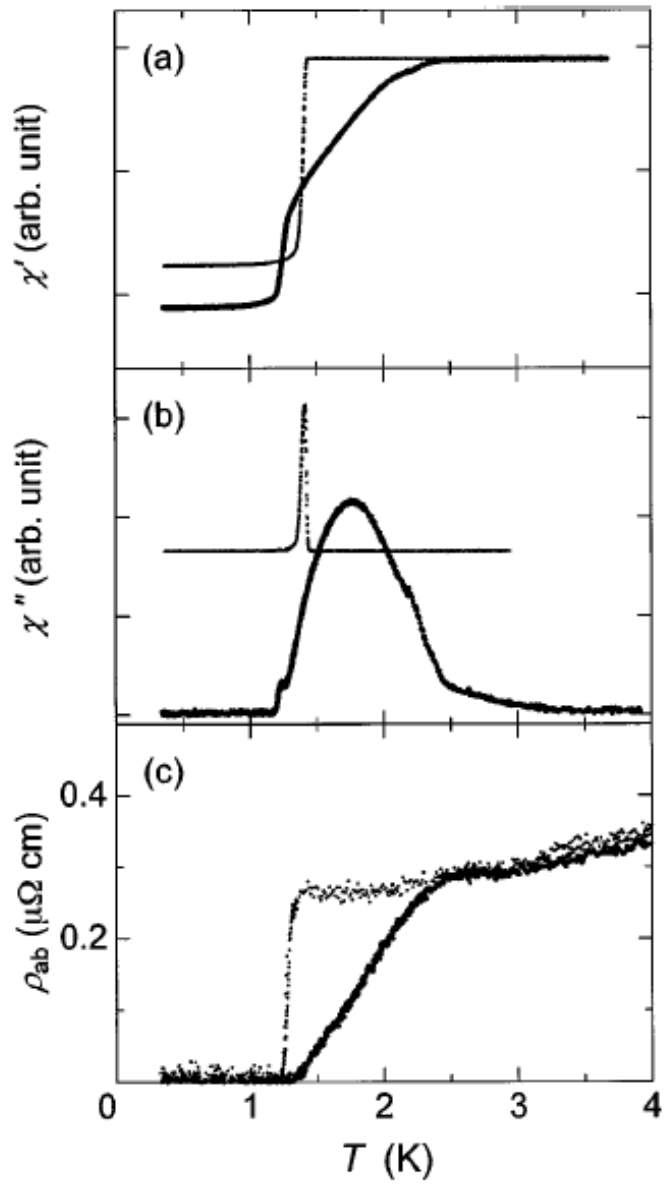

Figure 3.11 (a) *In-phase* and (b) *Out-of-phase* components of the *a.c* susceptibility, and (c) The *in-plane* resistivity as a function of temperature for both pure Sr_2RuO_4 (small, blurry symbols) and the Sr_2RuO_4-Ru eutectic system (big, dense symbols)[8].

The reason behind this enhanced superconductivity is still not clear at the moment.

It was found that the 3 K superconductivity happens near the interface close to the Sr_2RuO_4 part, not in the Ru inclusions. This suggests the enhanced superconductivity probably originates in the interface where a major modification of the electronic structure can happen[8, 84].

3.5 The Effect of Pressure on The T_c of Sr_2RuO_4 Single Crystals

Uniaxial pressure can be a powerful way to control superconductivity as well as the electronic structure[85-87]. The electronic states of Sr_2RuO_4 has been both experimentally and theoretically revealed to change drastically with an anisotropic distortion[10, 88]. Recalling the 3-K phase mentioned in the previous section, the T_c of which is 3 K. One possible reason for the enhancement is that the presence of Ru induces anisotropic distortions in Sr_2RuO_4 and further enhances the T_c significantly[84, 89].

Subsequently the uniaxial pressure effect on the T_c of Sr_2RuO_4 single crystals has been systematically studied. The findings are briefly discussed here. Two Sr_2RuO_4 single crystal samples were used for the experiments: one with a zero-strain T_c of 1.35 K, and the other 1.45 K. Strain has been applied on two different orientations: [1 0 0] and [1 1 0]. The results were shown in Figure 3.12(a) and (b), separately[90].

T_c enhancement was found for the two samples under either [1 0 0] or [1 1 0] strain, with different responses, though. It is obvious that in Figure 3.12(a), the response to [1 0 0] strain is symmetric, i.e. the enhancement of T_c under tensile and compressive [1 0 0] strain is almost of the same magnitude. In comparison, the response to [1 1 0] strain is weaker and mainly linear[90]. Tensile [1 1 0] strain enhances the T_c value more than compressive [1 1 0] strain. The reason for the different T_c enhancement response to [1 0 0] and [1 1 0] strain might be rooted in the nature of the symmetry of the superconductivity in Sr_2RuO_4[90], which is yet to be answered.

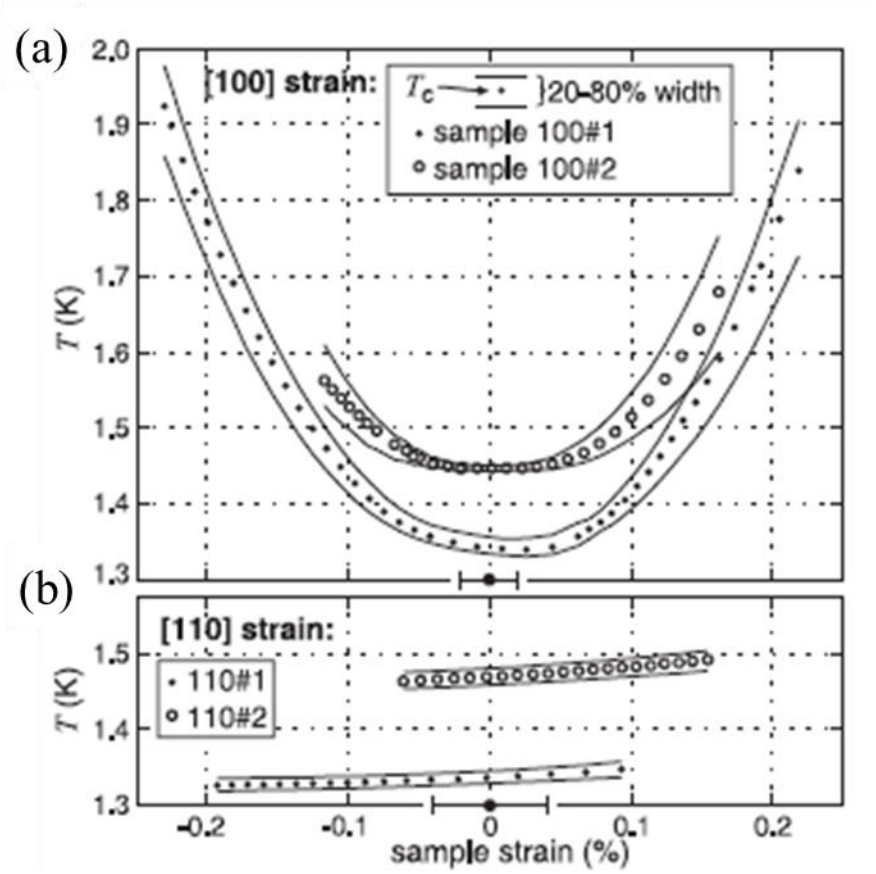

Figure 3.12 (a) T_c dependency on the [1 0 0] oriented strain. ε > 0 indicates tension. T_c was measured using *a.c.* susceptibility and was taken at the 50% point of χ'. The black lines are the 20 and 80% points, giving a measure of the transition width. The error bar on the horizontal axis indicates the error in locating zero strain. (b) T_c dependency on [1 1 0] strain for two further samples cut from the same crystals as in (a)[90].

Chapter 4 Thin Film Growth

As its name suggests, a thin film is normally a very thin layer of material with thickness typically ranging from a few nanometers to micrometers coated on a substrate. During thin film growth, a good control of film microstructure, surface and interface as well as thickness no doubt plays a vital role in today's electronic devices and basic scientific studies. This chapter introduces the basic principles about film growth and thin film deposition techniques. Section 4.1 introduces the three growth modes of thin films. Section 4.2 explains related information about epitaxial film growth. Section 4.3 is a systematic study of pulsed laser deposition.

4.1 Thin Film Growth Mode

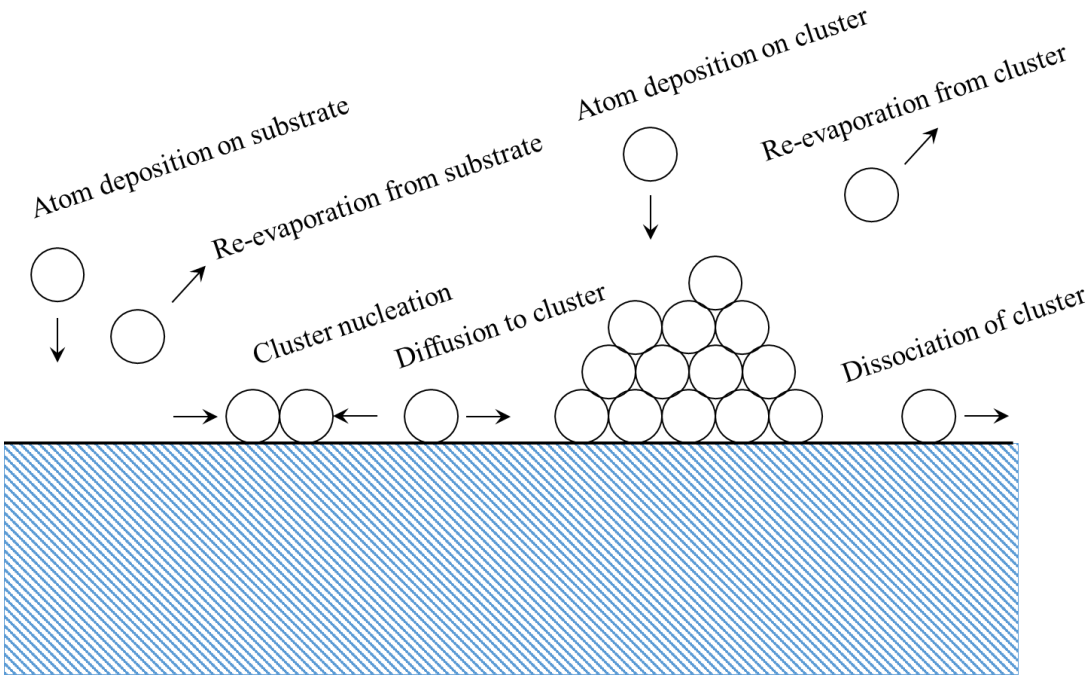

Figure 4.1 Atomic process during thin film growth[91].

During thin film growth, the substrate is exposed to the impinging vapor of species and is covered with highly mobile atoms. As illustrated in Figure 4.1, the adatoms can be adsorbed and diffuse on the surface, encounter other adatoms or clusters to form either mobile or stationary clusters, get detached from a cluster and remain on the

substrate surface or get re-evaporated[91]. As more clusters nucleate, they would grow and coalescence into either 2D or 3D nuclei. Subsequently the thin film continue to grow to the full thickness.

Thin film growth is conventionally categorized into three modes: Frank van der Merwe (layer by layer or 2D) growth, Volmer-Weber (island growth or 3D) growth, and Stranski-Krastanov (mixed growth) growth. The three growth modes are schematically shown in Figure 4.2[91, 92]. The following is a brief discussion of the three modes from the thermodynamic and kinetic point of view.

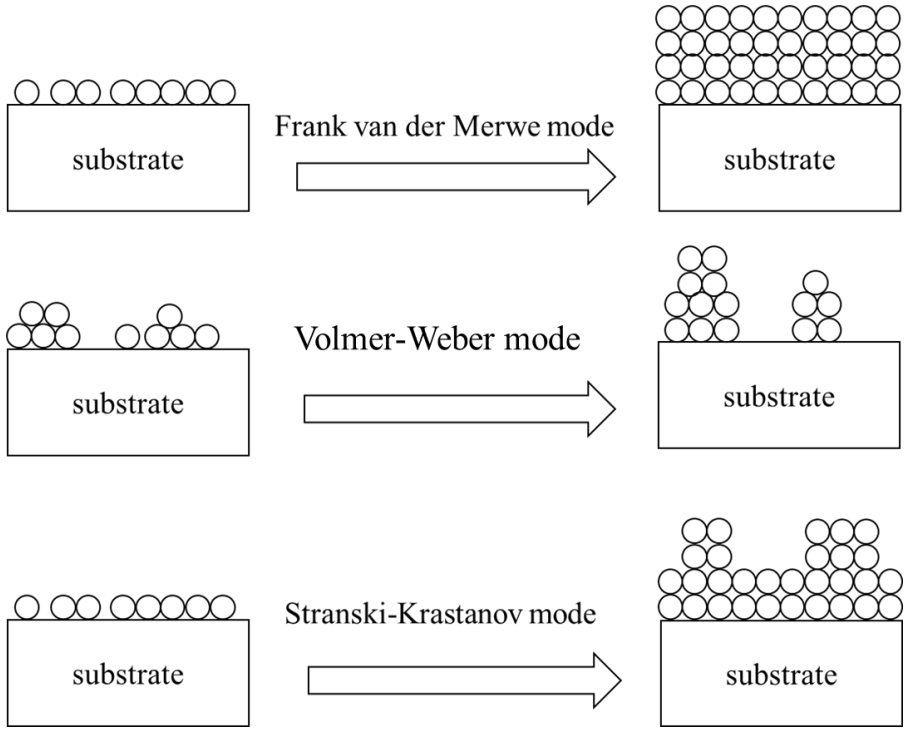

Figure 4.2 Schematics of three thin film growth modes[92].

Thermodynamic Factors

In Frank van der Merwe mode, atoms are more strongly bound to the substrate than to each other, and they are deposited onto substrate in a layer by layer mode. Therefore, epitaxial thin films (which will be discussed in section 4.2) grown in this mode usually have very smooth surface. The total surface energy has to satisfy the following equation:

$$\gamma_I + \gamma_F \leq \gamma_S \quad (4.1),$$

where γ_I, γ_F ,and γ_S are the surface energies of the interface, film and substrate, respectively[92].

In Volmer-Weber growth mode, atoms are more strongly bound to each other than to the substrate, and atoms form island or clusters. Therefore, the surface of the epitaxial thin film normally is rough. In this mode, the following equation needs to be satisfied:

$$\gamma_I + \gamma_F > \gamma_S \quad (4.2).$$

Stranski-Krastanov growth mode often happens for films having very large lattice mismatch with substrate. The first several atomic layers are deposited as monolayers but the subsequent atoms tend to form islands after that. The change from monolayer to island growth usually happens when strain increases after the formation of the first few monolayers due to lattice mismatch. Therefore, this growth mode is a result from lattice mismatch and accumulation of strain energy as the thickness increases. This will be discussed in more details in Section 4.2 about the mechanism of strain relaxation.

In fact, thin film growth depends not only on thermodynamic factors. Rather, it is affected by both thermodynamic and kinetic factors[92], which is briefly introduced in the following part.

Kinetic Factors

As illustrated in Figure 4.1, film growth kinetics includes the adsorption (deposition on substrate or island cluster), diffusion, desorption (re-evaporation from substrate or island cluster), as well as dissociation of the island cluster itself due to secondary bombardment. These kinetic factors can be characterized by different activation energies. For example, the diffusion process is closely associated with the diffusion activation energy via the diffusion coefficient (D). This can be understood using the following equation:

$$D \propto exp(-E_{act}/kT) \quad (4.3),$$

where k is the Boltzmann's constant, T is the substrate temperature, and E_{act} is the activation energy for diffusion, which is a function of the species (e.g. mass, size). It is obvious that adatoms with low activation energy have high diffusion coefficient, which

are more likely to diffuse and coalesce into an existing island rather than nucleating another new island. This results in a lower overall island density. Therefore, the island density is related to the adatom diffusion process. The higher the diffusion coefficient, the lower the island density[93].

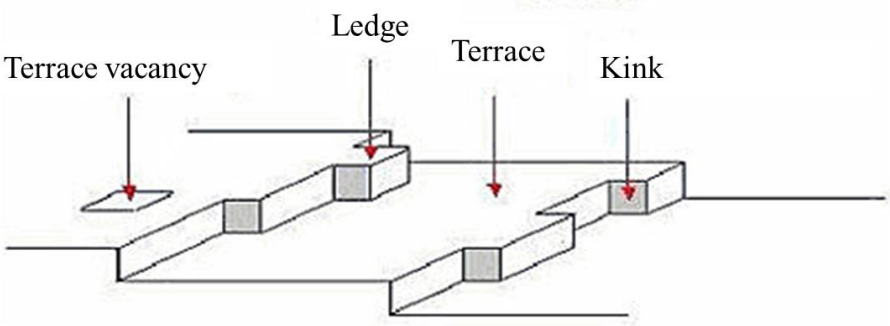

Figure 4.3 A schematic drawing of the Terrace-Ledge-Kink (TLK) model[92].

Film growth usually takes place at active sites, such as crystal defects, atomic steps or impurities by surface diffusion or direct vapor impingement[91], as shown in Figure 4.3. Two very important kinetic aspects affect the growth process - they are the deposition rate and substrate temperature. At low deposition rates, the majority of arriving species have enough time to diffuse along the terrace to the step edges (ledges and kink) and get attached there, resulting in the steady advances of the film layers along the terrace. In addition, some terrace vacancy defects can also be filled, creating a highly dense and high quality film. Similarly, high substrate temperatures result in high diffusion coefficient, as can be understood from equation (4.3). This means the adatoms are more mobile and the diffusion length increases at high temperatures, which reduces the island density and fosters the layer by layer growth. Thus, sufficiently low deposition rate and sufficiently high temperature are kinetically necessary for Frank van der Merwe growth to take place, and epitaxial films are more likely to happen under this condition. On the other hand, excessive deposition rate or low substrate temperature results in Volmer-Weber mode, which increases defects and decreases film epitaxial quality.

4.2 Epitaxial Films

Epitaxy can be defined as the transfer of crystallographic order of the substrate to that of the film via a certain degree of lattice matching. When thin films are deposited on single crystal substrates, the surface energy is minimized by maximizing the density of bonds (of appropriate length and angle) to merge the symmetries of the substrate and film. Therefore, it is energetically more favorable for the film to align itself crystallographically with the substrate in order to match the substrates' bonding symmetry and periodicity, which, to put it another way, is to grow epitaxially.

There are two basic forms of epitaxy, and the simplest one is homoepitaxy. In this scenario, both the composition and the structure of the thin film and the substrate are identical. In this case, the interface surface energy (γ_I) would be zero, and $\gamma_F = \gamma_S$, which satisfy equation (4.1). If the growth condition is optimum, Frank van der Merwe mode always applies regardless of the film thickness. The second form of epitaxy is heteroepitaxy, which is the growth of a material on a substrate with different composition. The film's preferred orientation is decided by the one that can minimize the energy of the system[91]. As the unit cell parameters between the film material and the substrate are usually different, there is a lattice mismatch:

$$f = \frac{a_s - a_f}{a_f} \quad (4.4),$$

where a_f is the lattice parameter of the film, and a_s is that of the substrate. A positive value of f means that the earlier several layers of the epitaxial film is in tension, and a negative value of f indicates that the film is under compression. Epitaxial growth usually happens when the lattice parameters and symmetry between the film and substrate are closely matched. In this case, this growth mode is favored strongly for low misfits (i.e. low γ_I), in the presence of strong bonding between the film and the substrate, which implies low interfacial energy, low film surface energy and high substrate surface energy.

There are three epitaxial regimes depending on the extent of lattice mismatch.

Firstly, if there is little or zero lattice mismatch as in the case of homoepitaxy, there is no lattice strain and the film and substrate are perfectly matched. This is shown in Figure 4.4(a). Therefore, small lattice mismatch is highly desired.

Secondly, if the lattice parameters differs considerably between substrate and film, there is a biaxial strain (ε) due to lattice mismatch (f), thus it gives rise to an elastic energy (E_e). This grows as the film thickness (d) increases, as shown in equation (4.5)[92]:

$$E_e = Yd\varepsilon^2/(1-\vartheta) \quad (4.5),$$

where Y is the Young's modulus (assuming film and substrate have the same Y), υ is the Poisson's ratio. If the film is very thin, it can be elastically strained to the substrate so that the thin layer and substrate have the same interatomic spacing. This is called a coherent film and is illustrated in Figure 4.4(b).

Last but not least, once the film thickness exceeds the critical film thickness (d_c), the total elastic strain energy would be more than the energy associated with a relaxed film which has some dislocations. Therefore, dislocations start to form to relieve the elastic strain, as shown in equation (4.6)[92].

$$\varepsilon = f - b/S \quad (4.6),$$

where S is proportional to the number of misfit dislocations, and b is the Burger's vector. The Burger's vector of a dislocation quantifies the difference between the distorted lattice around the dislocation and the perfect lattice. These dislocations are located at or near the film-substrate interface as shown in Figure 4.4(c). As a result, the film becomes relaxed.

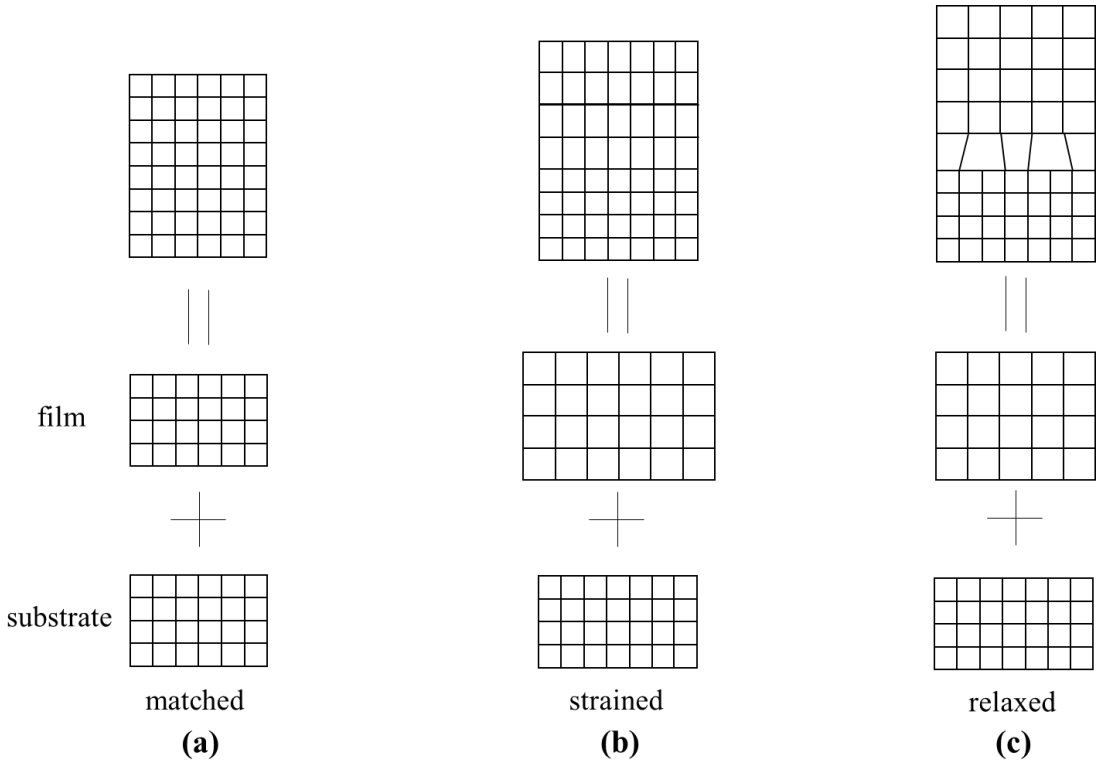

Figure 4.4 The schematic illustration of film and substrate matching: (a) lattice-matched, which is also the case in homoepitaxy, (b) film is strained, and (c) film is relaxed[92].

4.3 Pulsed Laser Deposition

Thin film growth techniques can be broadly categorized into two areas, namely chemical vapor deposition (CVD) and physical vapor deposition (PVD). As the name suggests, CVD usually involves the chemical reactions among different gaseous precursors near or on the hot object surface[94]. On the other hand, PVD is usually the process that involves the material transfer from its solid state to gaseous state and then back to its solid state.

Within the category of PVD, there are also many different techniques, such as pulsed laser deposition (PLD), sputtering, molecular beam epitaxy (MBE), electron beam evaporation. While each technique has its own distinct advantages, there are several key factors which can generally be used to determine which deposition technique to choose: (1) the depositing material, (2) requirements on film crystallinity and stoichiometry; and (3) deposition rates[95]. Generally speaking, sputtering is more suitable for the growth of metals and nitrides. In terms of scalability, sputtering can be used to uniformly grow very large area with high growth rate. PLD is widely applied to grow oxide films with relatively high growth rate compared to MBE, which has a slow deposition rate[96].

With careful control and under optimized conditions, PLD is very versatile to prepare many other kinds of thin films, including complex oxides, polymers[96] like the Teflon films[97], biomaterials like the calcium phosphate bioceramic coatings[98], superlattices like the $BaTiO_3/SrTiO_3$ system[99], superconducting electronic devices[95]. It is popular mainly due to (1) simple set-up in terms of pumping and gas-flow systems; (2) stoichiometric deposition of films with multi-components under optimized conditions; (3) fine control of thin film deposition in terms of film surface and crystallinity; (4) ease of integration with other equipment like reflection high-energy electron diffraction (RHEED) and x-ray photoelectron spectroscopy (XPS), etc[96].

Thin film deposition using PLD happens in a vacuum chamber with or without background gas. It involves a high power pulsed laser as an energy source, which gets

focused by a set of optics and enters the deposition chamber. During deposition, a rotating target is radiated by the laser and the material components get vaporized in the form of a high energy directional plasma plume. Upon arrival at the substrate, which is usually a single crystal, the forward-directed plume gets condensed and therefore a thin film grows. Figure 4.5 is an illustration of a PLD chamber. The quality in terms of crystallinity, uniformity, and stoichiometry and the growth rate of the thin film depends on a lot of deposition parameters. There are several parameters which can be independently controlled in PLD, as discussed in the following sections.

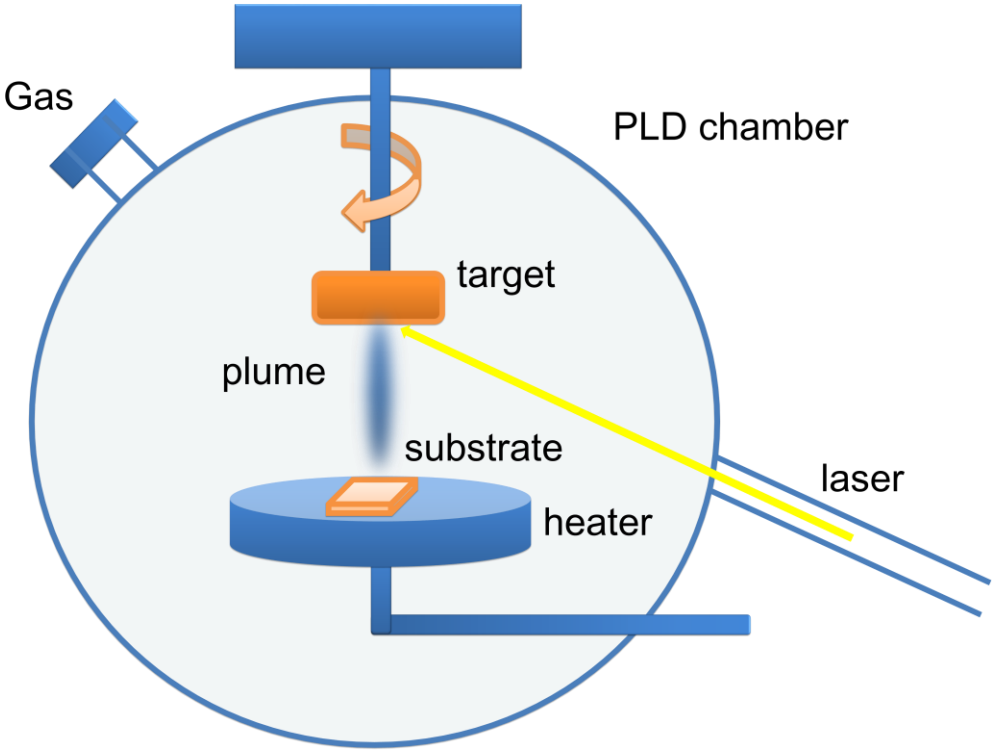

Figure 4.5 A schematic drawing of the PLD chamber.

Laser

A laser is the power source during pulsed laser deposition. The most useful range of laser wavelengths for PLD falls between 200 nm and 400 nm. This is due to the fact that most materials used for deposition have strong absorption at that range. As the laser wavelength gets shorter in that range, the penetration depths into the target materials

are correspondingly reduced. Therefore it is more favorable to use short laser wavelength to ablate thin layers of the target materials [96]. In this research, a KrF laser with the wavelength of 248 nm was used.

Gas Pressure

Many thin film depositions require a reactive gas atmosphere, for example, oxide thin film depositions usually require an oxidizing environment (normally oxygen) to form and stabilize the desired phase. For species with high vapor pressures, a high oxygen pressure is needed to maintain the stoichiometry of the film. For example, in the deposition of $ZnGa_2O_4$ thin films, Zn has a higher vapor pressure compared to that of Ga. Therefore, a significant Zn deficiency was observed in the film deposited at low oxygen pressures. By increasing the oxygen pressure, the Zn loss was compensated[100]. Similarly, for $BiFeO_3$, excessive substrate temperature was known to result in Bi-deficient film and formation of secondary phases. This is due to the highly volatile nature of Bi[101].

Apart from being a reactant, the background gas attenuates and thermalizes the plume during deposition. Therefore, the amount of gas or gas pressures have a great influence on the plume. For example, as the background pressure gets higher, the collisions among all species gets intensified, and the plume propagation velocity gradually decreases. In this regard, the plume spatial distribution, deposition rate and the kinetic energy distribution of the depositing species can be altered by altering background pressure[95, 96]. This in turn affects the manner at which the deposition species arrives at the substrate, resulting in different film qualities[102] Specifically, at extremely low oxygen pressures, the plume essentially expands rapidly to a wide angle of directions upon ejection from target, and thus the amount of plume species reaching the substrate may be reduced. On one hand this can result in low deposition rate and thinner films. On the other hand, this would cause off-stoichiometry in the density of various species on the substrate surface, leading to defects in the film[96]. At intermediate pressure, laser plumes are normally more directed along the target to

substrate direction. Consequently, the arriving atomic species carries some amount of kinetic energy which can result in enhanced diffusivity of the adatoms on the surface and therefore form a layer by layer growth. However, at very high pressures, the velocities of various species in the plume are reduced due to collisions and scatterings. Thus, the deposition rate would be very low and even the surface activation of the species may not be possible. Therefore, an optimal gas pressure is necessary to achieve the uniform velocity distribution of various species, leading to a reduction in the defect density in the film[103].

Target to Substrate Distance

In PLD, the plume has a spatial distribution and the atomic species are non-uniformly distributed within the ablation plume due to its highly forward-directed nature. Therefore, the energy and stoichiometry of the arriving species vary across the distance from the target to substrate. Near the target, the velocities of the different species in the plume are very high, gradually slowing down as the plume travels from target towards substrate due to collisions and scatterings with the background gas. Therefore, if the substrate is too close to the target, the film can be damaged by the bombardment of these energetic species, which is also called re-sputtering[104]. On the other hand, at a relatively long target to substrate distance, the particle flux of the ablated species in the plume over the substrate area decreases. This lowers the deposition rate and hence the film thickness[105]. In addition, if the distance is too far, the surface activation may not be available by moderately energetic ions and atoms, or it may be even worse that some species in the plume may be scattered off before reaching the substrate[106]. Apart from that, over a long target to substrate distance, there could be preferential scattering of lighter atoms or atomic species which can result in off-stoichiometry in the film. For example, in the growth of $SrTiO_3$ thin films, the atomic mass of Ti is lighter than that of Sr. It has been demonstrated that a long target to substrate distance can result in Sr-rich composition, whereas a short distance results in Ti-rich composition[107]. Therefore, the film composition is greatly affected by target-

substrate distance and an optimal distance is required for deposition of the right phase to occur.

Aside from target to substrate distance alone, other deposition parameters can have the same effect as target to substrate distance, therefore creating an inter dependency of these parameters. In fact, the gas pressure (P) and target to substrate distance (D) are not independent. They follow an experimental law[104, 108]:

$$P \times D^r = C \quad (4.7)^{[109]},$$

where r is positive and material dependent, and C is a constant which is both material and deposition system dependent[104].

Deposition Temperature

The effects of substrate temperature on the film growth have been well studied, and there are a large number of references in the literature[95]. Generally speaking, most perovskite thin films can be epitaxially grown at a processing temperature higher than 750 °C. For instance, highly epitaxial BSTO ($Ba_xSr_{1-x}TiO_3$) thin films can be achieved at a deposition temperature of 750 – 850 °C with excellent physical properties and epitaxy[95]. In theory, a high processing temperature will benefit the epitaxial growth of such oxide thin films. However, a much too high temperature will cause the inter-diffusion reaction at the interface between the film and substrate or substrate surface reconstruction that strongly alters the physical properties of the as-grown films[95].

In general, the deposition temperature can affect the film growth mainly via two major factors. For complex oxides, if one of the cation species has a high vapor pressure, it may easily evaporate at high temperatures. Therefore, a stoichiometric growth cannot be realized and the film would have a deficiency of this species. In this way, the deposition temperature is closely related to the gas pressure. Increasing the deposition temperature has similar effect on the film stoichiometry as decreasing the gas pressure. Take the example of the deposition of $ZnGa_2O_4$ again[100], at elevated temperatures, due to the high vapor pressure of Zn compared to that of Ga, the film exhibit a significant of Zn loss.

In addition, the surface mobility of the atoms or ions is associated with the substrate temperature. Normally, films grown at room temperature are amorphous or polycrystalline. Under high growth temperatures, small crystallites can diffuse more freely to form a more ordered structure and also less porosity, thus leading to an improvement in the film crystallinity[110]. As mentioned in the previous section, film growth mode can be affected by the temperature. Especially for the layer by layer growth mode, which can facilitate the high quality film, a high temperature is necessary. This, in turn, affects the film quality.

Laser Fluence

The energy absorbed by a single atom should be above a threshold, such that the energy from the laser pulse exceeds the binding energy of the target atoms, resulting in target ablation. This energy per unit area is defined as the laser fluence or laser energy density. The area is dependent on the laser spot size on the target. Laser fluence is one of the most important parameters during thin film depositions which affects the chemical composition of the plume and thus controls the stoichiometry and crystallographic quality of the final film. However, excessive laser fluence would generate many particulates. They are big clusters with diameters ranging from 0.1 to 10 μm, which can detrimentally affect the film properties[96]. In addition, a high laser fluence would result in strong momentum for the species which can bombard the existing film on the substrate, leading to damage. On the other hand, low fluence generally results in non-stoichiometry. Usually the deposited films exhibit a lack of light (atomic mass) atoms due to the higher tendency to be scattered[95]. For example, in the study of Y/Ba ratio of $YBa_2Cu_3O_{7-x}$ thin films, where Y is lighter than Ba, the stoichiometry in the film was greatly influenced by the laser fluence. Films deposited with laser fluence below 0.4 J/cm^2 were Y-deficient and the Y/Ba ratio was less than 1:2. On the other hand, this was compensated in films grown with a high laser fluence[111]. Therefore, the laser energy density should be carefully controlled depending on the material used for deposition.

Laser Frequency

Compared to a continuous laser, a pulsed laser can avoid over-heating the optics and the target. Therefore, risks associated with high energy laser can be reduced. The laser frequency during deposition can be adjusted according to different requirements of the materials. As different atomic species have different diffusion times on a heated substrate, the laser frequency mainly affects the phase formation and film quality. A very low laser frequency results in excessive time delay between deposition pulses, which in turn results in unwanted "annealing" of the film that may affect its stoichiometry due to the loss of volatile element in the film. On the other hand, a very high laser frequency may leave less time for the ions and atoms to settle and re-arrange, resulting in poor crystallinity, secondary phases or phase inhomogeneity[95].

It was shown that in the deposition of $Pb_{1-x}La_x(Zr_{1-y}Ti_y)_{1-x/4}O_3$ thin films, by increasing the laser frequency to 15 Hz, the unwanted secondary phase (the rutile phase of TiO_2) appeared. Under such a high frequency, the species on the substrate had no time to transform to the perovskite phase. Therefore, clusters accumulated in an amorphous form and the Pb^{2+} ions were lost by re-evaporation[112].

Target

During deposition, the target is normally rotated in order to achieve uniform target consumption. After several depositions, it is necessary to polish the surface of the target because the composition of the ablated area can be totally different from the initial stoichiometry. The target conditions can have a great influence on film growth, including film epitaxy, phase constitutions, deposition rate, and particulate. It is very important to have high density and high homogeneity target, which helps reduce the formation of particulates during ablation[95].

Substrate

In thin film growth, the condition of the substrate can greatly affect the film properties. Impurities on the substrate surface would act as an agglomeration source of

the upcoming atoms during deposition, and this can give rise to unwanted islands in the film. Thus, substrates should be very clean before being mounted in the chamber.

For a perfect substrate, nucleation happens heterogeneously on the substrate surface. However, most of the time there are defects on the surface of substrate like atomic steps and dislocation intersections either due to mechanical cleavage or poor crystal quality. These defects will of no doubt offer low energy sites and thus are preferable for nucleation.

For more delicate purposes, substrates with single termination or a deliberate mis-cut (often called vicinal substrates) are often selected. Figure 4.6 is an example of the film growth on a vicinal substrate. During film growth, adatoms would nucleate at the atomic steps, and propagate towards the step edge with a smooth front, then the steps would move along the substrate surface. In this way, thin film thickness is grown step by step, or rather, layer by layer, thus achieving high quality growth of thin films. This is called the step-flow growth of thin films[113].

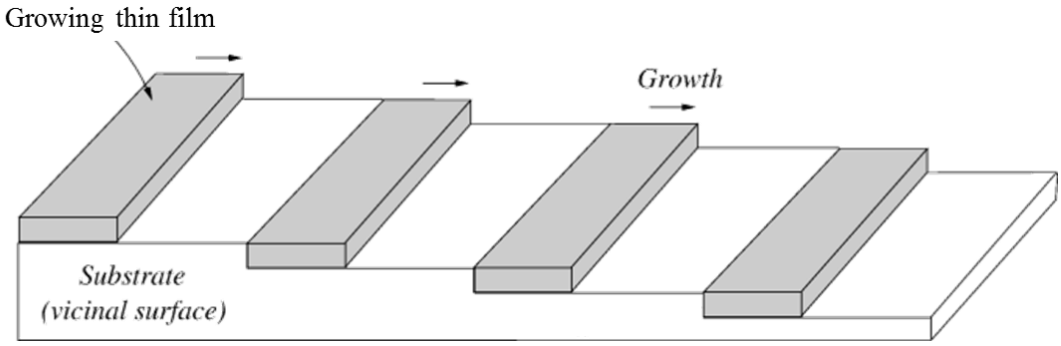

Figure 4.6 Thin film step flow on vicinal substrate[114].

Chapter 5 Characterization Techniques

This research involved characterization techniques such as x-ray diffraction (XRD), low angle x-ray reflectometry (XRR), low temperature electrical measurements, and atomic force microscopy (AFM) measurements. XRD was mainly used to identify the phase and crystal orientation of the thin film. XRR was used for film thickness calculation. Low temperature electrical measurements were mainly used to measure resistance as a function of temperature with or without applied magnetic field. AFM was used to check the topography of the film surface. These techniques are briefly discussed in the following. Section 5.1 discusses the fundamentals of XRD technique, including several heavily used scan modes in this research: θ-2θ scans, ω scans, phi scans, reciprocal space map (RSM). Section 5.2 discusses the low angle reflectometry (XRR) and high angle fringes to measure film thickness. Section 5.3 explains the resistivity measurement and the helium cooling principle, using both a dewar and a helium-3 probe in the minicryofree system. Section 5.4 is an introduction to the AFM.

5.1 XRD

It is a very powerful and non-destructive tool in material analysis. XRD is widely used in phase identification, crystal orientation or epitaxy determination, film thickness calculation, structural analysis, and strain analysis. x-rays are short wavelength electromagnetic radiations that are usually in the range between 0.05 – 0.25 nm[115]. In most cases, the wavelength is fixed and the most commonly used source is Cu Kα, with the wavelength 0.15418 nm.

In a crystal lattice, atoms are regularly distributed with long-range order. The interatomic distances are of comparable magnitude to the wavelength of x-rays. In this sense, atomic lattices are analogous to the diffraction gratings for x-rays. When the incident beam is coherently scattered by the atoms, there will be concerted constructive

interference at some specific angles. This corresponds to the diffraction peaks observed in an XRD pattern, while the background noise is from the incoherent interference. Generally speaking, the XRD pattern is a plot of diffraction intensity over a range of angles. The scan angle depends on the scanning mode, which is 2θ in a 2θ-ω scan, or ω in an ω scan. The peak intensity is mainly related to the structure of the material, the orientation, and instrumental parameters.

The x-ray diffraction process in a perfect crystal is demonstrated in Figure 5.1. Atoms in the crystal are located on the parallel planes labeled as A, B, C, etc, with the inter-planar spacing of d. The incident x-ray is monochromatic with wavelength λ. The incident angle is θ, which is defined as the Bragg angle. Incident beam 1 is diffracted by the atom to beam 1', and same occurs for other parallel beams.

For diffraction to occur, an essential condition must be fulfilled. Take beam 1 and 2 for example, in order for the diffracted beam 1' and 2' to have constructive interference, the differences in the x-ray path distance must be $n\lambda$, where n is an integer. The difference in the x-ray path length is simply $2dsin\theta$. Therefore, this essential condition can be written as:

$$2dsin\theta = n\lambda \quad (5.1).$$

This equation is also called Bragg's equation.

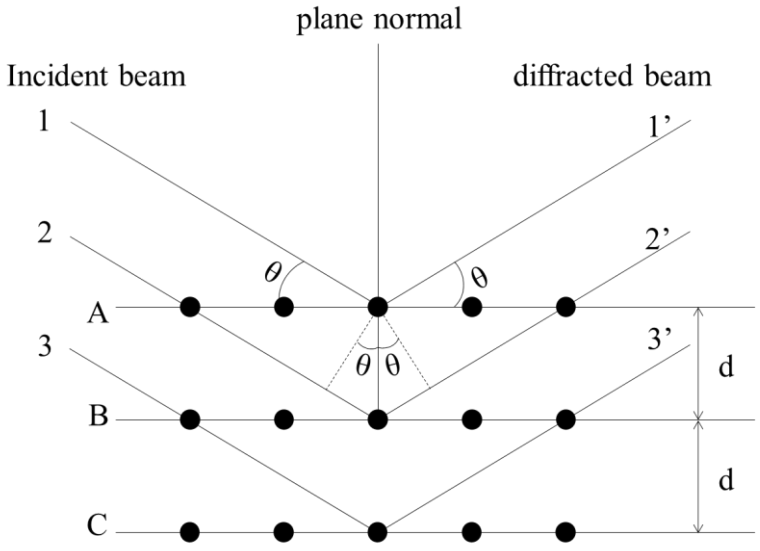

Figure 5.1 Diffraction of x-rays by a crystal[115].

In this research, XRD were performed on equipment in the department of Materials Science and Metallurgy, Cambridge. The phase identification of the PLD target was carried out on P4 Philips diffractometer. The analysis of epitaxial thin films was carried out on P1 with a four-circle Panalytical Empyrean vertical diffractometer. P4 and P1 are the local names for the two different diffractometer in the department. The commonly used XRD modes are 2θ-ω scans, ω scans or rocking curves, phi scans, reciprocal space maps (RSM). They are briefly described in the following parts.

θ-2θ Scans

The working principle of this scan mode is demonstrated in Figure 5.2, where ω is the incident angle, 2θ is the angle between detector and the x-ray source, s is the diffraction vector which bisects the incident beam and the diffracted beam. In this mode, ω is set to follow the value of θ, with a small offset which is used to align the diffraction vector to be parallel with the crystal plane normal.

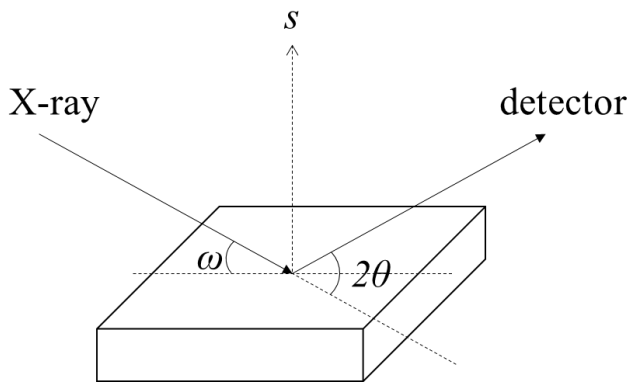

Figure 5.2 A schematic drawing of the θ-2θ scans.

This is the measurement of diffraction intensity as a function of 2θ. According to the Bragg equation, the peak position in the plot is related to the d-spacing. It contains information on the lattice parameter, which can be influenced by compositional change or strain. In the case of symmetric scans, where the crystal plane normal is parallel to the sample surface normal and $\theta = \omega$, like the (0 0 l) plane in my research, the d-spacing is reflecting the c-axis value of the film. Therefore, the *out-of-plane* strain of the film can be easily estimated; the phase of the film can be worked out by comparing the peak

positions to those in the reference; the film orientation can also be determined by the appearance of (0 0 *l*) family peaks; even the fringes in the vicinity of high intensity peaks can be used to calculate the film thickness, all these analysis will be discussed later.

In this research, this working mode is primarily used in phase identification. A phase is a specific set of chemical and atomic arrangement, and each phase has a unique diffracted pattern. If the material under investigation consists of more than two different phases, the diffracted pattern is just a simple sum of the component phases. The relative intensity of diffracted peaks and their positions can be used to match with the reference patterns so that the phase can be determined. Miller indices (*h k l*) were used to identify different planes and orientations.

Under ideal conditions in this mode, a single crystal only have one family of diffraction peaks displayed in the diffraction pattern, corresponding to (*h k l*) planes parallel with sample surface. For a polycrystalline sample, there are a large number of crystallites with random orientations. Therefore, all possible diffraction peaks can be observed, albeit some with low intensity.

ω Scan

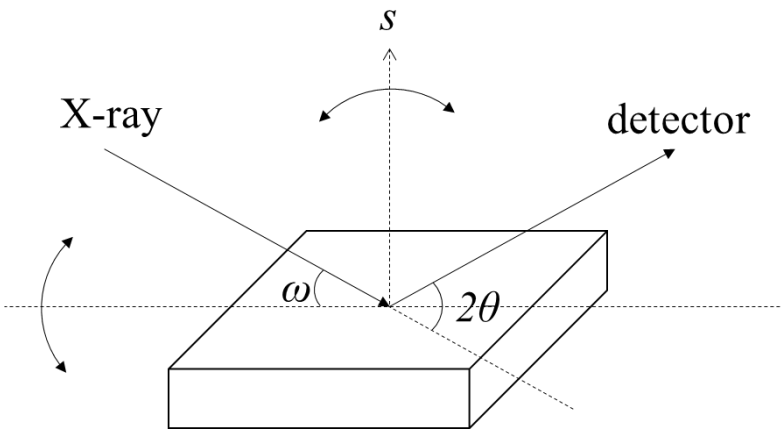

Figure 5.3 A schematic drawing of the ω scans.

ω scan is a plot of intensity as a function of. ω, which is also called rocking curve. In this mode, the sample is being rocked in a small range, while the x-ray tube and

detector are fixed as shown in Figure 5.3 (this is the case with the equipment used in this research), or the sample is being fixed while the x-ray tube and detector both move by the same angle to make sure 2θ is constant. Ideally, a well aligned (oriented) crystal has a very sharp rocking curve with a small full-width at half-maximum (FWHM) value, regardless of the broadening from the instrument. However, in real cases, there are always factors like dislocations, mosaicity (which is caused by mis-orientations of different crystals), curvature and inhomogeneity. These defects cause disruptions in the originally parallel atomic planes, and thus resulting in the broadening of the rocking curve.

Phi Scans

For thin film analysis, phi (Φ) scans are usually used to measure the *in-plane* orientation of the thin film with respect to the substrate. Phi scan is usually for asymmetric scans, where ω is not equal to θ. As shown in Figure 5.4, this is done by rotating the sample around the sample normal (sweeping the Φ angles) while measuring the intensity of a specific planar orientation, with other parameters such as ω, 2θ, and ψ (chi) being constant (ψ is illustrated in Figure 5.4).

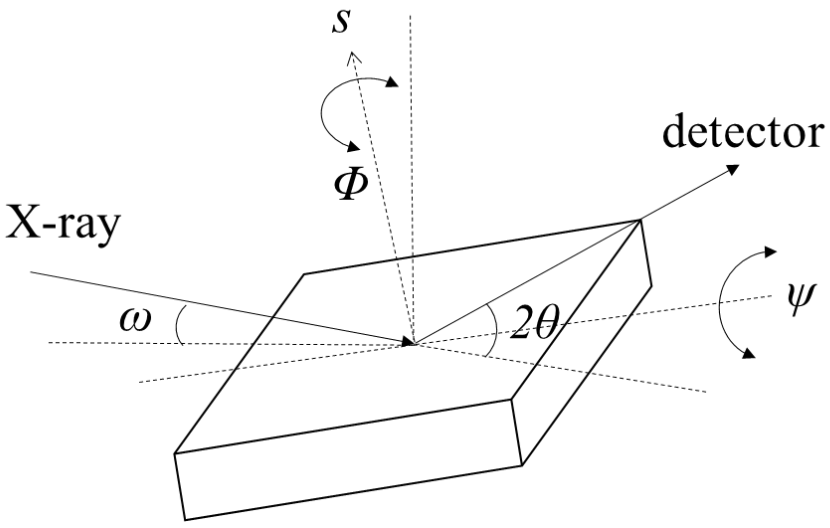

Figure 5.4 A schematic drawing of the Φ scans.

The results of phi scan can be analyzed to determine the symmetry of the crystalline phase in the film and substrate. For instance, in a tetragonal single crystal with tetrad axis parallel to the sample normal, as is the case in this work, the phi scans for inclined planes such as {103} planes will have four peaks when rotated through 360°, corresponding to reflections from (1 0 3), ($\bar{1}$ 0 3), (0 1 3), and (0 $\bar{1}$ 3).

Reciprocal Space Map

An reciprocal space map (RSM) consists of many sets of θ-2θ scans, each measured at a different ω offset. It offers a rather comprehensive structural information about a material and is frequently used in strain analysis. The map is usually presented as a contour map, and two different sets of axes can be used to present the data. As shown in Figure 5.5, they are the diffractometer axes (2θ and ω) and the reciprocal space axes (Q_x and Q_z).

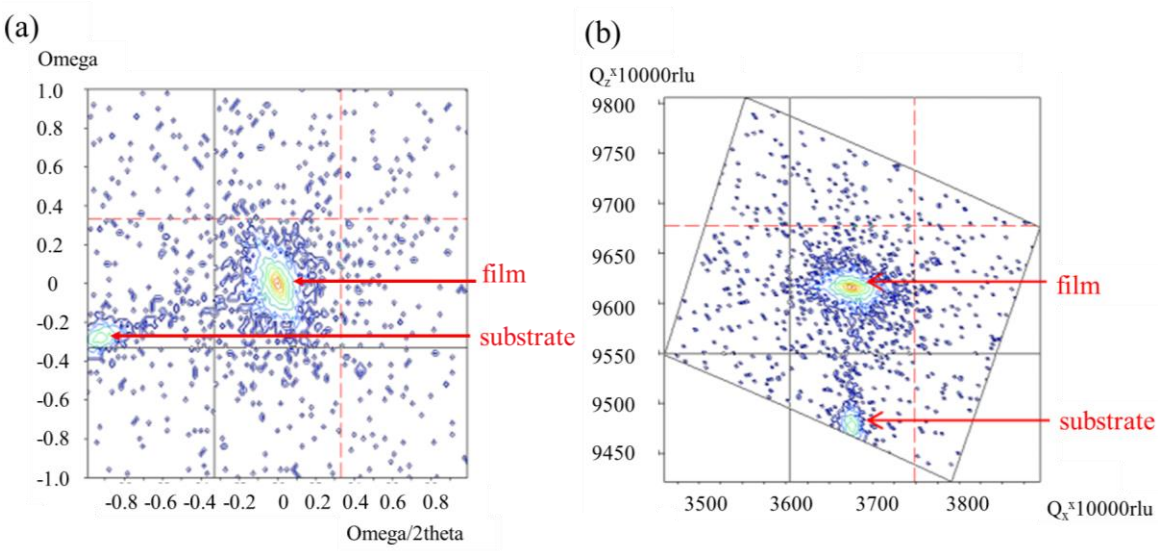

Figure 5.5 Reciprocal space map based on (a) diffractometer axes and (b) reciprocal space axes. Data extracted from Mary Vickers' lecture notes[116].

To enable easy calculation of lattice parameter, the reciprocal space map is usually plotted in Q_x and Q_z, which is essentially the inverse lattice spacing in the x and z direction of the diffracted plane, respectively. In reciprocal space, each point represents a set of (h k l) planes. By comparing the two points whether they lie parallel on the Q_x

axis, we can tell whether the film is coherently strained *in-plane* with respect to the substrate. For example, if the peaks from two reciprocal peaks of film and substrate lie parallel to each other, with the same Q_x, as shown in Figure 5.5(b), it means that the *in-plane* spacing between the planes observed in both film and substrate peaks is the same. This consequently means that the film is fully strained *in-plane* by the substrate. Moreover, the lattice parameters of both the film and substrate can be calculated based on their peak position in Figure 5.5(b). Therefore, it is more convenient to use the reciprocal space axes to present the map.

The reciprocal space axes can be converted from the diffractometer axes using the following equations[115]:

$$Q_x = \frac{cos\varpi - \cos(2\theta - \varpi)}{\lambda} \quad (5.2),$$

$$Q_z = \frac{sin\varpi + \sin(2\theta - \varpi)}{\lambda} \quad (5.3).$$

Apart from strain and lattice parameter analysis, the RSM indicates the crystalline quality of the observed phase as well. For example, a sharp peak indicates high quality film.

5.2 Low Angle Reflectivity and High Angle Fringes

Low angle reflectivity (XRR) is most commonly used to measure film thickness, surface roughness and the density of the topmost layer. It records the intensity of the x-ray beam reflected by a sample at grazing angles. The operation mode is θ-2θ mode as disccused in the XRD section. The typical range for measuremtns is 0 - 5° in θ. The principle of XRR is based on a well-known phenomenon in optics.

Optical waves have such a characteristic that they can be completely reflected below a critical angle (θ_c) when iradiating a sample surface. This is due to the differences in refractive indexes between the substance that constitute the sample interfaces. For the incident angles greater than θ_c, part of the x-ray can penetrate into the film. Therefore, reflection occurs at the top surface of the film as well as the film-substrate interface. The interference between the reflected x-rays give rise to the interference fringes which are angle dependent[91].

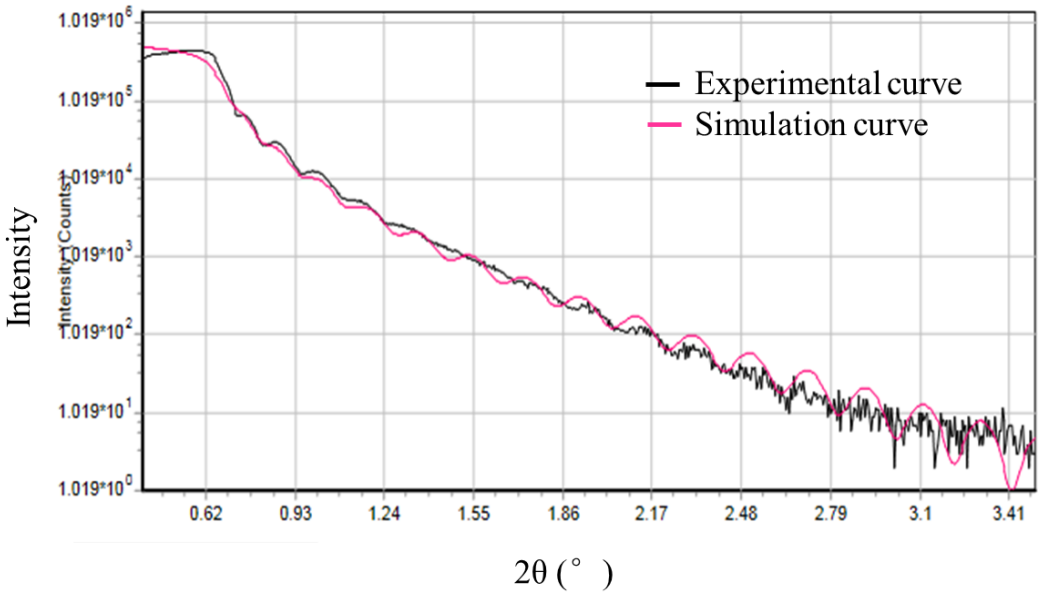

Figure 5.6 An example of the experimental XRR data and the simulation result. The simulation was carried out using software Reflectivity by PANalytical.

An example is shown in Figure 5.6, there are many periodic fringes in the plot. The period of the interference fringes and the fall in the intensity are related to the thickness and the roughness of the layer. For thin films, the separation between the

fringes is inversely proportional to the film thickness (t). It can be calculated using the following approximated equation[115]:

$$t = \frac{\lambda}{2\Delta\theta} \quad (5.4),$$

where $\Delta\theta$ is the separation (in radians) between two adjacent fringes. Sample with a rough surface scatters x-rays rather than reflecting x-rays. Therefore, the intensity of the reflected beam can quickly decay and XRR is normally used for smooth thin films to determine the film thickness.

The accuracy of this measurement depends largely on the range of the periodic fringes. For interference fringes in a big angular range, the precision is about 1 nm[115].

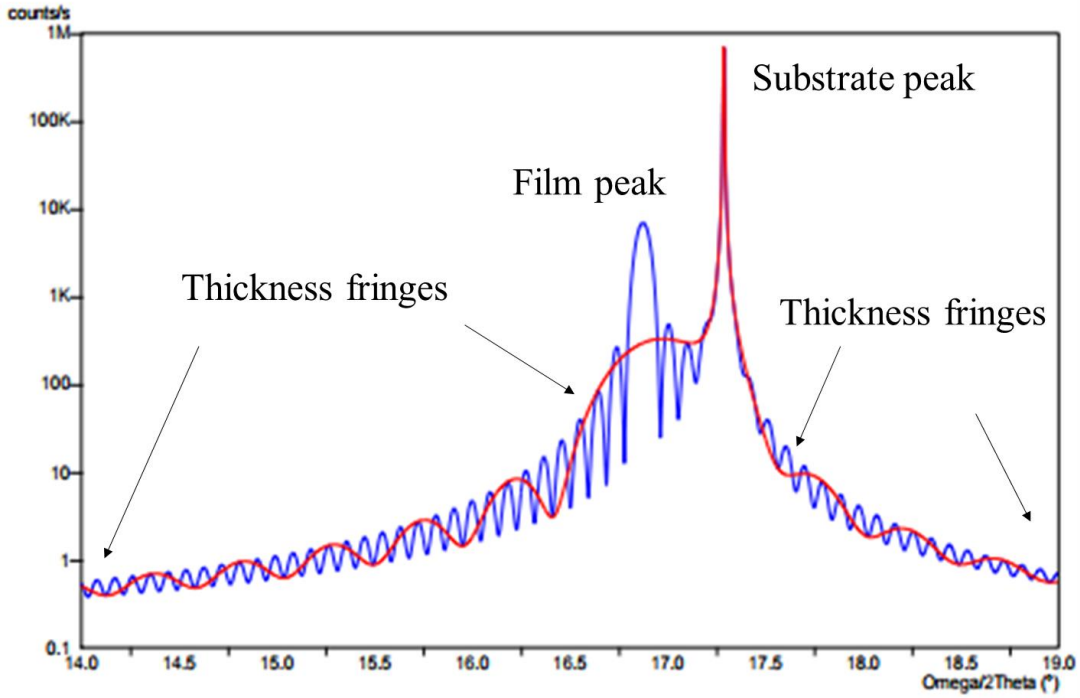

Figure 5.7 Thickness fringes for films with 50 nm (blue) and 10 nm (red). Data extracted from Mary Vickers' lecture note.

In addition, for high quality thin films, there might be fringes (especially next to the high intensity peaks) on the θ-2θ scans, which can also be used to calculate the film thickness. An example is shown in Figure 5.7. The mechanism is the same to the low angle fringes. Although in theory this technique can be applied to any sample, only those with high quality give rise to the fringes. This is because the fringes require

coherent scattering from all points in the film, any defect destroying lattice coherence could extinguish these fringes long before the primary x-ray reflection[117]. The film thickness is calculated using the following equation[115]:

$$thickness = \frac{\lambda}{2\Delta\theta * cos\theta} \quad (5.5).$$

5.3 Resistance As a Function of Temperature Measurement

The resistance was measured using a four point probe geometry as shown in Figure 5.6. In this geometry, current is applied to the outer electrodes and the potential drop is detected between the inner electrodes. Compared to the two point probe geometry, four point probe geometry avoids measuring the resistance of the connecting leads. This means when the sample becomes superconducting, the measured resistance is zero and not some finite values due to the contribution from the connecting leads.

In this thesis, sample resistance was measured by wire bonding electrodes on the plain films, without any other patterning. The spacing between two electrodes on the sample is usually about 0.5 – 1 mm.

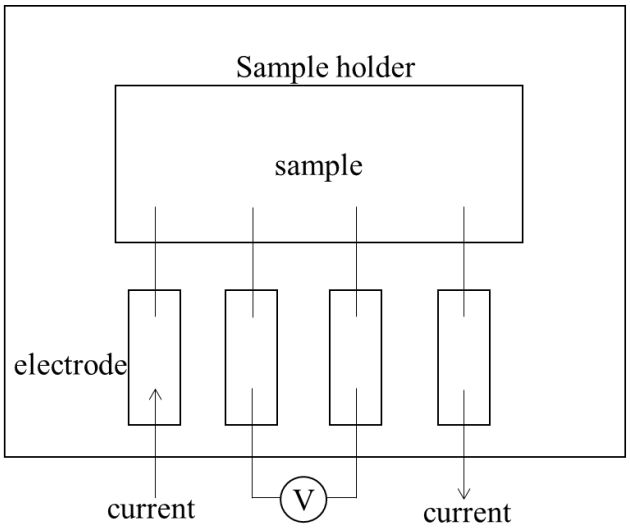

Figure 5.6 Illustration of the four-point probe geometry.

The resistance measurements were carried out in two cooling systems because of different temperature requirements: one is the helium-4 dewar for temperature range between 4.2 K - 300 K; the other one is the helium-3 probe for temperature range between 0.3 K - 300 K. The reason is explained as follows.

Although Sr_2RuO_4 is superconducting at 1.5 K, the Sr_2RuO_4 thin films from early

depositions were neither superconducting nor fully conductive down to 0.3 K. Instead, they either behaved like an insulator or a metal-insulator. In that case, it is not necessary to cool down to 0.3 K. A quick way to check the transport properties of the film is to use the helium dewar, which can be quickly cooled down to 4.2 K and this temperature range (from 300 K to 4.2 K) is enough as a first check for the Sr_2RuO_4 thin films. For Sr_2RuO_4 thin films that were fully metallic down to 4.2 K, further cooling was required to characterize the low temperature behavior of the film. Therefore, temperatures below 1.5 K were necessary in order to check whether the films were superconducting or not. In this situation, helium-3 probe in the minicryofree system is used to achieve temperature down to 0.3 K. Besides, the minicryofree is equipped with a magnetic field up to 1 T, proving some crucial field dependent data for Sr_2RuO_4 thin films.

5.3.1 T_c Probe in Helium Dewar

Liquid helium is stored in a special vessel called dewar. The resistance was measured by mounting the sample onto a T_c sample holder, which is connected to home made T_c probe. The T_c sample holder is a copper pad with eight electrodes and the sample was wire bonded to the electrodes using the four point probe geometry. By slowly dipping the probe into the dewar, liquid helium-4 boils as heat is taken away by the evaporation. In this way, the temperature can be cooled down, providing the resistance as a function of temperature data down to 4.2 K.

5.3.2 Helium-3 Probe in Minicryofree

For temperature range between 0.3 K - 300 K, the measurements were carried out using the helium-3 probe in minicryofree system. The minicryofree is a vacuum insulated chamber used to support and thermally shield the superconducting magnet and variable temperature insert (VTI).

Figure 5.7 is a brief description of the cooling principle of the system. At room temperature, the helium gas (helium-4) is stored in the helium dump. It goes into the VTI via the gas inlet and gets purified after the charcoal filter. After the heat exchanger,

the helium-4 gas is cooled down below its boiling point (4.2 K) and condenses in the helium pot. Then the liquid helium-4 expands after flowing through the needle valve and is further cooled down to about 1.6 K as it expands. It can be warmed through the VTI heat exchanger when necessary. The helium-4 gas flows past the sample and then back to the helium dump.

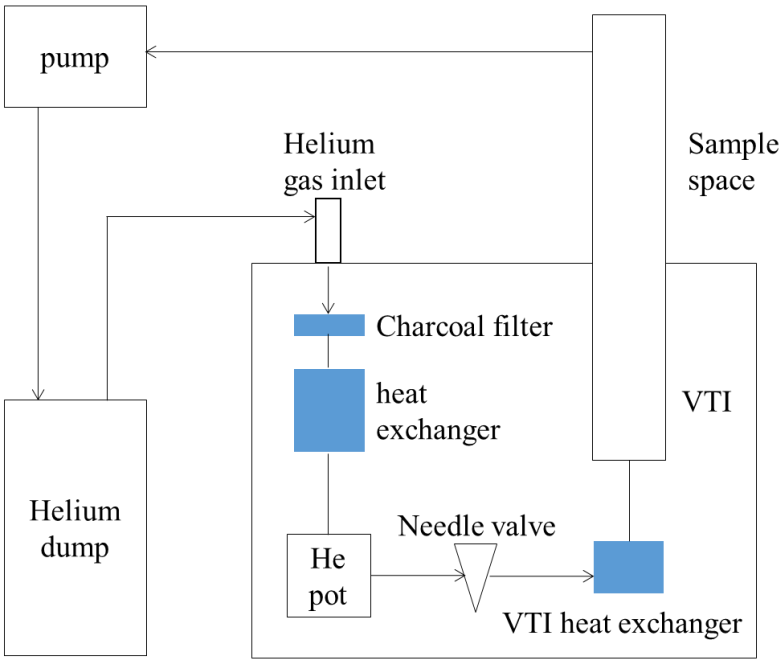

Figure 5.7 Illustration of the helium-4 cooling principle of the minicryofree. Replotted from the minicryofree manual.

Temperatures down to 0.3 K are achieved in the helium-3 probe, which is more complicated. A schematic drawing of the helium-3 probe is illustrated in Figure 5.8. The helium-3 gas is contained in the helium-3 dump in the probe. Two charcoal sorption pumps (main sorption pump and the mini sorption pump) are used in pumping and thermal isolation of liquid helium-3. Basically, the main sorption pump is to control the liquid helium-3 vapor pressure; while the mini sorption pump is to control the amount of the helium-4 exchange gas in the inner vacuum chamber (IVC). The typical cooling cycle is as follows. The helium-3 probe is inserted into the sample space in minicryofree, and first gets cooled down from room temperature by setting the VTI at 1.6 K, following

the cooling process discussed above. During this process when the main sorption pump reaches 40 K, the helium-3 gas is completely desorbed into the helium-3 pot. When the mini sorption pump reaches 25 K, the helium-3 pot gets cooled by desorbing the helium-4 exchange gas into the IVC. When the helium-3 pot is cooled down to 2 K, all the helium-3 gas is fully condensed. Then the main sorption pump is set to 1 K, as the temperature drops, the vapor pressure of liquid helium-3 in the helium-3 pot also drops. In the meanwhile, the mini sorption pump is set to 1 K, which absorbed the helium-4 exchange gas from the IVC and thermally isolate the helium-3 pot. Finally, by pumping the main sorption pump on the condensed helium-3, the helium-3 pot is reduced to 0.3 K.

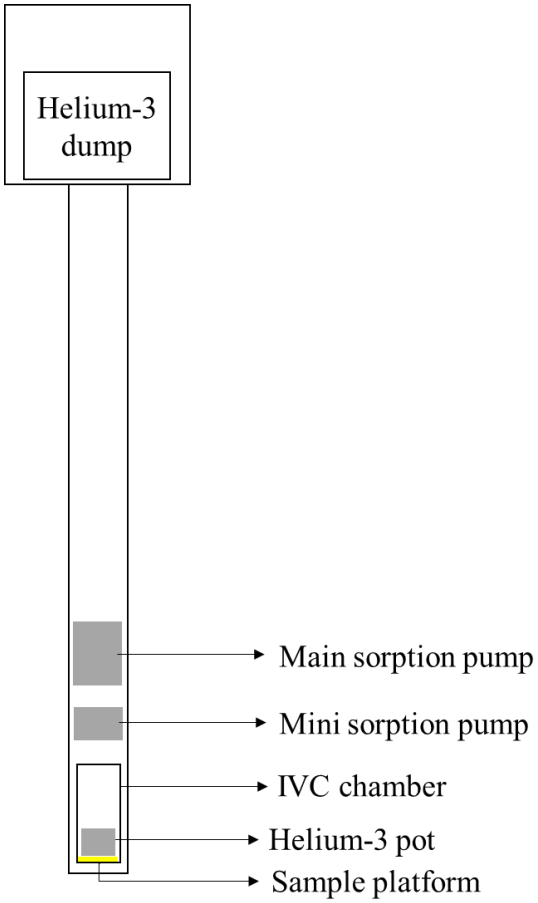

Figure 5.8 Illustration of the helium-3 probe, which would be inserted into the sample space in Figure 5.7 during measurement. Replotted from the helium-3 probe manual.

5.4 AFM

The surface topography of some of the thin films have been measured by AFM on the scale from micrometer down to nanometer range. The basic working principle is demonstrated in Figure 5.9. The sample surface is scanned by a cantilever with an atomically sharp tip. When the tip is close enough to have interaction with the sample surface, the cantilever can be deflected. The deflection is then monitored by a diode laser, reflecting from the back of the cantilever towards a photodetector. The photodetector is used to monitor and amplify the cantilever deflection. A surface topography image is therefore built up. A feedback circuit is used to control the tip-sample distance in order to maintain a constant force and avoid damage the tip or the sample[118].

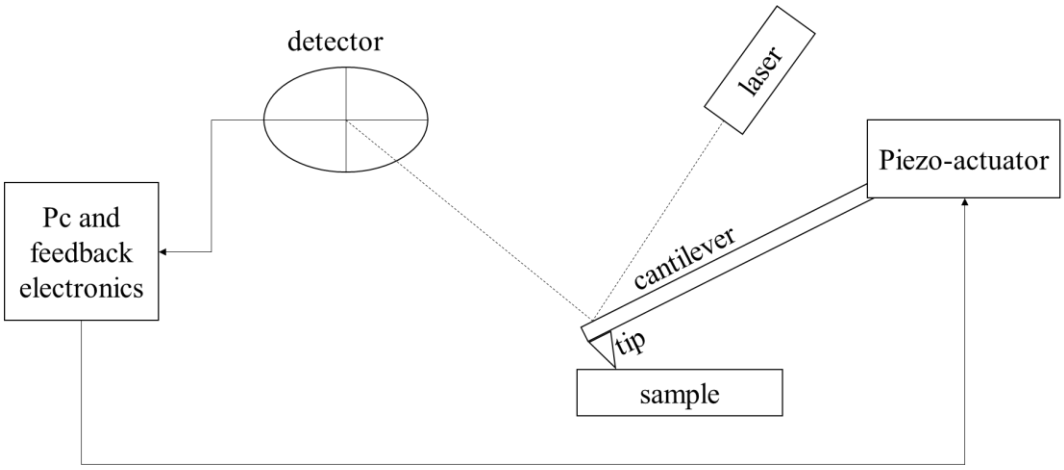

Figure 5.9 A schematic drawing of the AFM working principle[118].

One of the most commonly used working modes in AFM is the tapping mode. In this mode, the cantilever is driven at or slightly below its resonance frequency with the tip slightly taps on the surface of the sample, making contact with the sample at the bottom of its swing. During scanning, when the tip is still far from the sample surface, the cantilever oscillates at a constant amplitude. When the tip is brought close to the sample surface, several forces including the Coulombic and van der Waals interaction contribute to the movement of the cantilever. As a result, the effective resonance frequency and the oscillation amplitude of the cantilever is dampened as it approaches

the sample surface. The amplitude would first gradually reduce, followed by a sudden drop when the tip-sample distance is close enough that the tip completely sticks to the sample surface. The change in the oscillation amplitude is used to measure the tip-sample distance[118].

The AFM measurements in this thesis were carried out on the AFM in my group: Multimode SPM Nanoscope III. Software WSxM 5.0 develop was used to analyze the AFM data[119].

Chapter 6 Growth and Optimization of Metallic c-axis Oriented Epitaxial Sr_2RuO_4 Thin Films

As mentioned in Chapter 3, currently there are many research groups trying to grow superconducting Sr_2RuO_4 thin films using either PLD or MBE. Unfortunately, despite the efforts, the results are not so satisfactory compared to the growth of superconducting single crystal Sr_2RuO_4. Before this work, there was only one superconducting Sr_2RuO_4 thin film reported in 2010[14], and no following report afterwards. The extreme sensitivity of superconductivity in Sr_2RuO_4 to impurities and disorder makes it a challenging task to grow superconducting Sr_2RuO_4 thin films.

To make things easier and tackle the problem progressively, I started out by identifying the optimum deposition parameters or parameter windows to grow c-axis oriented epitaxial Sr_2RuO_4 thin films. This is the first part of this chapter. The process started with target fabrication and substrate selection, and then with the optimization of deposition parameters. The second part of this chapter is the improvement of transport properties from metal-insulating Sr_2RuO_4 films to metallic Sr_2RuO_4 films, which involves fine tuning of some key deposition parameters.

6.1 Phase Optimization for c-axis Epitaxial Sr_2RuO_4 Thin Films on LSAT Substrates

6.1.1 Target Fabrication

It is known that Sr_2RuO_4 thin films grown from a pure target have fewer defects than those grown from a less pure target[17]. Therefore, a target with high level of purity is the key step for successful growth of superconducting Sr_2RuO_4 thin films. Due to the fact that there is no commercial Sr_2RuO_4 target available, all the Sr_2RuO_4 targets involved in this research are hand-made via a solid reaction process[18].

The starting powders were $SrCO_3$ (Alfa Aesar, 99%) and RuO_2 (Alfa Aesar, 99.9%). Powders were pre-heated to remove moisture in order to be accurate when weighing. After weighing, the appropriate proportions of powders were carefully mixed in the mortar by continuously grinding with a pestle. The mixing process was carried out manually until the color of the mixture powders ($SrCO_3$ is white and RuO_2 is black) was fully uniform, at least to the naked eyes (e.g. no white spots visible). After that, they were transferred to a die and pressed into a pellet (1 inch in diameter and 5-6 mm thick, thickness of the pellet depended on the amount of powders being pressed). The pellet was then sintered in a clean tube furnace. In the first cycle of sintering process, the pellet was sintered at 1200 °C in oxygen atmosphere with a heating rate set at 5 °C/min. This was followed by a 24 hours dwelling period, which was to make sure that the starting powders had fully reacted. Subsequently, the pellet was cooled down to room temperature in the same oxygen atmosphere with the cooling rate set at 5 °C/min. After the first cycle of sintering, the as-sintered pellet was loose and porous, and crumbled even by a slight touch. Moreover, it was very easy to crack. Therefore, the pellet was further re-ground into powders, pressed into a new pellet, and underwent the same sintering process again. After the second cycle of sintering, the target was dense and hard. This re-sintering process reduced the porosity of the target. In order to make a dense and high quality target, the pellet was usually ground and sintered twice.

Three targets were made in this research and their only difference was the ratios of the starting powders in terms of atomic percentage. The first target had Sr/Ru = 2.1:1. As the Sr/Ru ratio in Sr_2RuO_4 phase is the highest among other Sr-Ru-O phases, it makes sense to have more Sr in the target to ensure that only the Sr_2RuO_4 phase can exist in the target. However, due to Sr excess, another unexpected phase: SrO was found to be present in every film. The details are shown in the subsequent section. Therefore, a second target which had a ratio of Sr/Ru = 2:1 was made. However, it was still difficult to get rid of the SrO extra phase in the films grown with this target. The major reason for the extra SrO phase observed in films grown from both the first two targets can be associated with Ru deficiency. At high target sintering temperatures, any volatile

species in the target could be lost during sintering, especially near the surface. Given the fact that Ru can be easily oxidized into RuO_4, which is gaseous at high temperature, it can therefore lead to Ru loss in the target[7]. Therefore, it is possible that both the first two targets were Ru deficient after two rounds of sintering, and have more tendency to form SrO extra phase.

Lastly, a straightforward way to compensate for the species loss and maintain the target stoichiometry is to add an excess amount of the volatile component to the starting powders. In the third Sr_2RuO_4 target, an excess of 15 at% RuO_2 powder was added into the initial mixture of powders. This is also the same recipe for growing single crystal Sr_2RuO_4[7]. This target subsequently consisted of phase Sr_2RuO_4, and therefore was used for the rest of the work. After several rounds of grinding and sintering, the final target was polycrystalline, as shown in the XRD results in Figure 6.1 which shows that all peaks from the target match those of the Sr_2RuO_4 reference peaks.

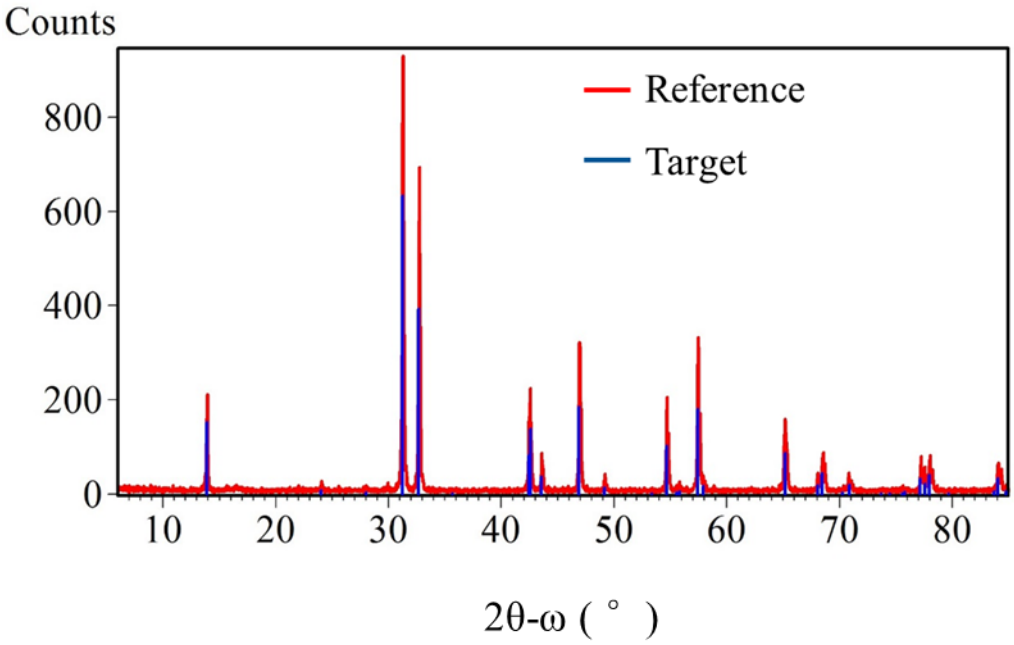

Figure 6.1 x-ray diffraction on the Sr_2RuO_4 target with 15 at% Ru excess in the starting powder and the reference (JCPDS No. 01-082-1096) pattern.

During deposition, high energy laser can severely change the composition and the

morphology of the target surface due to localized partial melting[96]. Therefore, polishing using sand paper was done on the target surface after every deposition to ensure that the compositional change from previous deposition will not affect the subsequent deposition.

6.1.2 Substrate

As already stated in Chapter 4, the lattice mismatch between the substrate and the film has an important impact on film epitaxy. Therefore, the lattice parameter of the substrates is the first criteria to be considered when selecting a substrate material. Several different single crystal substrates were compared, including the commonly used ones and those mentioned in other groups' reports: $(LaAlO_3)_{0.3}(SrAl_{0.5}Ta_{0.5}O_3)_{0.7}$ (LSAT), $SrTiO_3$ (STO), $LaAlO_3$ (LAO). Except for the lattice mismatch at room temperature, the lattice mismatch at high temperature (growth temperature) and low temperature (measurement temperature) have also to be taken into consideration. The thermal expansion mismatch between substrate and film might induce strain or defects into the thin films.

Unfortunately there is no study on the lattice parameters of Sr_2RuO_4 at high temperature at the moment, and no reports on the thermal expansion coefficient, either[120]. An indirect way would be to compare the thermal expansion coefficient of the different substrates in Table 6.1. At room temperature, the lattice mismatch between Sr_2RuO_4 and LSAT is the smallest. LSAT has the smallest thermal expansion coefficient[121] among LSAT, STO, and LAO, which indicates a minimum lattice parameter change either under heating or cooling. In addition, the perovskite structure of LSAT can facilitate the epitaxial growth of Sr_2RuO_4. Therefore, LSAT was chosen as the substrate. All LSAT single crystal substrates in this project were ordered from CrysTec Gmbh.

Every time before deposition, substrates were ultrasonically cleaned in a bath of distilled water, acetone and isopropyl alcohol (IPA), sequentially for 15 min, and dried with compressed air. Right after cleaning, the substrate was mounted onto a resistive

heater using silver paint, which guarantees not only a good adhesion to the heater but also a good thermal conductance between the heater and the substrate. As the reported deposition temperature window for high quality Sr_2RuO_4 thin film is less than 10 °C[14], it is important to make sure a good temperature uniformity so that the Sr_2RuO_4 thin film is homogeneous. The substrate was heated up in a step-heating mode to avoid any thermal shock, with heating rate of about 10 °C/min. After reaching the desired temperature, the substrate was kept for about 10 minutes to make sure the substrate is uniformly heated. After the deposition, the substrate was cooled down to room temperature at cooling rate of 10 °C/min in the same oxygen pressure as during deposition.

Material	Lattice parameter (nm)	Lattice mismatch vs Sr_2RuO_4 (%)	Thermal expansion coefficient (K^{-1})
Sr_2RuO_4	0.3873	N.A.	Not reported
LSAT	0.5468	0.16*	8.2×10^{-6}
STO	0.3905	0.90	9×10^{-6}
LAO	0.3821	1.27	10×10^{-6}

Table 6.1 Lattice parameter comparison between Sr_2RuO_4 and other (0 0 1) oriented single crystal substrates at room temperature. The lattice parameters and thermal expansion of LSAT, STO and LAO are all provided by CrysTec Gmbh. The lattice parameter of Sr_2RuO_4 is from JCPDS No. 01-082-1096. The lattice mismatch was calculated using equation 4.4. Unless otherwise mentioned, the orientation concerned in this report is (0 0 1). *It should be noted that Sr_2RuO_4 grown on the LSAT substrate has to undergo a 45° *in-plane* rotation in order to minimize the lattice mismatch to 0.16%.

From Table 6.1, it seems that there is a big difference in the *in-plane* lattice parameters between Sr_2RuO_4 and LSAT. However, in epitaxial thin film growth, if the difference in lattice parameters between substrate and film is very large, the film will have tendency to rotate 45° *in-plane* to minimize the lattice mismatch. In my case,

Sr_2RuO_4 unit cells indeed undergoes 45° *in-plane* rotation, as schematically illustrated in Figure 6.2. (XRD results presented in Chapter 7 show evidence of this rotation in Figure 7.1 (c)). The *in-plane* lattice parameter after 45° *in-plane* rotation for Sr_2RuO_4 is 0.3873 x √2 = 0. 5477 nm, resulting in only 0.16% difference with the lattice parameter of LSAT.

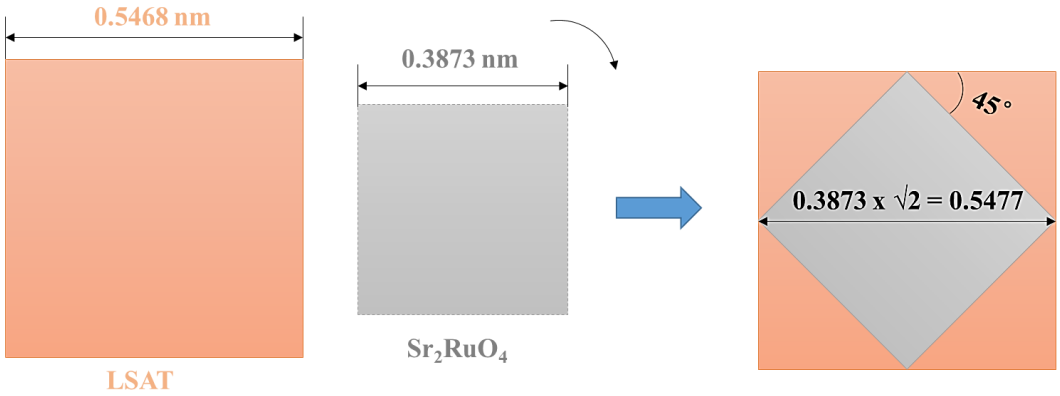

Figure 6.2. Schematic showing the *in-plane* rotation of Sr_2RuO_4 film unit cell on the LSAT substrate.

6.1.3 The Influence of Deposition Parameters on Thin Film Phase Composition

In this research, the "106 PLD" system in my group with a KrF laser (from Lambda physik) was used. To begin with, a good vacuum is essential towards a high quality thin film. The "106 PLD" system normally can reach a base pressure between 10^{-8} to 10^{-9} mbar after an overnight baking and pumping. In addition, chamber leakage was tested every time before the deposition to make sure the vacuum for every deposition was consistent. Once the desired deposition temperature is reached, the system was left at that temperature for about 10 mins to make sure the substrate was at a uniform temperature. In the meanwhile, O_2 was let in through the needle valve which was connected to a O_2 reservoir. The laser energy and ablation frequency were also set at the same time. The target was first pre-ablated for about 100 pulses, while the

substrate was covered by a shutter. The purpose of the pre-ablation is to remove any dirt and impurities on the target surface and leave a fresh surface for the real deposition. After all the preparations, deposition was started at the chosen parameters. When the deposition finished, the chamber was cooled down to room temperature with O_2 flow.

Although the PLD target phase was known, it does not mean the composition of the film would be the same as that of the target. Due to the difference in particle mass, charge, vapor pressure, and sticking coefficient of the target species, the composition of the film is expected to be greatly affected by many deposition parameters such as the gas pressure, deposition temperature, target to substrate distance, and laser fluence. In the case of Sr-Ru-O, there could be a competition among the formation of several different crystalline phases: SrO, Sr_2RuO_4, $Sr_3Ru_2O_7$ and $SrRuO_3$. Therefore, the growth of Sr_2RuO_4 thin films requires the delivery of the right ratio of species to the substrates.

A survey of all the reported growth of Sr_2RuO_4 thin films by PLD was recorded in Chapter 3. In spite of this, the divergence in some of the deposition parameters and the wide selection of deposition parameters made it difficult to select starting conditions. Therefore, a careful optimization was necessary to make sure the composition does not deviate from the desired one. To make things easy and clear, the optimization was started by adjusting one parameter at a time: background gas pressure, deposition temperature, target to substrate distance and laser fluence. When one parameter was changed, the others were kept constant. The following part is a systematic study of the influence of the deposition parameters on the film composition.

Oxygen Pressure

The addition of oxygen during deposition is necessary for oxide thin films, which not only serves as a background gas but also as a reactive gas. Pure oxygen was used in the depositions. The phases of the Sr-Ru-O thin films were characterized by XRD, as shown in Figure 6.3. Different phases have different thermodynamic stabilities and therefore require different amount of oxygen[95]. With the increase in oxygen pressure,

the dominant phases in Sr-Ru-O thin films were identified in order from SrO, Sr_2RuO_4 + SrO, Sr_2RuO_4, Sr_2RuO_4 + $SrRuO_3$, and $SrRuO_3$. This trend is consistent with the chemical equilibrium of the Sr-Ru-O phases with different oxygen amount, as found in the bulk Sr-Ru-O system:

$$Sr_2RuO_4 \leftrightharpoons 2SrO + Ru + O_2 \quad (6.1),$$

$$2SrRuO_3 \leftrightharpoons Sr_2RuO_4 + Ru + O_2 \quad (6.2)^{[122]}.$$

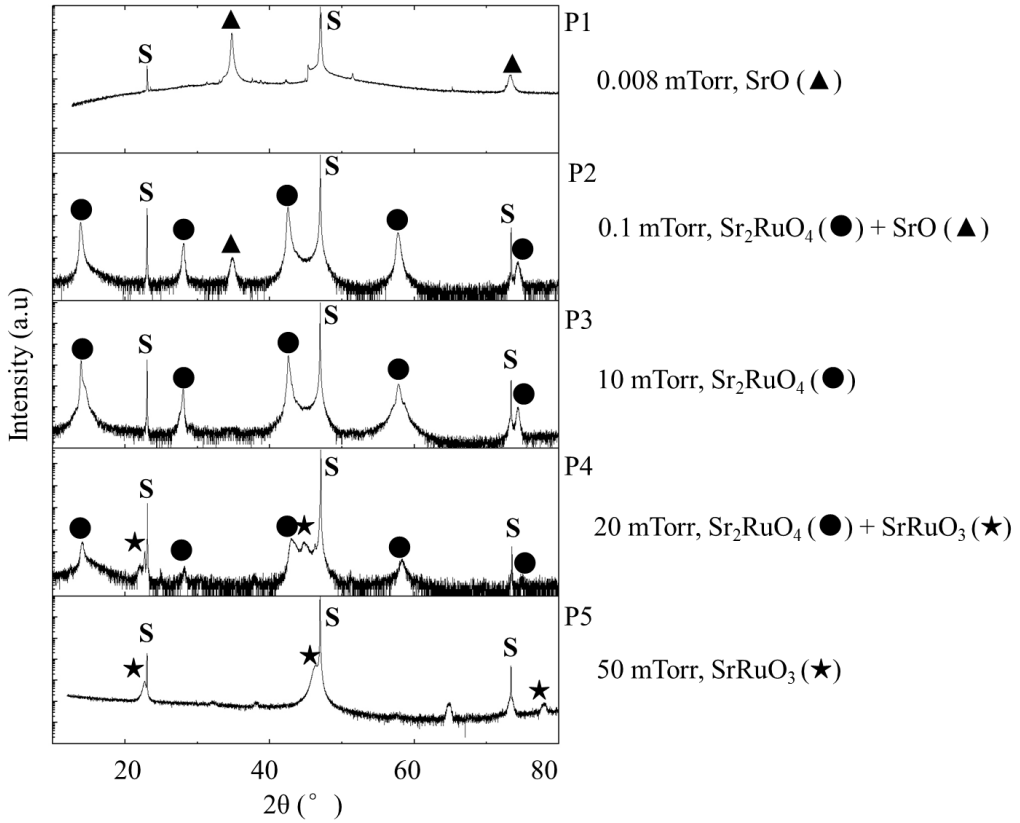

Figure 6.3 XRD results of composition in the Sr-Ru-O film with the change in oxygen pressure presented on a log scale, with the sample names to the right. The influence of the oxygen pressure on Sr-Ru-O thin films was studied by adjusting the oxygen pressure from low to high while the deposition temperature was set at 950 ℃, target to substrate distance at 7.5 cm, laser fluence at 1.5 J/cm^2, laser ablation frequency at 8 Hz, and repetition of 6000 pulses. Heating and cooling of substrate was done at a rate of 10 °C/minute. The peaks in the XRD have been identified by comparing to the reference data (JCPDS No. 01-082-1096). S denotes the LSAT substrate. All the peaks for Sr_2RuO_4 identified were (0 0 1) oriented. The thicknesses of the samples are given in Table 6.2.

The above chemical reactions are for illustration purposes, and by no means represent the real PLD growth process, which involves high density plasma that cannot be simply described using simple reaction equations. In reaction (6.1), more oxygen in the system would make the reaction more favorable towards the left side, and thus easier for Sr_2RuO_4 to be formed. However, as shown in reaction (6.2), too much oxygen in the system would facilitate the further formation of $SrRuO_3$. Therefore, as the oxygen pressure is increased, the phase in the film changed from Sr-rich phase (Sr_2RuO_4) to Ru-rich phase ($SrRuO_3$).

In addition, as mentioned in Chapter 4, the oxygen pressure has a great influence on species with high vapor pressures. In Sr-Ru-O series, Ru has a high vapor pressure, because it forms RuO_4 gas with a boiling temperature of only 40 °C[123]. Therefore, films grown at low oxygen pressures tend to have less Ru. As mentioned in Chapter 4, the loss of species with high vapor pressure can be compensated by increasing the pressure. My result is consistent with this in that at high oxygen pressure, Sr_2RuO_4 formation was favorable. Similar results have been found in Pb-Zr-Ti-O thin film depositions. Pb deficiency was found in films grown at low pressures, but not in films grown at high pressures[124].

Finally, it has to be noted that the gas pressure can affect the film thickness. The film thicknesses were estimated from x-ray fringes, more details can be found in Appendix I. As shown in Table 6.2, as the pressure increased, the film thickness decreased, with the exception that film deposited at 0.008 mTorr was not in trend. The reason is that high pressure reduces the kinetic energy of the plume and creates more scattering, causing a lower deposition rate. Therefore, for the same number of laser pulses, films grown at high pressure are thinner[95]. However, for films grown at extremely low pressures, the plume becomes widely expanded due to fewer collisions with the gas molecules, therefore, reducing deposition rate and giving rise to a thin film[96]. This may explain exception for the film deposited at 0.008 mTorr.

Sample	Oxygen pressure (mTorr)	Thickness (nm)
P1	0.008	48 ± 5
P2	0.1	63 ± 5
P3	10	57 ± 3
P4	20	43 ± 3
P5	50	36 ± 2

Table 6.2 Thickness of the Sr-Ru-O films in Figure 6.3. The thicknesses were estimated from x-ray fringes, the estimation of the thickness and thickness errors from x-ray fringes can be found in Appendix I.

Deposition Temperature

Deposition temperature greatly affects the nucleation process[96] by means of activation energy. To some extent, it influences which phase nucleates on the substrate. Normally for thin film growth, the temperature should be high enough so that the atoms can get sufficient surface diffusion and thus minimize the surface energy[96]. However, for some complex oxides, some cation species which have high vapor pressures may be lost during deposition[95] at high temperatures. Therefore, a stoichiometric growth cannot be realized. In this way, the deposition temperature is closely related to the gas pressure. In this specific case, increasing the deposition temperature has similar effect on the film stoichiometry as decreasing the gas pressure.

In the case of Sr-Ru-O thin film deposition, as already discussed, Ru has a high vapor pressure and easily evaporate in the form of RuO_4[125]. As can be seen in Figure 6.4, with the increase in temperature, the dominant phases in Sr-Ru-O thin films were identified as $SrRuO_3$, Sr_2RuO_4 + $SrRuO_3$, Sr_2RuO_4, and Sr_2RuO_4 + SrO, progressively. It is clear that Ru-rich phases such as $SrRuO_3$ formed at relative low temperatures while Sr-rich phases such as Sr_2RuO_4 formed at relative high temperatures, consistent with the Ru evaporation. This is consistent with the reports on $ZnGa_2O_4$[100], due to the high vapor pressure of Zn compared to that of Ga, the film exhibit a significant of Zn loss at

elevated temperatures. Therefore, the deposition temperature cannot be too high.

In general, deposition temperature might slightly affect the film thickness because the sticking coefficient of the atomic species is closely related to temperature and generally porous films have higher thicknesses[96]. However, in my depositions, due to the small temperature window, the thickness variations shown in Figure 6.4 were not obvious enough to draw any conclusion, the results are shown in Table 6.3.

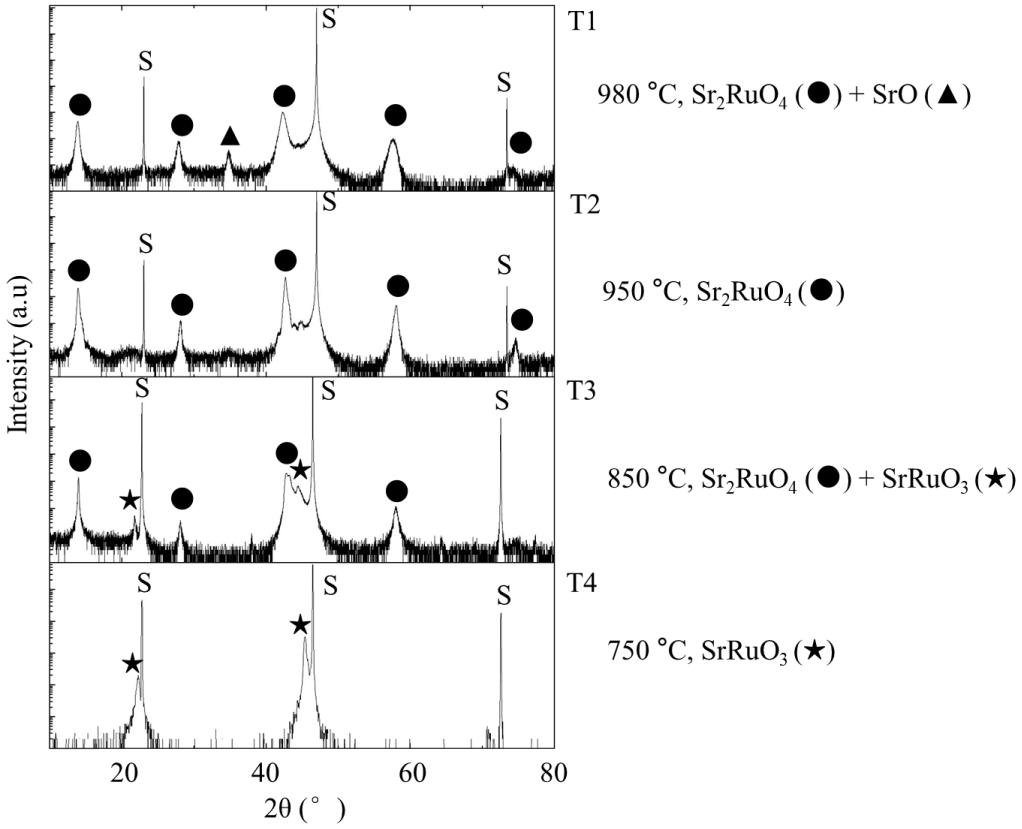

Figure 6.4 XRD results of Sr-Ru-O composition in the film with the change in deposition temperature presented on a log scale, and the sample names are to the right. While the temperature was adjusted from low to high, the oxygen pressure was set at 10 mTorr, the target to substrate distance at 7.5 cm and the laser fluence at 1.5 J/cm^2, laser ablation frequency 8 Hz, and total repetition of 6000 pulses. Heating and cooling rate was maintained at 10 °C/minute. The peaks in the XRD have been identified by comparing to the reference data (JCPDS No. 01-082-1096). S denotes the LSAT substrate. All the peaks for Sr_2RuO_4 identified were (0 0 1) oriented. The film thicknesses were shown in Table 6.3.

Sample	Temperature (°C)	Thickness (nm)
T1	980	58 ± 3
T2	950	55 ± 4
T3	850	60 ± 2
T4	750	52 ± 5

Table 6.3 Thickness of the films in Figure 6.4. The thicknesses were estimated from x-ray fringes, the estimation of the thickness and thickness errors from x-ray fringes can be found in Appendix I.

Target to Substrate Distance

With the increase in this distance, the dominant phases in Sr-Ru-O thin films were identified as Sr_2RuO_4, Sr_2RuO_4 + $SrRuO_3$, and $SrRuO_3$, as shown in Figure 6.5. It is obvious that the target to substrate distance (D) affects the phases in the films. Films grown in a relative short D tend to have Sr-rich phases, while those grown in a relative long distance have Ru-rich phase.

This can be understood in terms of the plume propagation during deposition. Within the distance from target to substrate, the energy and the composition of the particles as well as the ion density in the plume vary a lot[95]. Due to the existence of gas in the chamber, all species constituting the plume can be scattered and thermalized. In this process, particles which are light in mass are more prone to be scattered. In the case of Sr-Ru-O, Sr is lighter than Ru. Therefore, within the distance from target to substrate, Sr was more easily scattered than Ru. If D is short, the scattering of Sr was not significant. However, for relatively longer D, the scattering of Sr was significant enough to cause Sr loss and thus resulted in a Ru-rich phase in the film. Therefore, films grown at short distances are Sr-rich, while those grown at long distances are Ru-rich. Similarly, this preferential scattering of lighter atoms over long target to substrate distance is also found in the deposition of $SrTiO_3$ (Ti is ligher than Sr) thin films. Sr-rich phases were found to dominate in films grown at long D values, whereas Ti-rich phases were was found in films grown at short D[107].

In addition, D is related to the gas pressure (P), following the aforementioned empirical law[104, 108] in Chapter 4:

$$P \times D^r = C \qquad (6.3)^{[109]}.$$

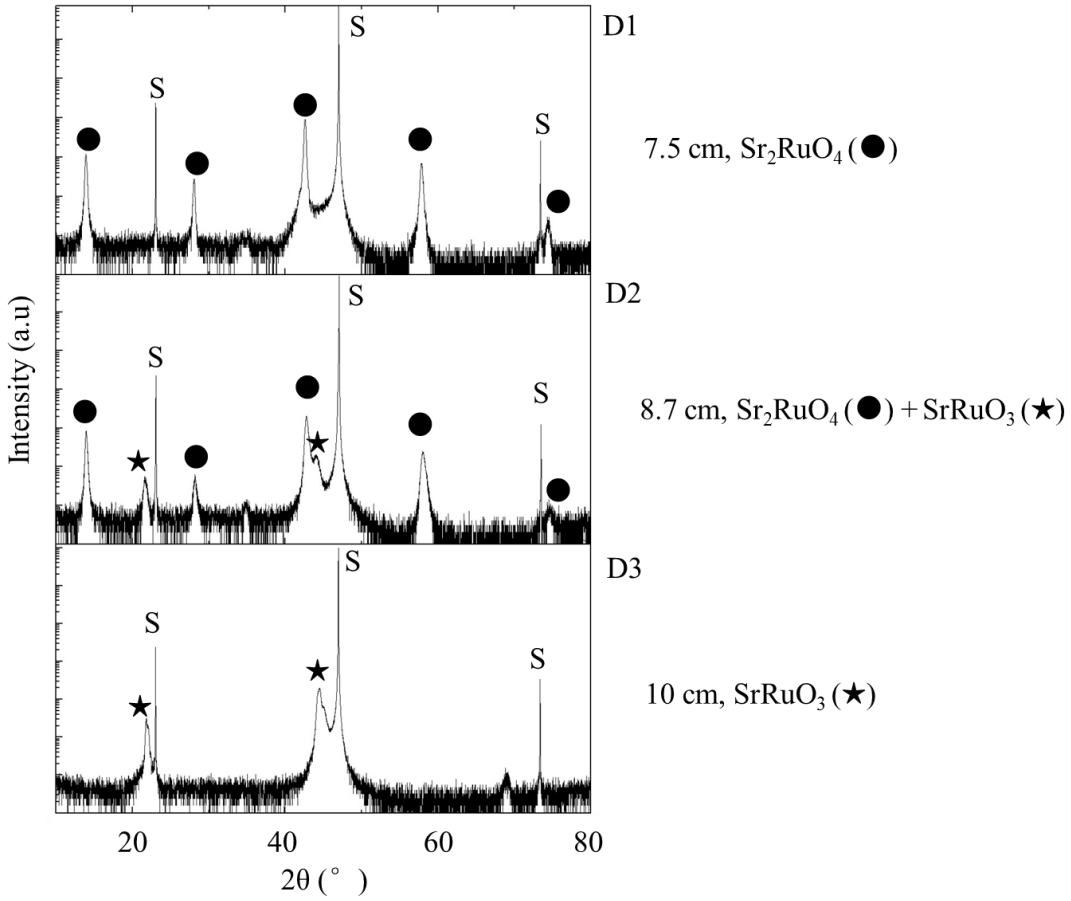

Figure 6.5 XRD results of Sr-Ru-O composition in the film with the change in target to substrate distance (D) presented on a log scale, and the sample names are to the right. During experiments, D was adjusted gradually from short to long, while the oxygen pressure was maintained at 10 mTorr, deposition temperature at 950 °C, and the laser fluence at 1.5 J/cm^2, laser ablation frequency at 8 Hz, and total repetition of 6000 pulses. Heating and cooling rate was maintained at 10 °C/minute. The peaks in the XRD have been identified by comparing to the reference data (JCPDS No. 01-082-1096). S denotes the LSAT substrate. All the peaks for Sr_2RuO_4 identified were (0 0 1) oriented. The film thickness was shown in Table 6.4.

The equation can be understood in the following way. For the deposition of a

specific material in a PLD system, under background gas pressure P_0, there is an optimum target to substrate distance D_0, which guarantees the optimum plume species transfer to substrate. Suppose the background gas pressure P_0 increases to P_0', according to that equation, the new optimum D_0' is shorter compared to D_0. If the real target to substrate distance is still D_0, it means the distance is relatively longer. In this way, increasing the gas pressure or the target to substrate distance has similar effect on the thin film composition. The difference is that the film composition is more sensitive to target to substrate distance because of the power r, which is normally bigger than 1[109]. This empirical law also explains why the oxygen pressure used to grow Sr_2RuO_4 was so different among different research groups, as shown in Table 3.2. Given the different deposition chambers, different target to substrate distances, it is reasonable to have a big variation in the optimum oxygen pressure.

Finally, it has to be noted that the deposition rate is influenced by the target to substrate distance. As D increases, atomic species normally undergo more scattering along the way from target to substrate. Therefore, the deposition rate tends to decrease. Nevertheless, the plasma plume is highly directional, and thus the film thickness in fact does not decrease too much as the distance gets longer[95], as shown in the film thicknesses in Table 6.4.

Sample	Distance (cm)	Thickness (nm)
D1	7.5	58 ± 2
D2	8.7	56 ± 3
D3	10	53 ± 2

Table 6.4 Thickness of the Sr-Ru-O films in Figure 6.5. The thicknesses were estimated from x-ray fringes, the estimation of the thickness and thickness errors from x-ray fringes can be found in Appendix I.

Laser Fluence

The laser fluence influences not only the composition of the ejecting species in the

plume, but also their kinetic energy. In order to achieve stoichiometric Sr_2RuO_4 films, a critical laser fluence range must be determined.

A gradual change in the phase composition with laser fluence is shown in Figure 6.6. With the increase in laser fluence, the dominant phases in the film changed from Sr_2RuO_4 + SrO to Sr_2RuO_4 to Sr_2RuO_4 + $SrRuO_3$ and finally to $SrRuO_3$ at the highest laser fluence. It is clear that in the Sr-Ru-O system, a relatively high laser fluence results in a Ru-rich phase like $SrRuO_3$, while a relative low laser fluence leads to a Sr-rich phase like Sr_2RuO_4.

The reason that high laser fluence results in low Sr/Ru ratio can be related to scattering of the atomic species in the laser plume. In a simplistic view, since the energy from laser fluence (laser energy density) is transferred to the atomic species in the form of their kinetic energy, higher laser fluence results in higher kinetic energy of the atomic species in the plume. Consequently, higher kinetic energy translates to higher linear momentum of the atomic species. Since particles with higher level of linear momentum are less likely to be scattered, increasing laser fluence will normally result in less scattering for the atomic species during the deposition.

In my case, $SrRuO_3$ (low Sr/Ru ratio) tends to be observed at high fluence while Sr_2RuO_4 (high Sr/Ru ratio) tends to be observed at lower fluence. This seems to infer that at high fluence Sr (lighter atom) is more scattered than at low fluence. This somewhat contradicts the arguments in the literature which essentially associate higher fluence to less scattering of lighter atoms. For example, in the case of $YBa_2Cu_3O_{7-x}$ thin films, where Y is lighter than Ba, for low laser fluence below 0.4 J/cm^2, the film was Y-deficient and the Y/Ba ratio was less than 1:2[111].

In view of the above discrepancy, in this Sr-Ru-O film case, the compositional change with respect to fluence cannot be explained by scattering of lighter and heavier atoms alone, but rather there may be combinations of a few mechanisms, which will require an in depth studies on the ionization state of Ru and Sr atoms in the plasma (charged ions scatters differently to neutral atoms), congruent or incongruent target ablation, as well as possible reaction to form bigger molecules in the plasma. In addition,

for different fluence, the spatial distribution of atomic species in the plume may be very different. Moreover, in my case, Ru tends to be oxidized to RuO_4 in the presence of O_2 and therefore further complicates the scattering process.

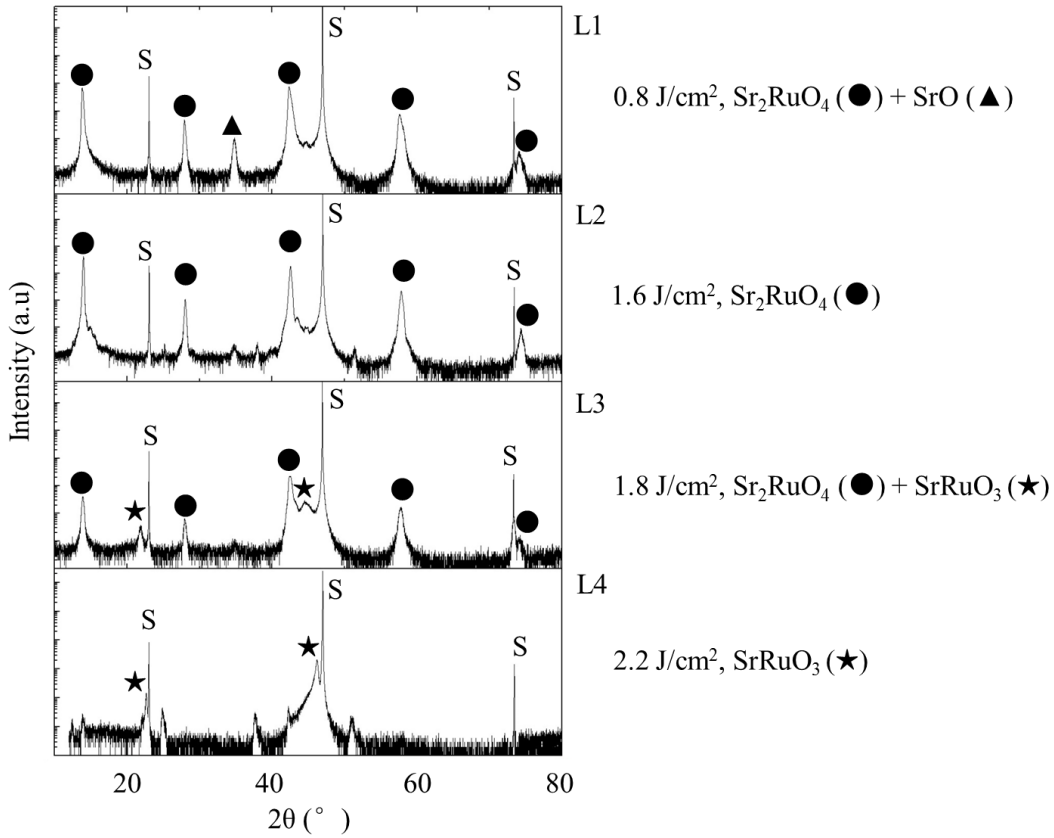

Figure 6.6 XRD results of Sr-Ru-O composition in the film with the change in laser fluence presented on a log scale, and the sample names are to the right. During the optimization, the laser fluence was adjusted gradually while the oxygen partial pressure was set at 10 mTorr, deposition temperature at 950 °C, and the target to substrate distance at 7.5 cm, laser ablation frequency at 8 Hz, and repetition of 6000 pulses. Heating and cooling rate was maintained at 10 °C/minute. The peaks in the XRD have been identified by comparing to the reference data (JCPDS No. 01-082-1096). S denotes the LSAT substrate. All the peaks for Sr_2RuO_4 identified were (0 0 1) oriented. The film thickness was shown in Table 6.5. It has to be noted that there would be a slight energy variation due to the periodic refilling of KrF gas for PLD, which results in higher fluctuation in laser fluence immediately before laser gas refilling.

Finally, it is worth mentioning that a high laser fluence also affects the deposition rate[95]. Generally, a high laser fluence is expected to result in a high deposition rate and thus giving thicker film for the same number of pulses. This is consistent with results shown in Table 6.5. for film deposited using 6000 pulses.

Sample	Fluence (J/cm^2)	Thickness (nm)
L1	0.8	36 ± 3
L2	1.6	60 ± 2
L3	1.8	68 ± 2
L4	2.2	82 ± 3

Table 6.5 Thickness of the Sr-Ru-O films in Figure 6.6. The thicknesses were estimated from x-ray fringes, the estimation of the thickness and thickness errors from x-ray fringes can be found in Appendix I.

Film Composition Using Different Targets

Lastly, films grown using the three different Sr_2RuO_4 targets mentioned previously were compared. The only difference among the three targets was the Sr/Ru ratio. For clarity, the three targets were named as target-1, target-2, and target-3; and the corresponding films were named as A, B, and C, separately. This is shown in Table 6.6.

During the optimization of Sr-Ru-O thin film growth, it has been found that only target-3 gave the possibility of obtaining the intended film peaks (pure Sr_2RuO_4 phase) in XRD scan, as shown in Figure 6.7. Whereas films grown using either target-1 or target-2 always resulted in the extra SrO phase, although possible deposition parameters discussed above have been tried and varied. The result is shown in Figure 6.7, with the red dashed line pointing out the SrO peak. As explained previously, the reason for this is the volatility nature of Ru, resulting in Ru deficiency in both target-1 and target-2 as well as the films. Only target with a 15% excess of Ru (target-3) was found to effectively suppress the appearance of SrO phase and yield the pure Sr_2RuO_4 film. Therefore, target-3 was chosen to be used in the work.

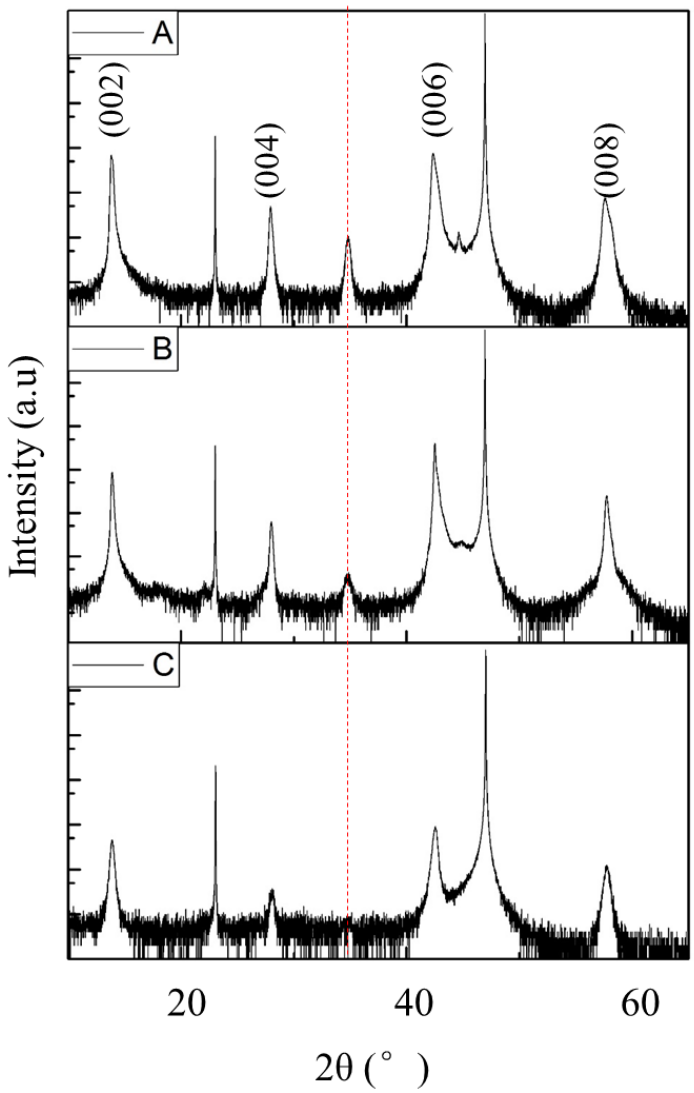

Figure 6.7 XRD results of Sr_2RuO_4 thin films grown using three different targets, presented in log scale. The peaks in the XRD have been identified by comparing to the reference data (JCPDS No. 01-082-1096). All the peaks for Sr_2RuO_4 identified were (0 0 1) oriented. The growth conditions are obtained from the previous optimizations: deposition temperature at 950 °C, oxygen pressure at 7 mTorr, target to substrate distance at 7.5 cm, laser fluence at 1.4 J/cm^2, ablation frequency at 2 Hz and total repetitions of 6000 pulses. Heating and cooling rate was maintained at 10 °C/minute.

Target	Sr/Ru	Corresponding films	Comments on film composition
Target-1	2.1:1	A	Sr_2RuO_4 + SrO phase
Target-2	2:1	B	Sr_2RuO_4 + SrO phase
Target-3	2:1.15	C	Sr_2RuO_4 phase

Table 6.6 Three different targets and the corresponding film phase compositions.

6.1.4 Summary on Sr_2RuO_4 Thin Film Phase Optimization

To sum up, the deposition of c-axis oriented Sr_2RuO_4 thin films on LSAT substrate using my hand-made target has been optimized by studying the influence of four major deposition parameters on film compositions. Firstly, targets were fabricated using different nominal Sr/Ru ratios and the resulting films were examined. The target fabricated with a slight excess Ru powder was found to give the most phase pure films. Subsequently, oxygen pressure, deposition temperature, target to substrate distance, and the laser fluence were tuned systematically to find the deposition trend. Changes in the dominant phase in as-deposited Sr-Ru-O films have been revealed to follow some trends. In general, the appearance of Sr_2RuO_4 phase prefers low oxygen pressure, high deposition temperature, short target to substrate distance and low laser fluence. To summarize, a schematic phase diagram has been illustrated in Figure 6.8.

Although the deposition parameters were adjusted independently, they are actually interrelated as already discussed in the previous sections and all have an influence on the deposition rate. It has been discussed in Chapter 4 that the deposition rate can affect thin film formation mechanism. This, in effect, also means that the deposition rate will eventually affect surface morphology/roughness.

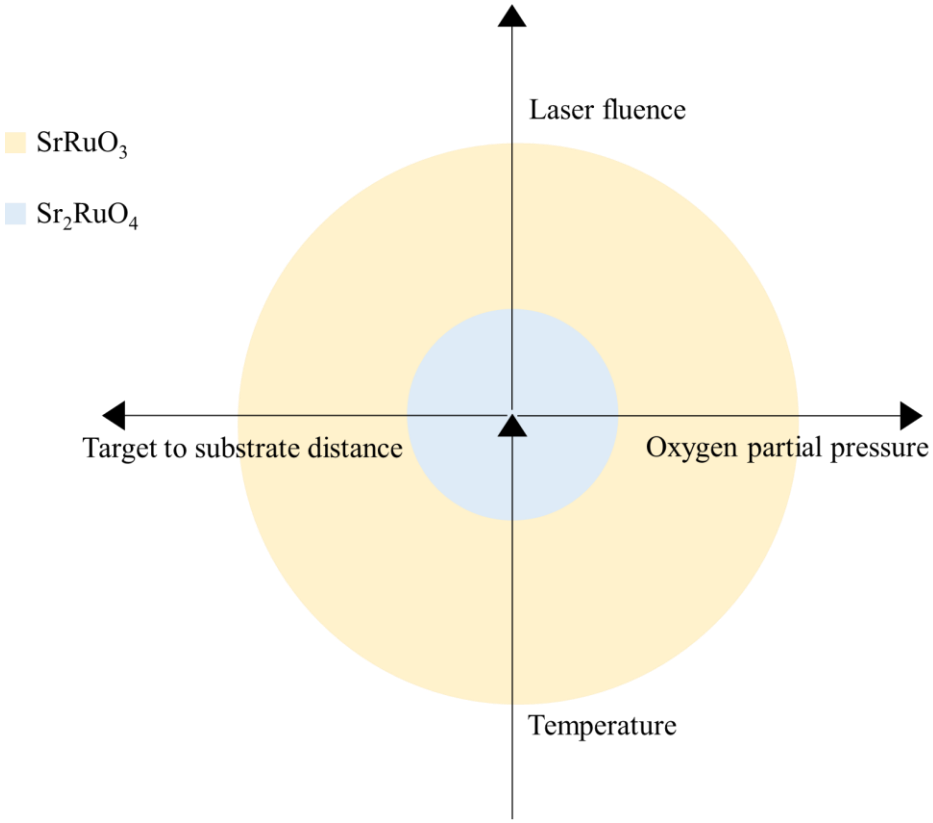

Figure 6.8 A short summary of the phase diagram on the four deposition parameters: oxygen pressure, deposition temperature, target to substrate distance, and laser fluence. The arrow indicates an ascending direction for the specific axis.

6.1.5 A Comment on the Reproducibility of Sr_2RuO_4 Phase

In general, PLD is a very reliable technique for thin film growth under optimized conditions. In my case, apart from finding the trends of the growth conditions of Sr-Ru-O thin films, it has also been found that Sr_2RuO_4 films with reasonably consistent XRD peaks can be consistently grown. For example, the XRD results of the four samples (P3, T2, D1, L2) which were grown under nearly identical conditions have been summarized in Figure 6.9. The XRD patterns for all four samples show c-axis oriented Sr_2RuO_4 phase.

Nonetheless, there are some slight variations. First, it seems that there are some tiny extra peaks for sample L2. In the case of L2, it was grown when the KrF gas for the laser was nearly empty, right before the KrF gas refill. Thus the laser beam was not very stable and there was a slightly higher fluctuation on the laser fluence compared to

normal situation. Therefore, the XRD result of L2 deviates a little bit from the other three. Second, the reason that there are slight variations in the XRD of the four samples may be due to inhomogeneity in the target. Due to the fact that the Sr_2RuO_4 target used in this work was hand-made, it was really hard to guarantee perfectly homogeneous target compositions. Therefore, slight compositional variation may occur between every deposition. This issue may be overcome by using a high quality commercial Sr_2RuO_4 target which unfortunately was not widely available due to limited studies on this material.

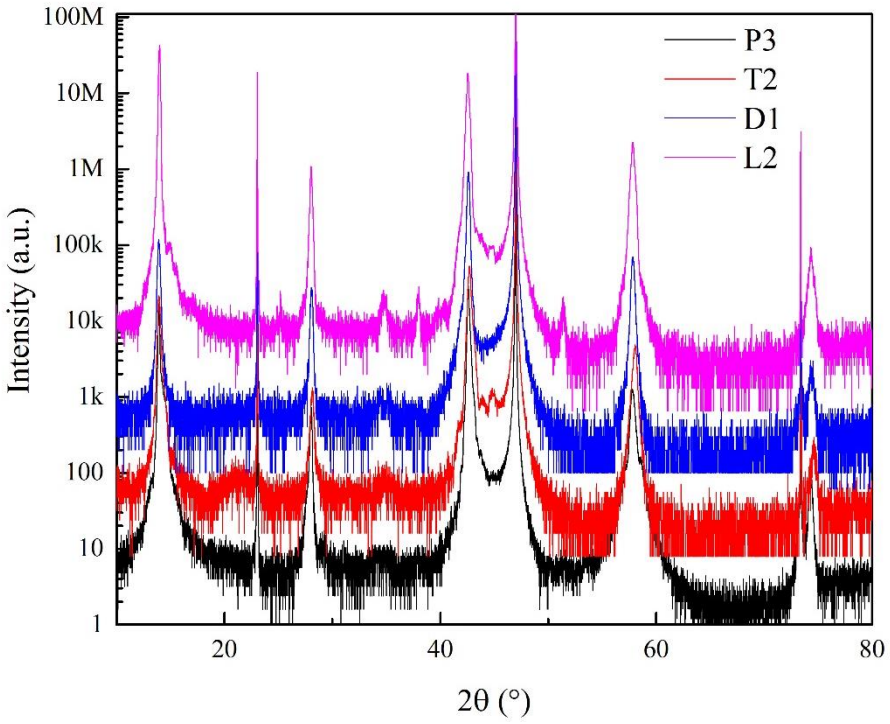

Figure 6.9 XRD results of four Sr_2RuO_4 thin films using nearly identical growth conditions, presented in log scale. All four samples were grown at deposition temperature of 950 °C, oxygen pressure of 10 mTorr, target to substrate distance of 7.5 cm, laser fluence of 1.5 J/cm^2 (for P3, T2, D1) - 1.6 J/cm^2 (for L2), and ablation frequency of 8 Hz.

In addition, the film thicknesses and surface roughnesses of the four samples (P3, T2, D1, L2) are summarized in Table 6.7. As expected, all the four films have similar thickness and surface roughness values. This, once again, demonstrates that the quality of the Sr_2RuO_4 thin films grown in my experiments are reproducible.

sample	P3	T2	D1	L2
Thickness (nm)	57 ± 3	55 ± 4	58 ± 2	60 ± 2
Roughness (nm)	3.892	3.695	3.978	4.101

Table 6.7 Thicknesses and root mean square (RMS) surface roughness values of the four Sr_2RuO_4 thin films using nearly identical growth conditions: P3, T2, D1, L2. The estimation of the film thickness was from x-ray fringes, and more information can be found in Appendix I about the estimation and calculation of thickness errors.

6.2 Transport Study and Improvements to the Fully Metallic Sr_2RuO_4 Thin Films

After being able to grow c-axis oriented Sr_2RuO_4 films with the right phase, the next objective was to focus on characterizing transport properties. Unfortunately, all the early Sr_2RuO_4 thin films had metal-insulating transitions (MIT). Their resistance values first decreased as the sample was cooled down, showing metallic behavior; then at low temperatures the resistance increased as the sample was further cooled down, leaving a metal-insulating transition in the plot. An example of the resistance as a function of temperature plot is shown in Figure 6.10.

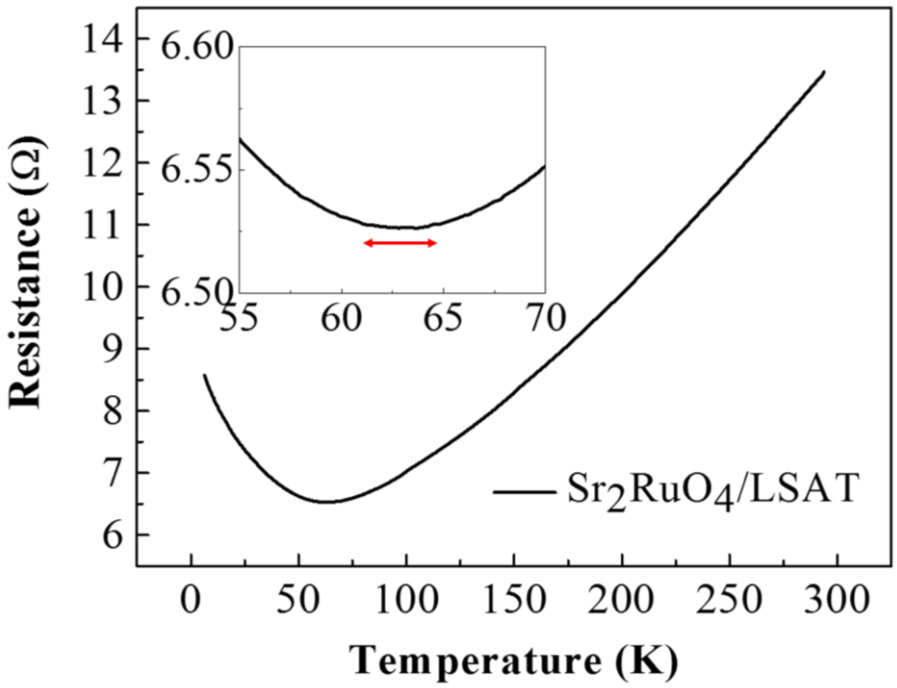

Figure 6.10 Resistance as a function of temperature for a typical metal-insulating Sr_2RuO_4/LSAT sample. The deposition was done at temperature of 920 °C, oxygen pressure of 10 mTorr, target to substrate distance of 7.5 cm, laser fluence of 1.6 J/cm^2, ablation frequency of 8 Hz and total repetition of 10000 pulses.

The metal-insulating transition is normally not a sharp one, but undergoes a broad temperature range, as shown in the red arrow in the inset in Figure 6.10. The MIT temperature is defined as the temperature where the resistance is the minimum, and the

transition width is defined as the temperature range of the two points where the resistances difference are within 0.01 times of the value the minimum resistance, which also defined the error bars for the MIT temperatures in the following sections.

This MIT has never been reported in single crystals Sr_2RuO_4 before, but has been seen in many Sr_2RuO_4 thin films[17, 18, 47, 77, 78]. In spite of this, the reason and mechanism behind the MIT in Sr_2RuO_4 is still not clear to date. It has only been suggested that the disorder within the Sr_2RuO_4 films may play a role[17]. As described in Chapter 3, it has already been understood how growth conditions in the floating zone method can affect the quality of superconducting single crystals of Sr_2RuO_4. Therefore, defects can be minimized in this process explaining why it is easier to obtain superconducting single crystal Sr_2RuO_4. For thin film growth techniques like PLD, many factors during growth process can result in disorder. For example, a dirty or faulty substrate can affect the nucleation process, target with lower purity can result in unwanted elements in the film, the chemical composition of the film may be off the desired stoichiometry, compromising the structural perfection, the growth temperature can influence the film crystallinity. At present, there are not enough studies on Sr_2RuO_4 thin film growth and this in turn limited our understanding of how to improve the transport properties.

6.2.1 Correlation between the FWHM and MIT Temperatures of Sr_2RuO_4 Thin Films

To understand the underlying reason for the occurrence of a MIT, a few metal-insulating Sr_2RuO_4 thin films with different MIT temperatures were investigated. Although their θ-2θ XRD showed that the Sr_2RuO_4 phase was dominant, the difference in film crystalline quality was observed by comparing the rocking curves (ω *scan)* of the (0 0 6) Sr_2RuO_4 phase. The full-width at half-maximum (FWHM) of rocking curves were observed to vary from sample to sample. The reason for comparing rocking curves is because it represents the overall structural quality of the film. Defects such as dislocation, mosaicity, disorientation or inhomogeneity[126, 127] all increase FWHM of the rocking curve. The fact that different FWHM of different rocking curves was

observed suggests that among the different metal-insulating Sr_2RuO_4 thin films, there was a variation in crystalline quality. In Figure 6.11, the MIT temperatures of these Sr_2RuO_4 thin films samples are plotted against the FWHM values of the (0 0 6) rocking curves. The samples were grown using a broad range of deposition parameters with fluence ranging from 0.9 J/cm^2 to 1.6 J/cm^2, temperature from 900 °C to 950 °C, target to substrate distance at 7.5 cm, oxygen pressure from 0.4 mTorr to 15 mTorr and ablation frequency of 8 Hz. These films were grown using different total number of pulses ranges from 8000 pulses to 15000 pulses, to account for the various deposition rate when using different deposition parameters. The MIT error bars in the y-direction has been explained earlier and shown in the red arrow in the inset in Figure 6.10. Note that no error bars was shown in the x-direction (FWHM). This is because all the samples were measured using the same instrument, and the major source of error is the instrumental broadening which is about 0.02° according to the instrument manual. The instrumental broadening in the FWHM shown in the graph has already been subtracted.

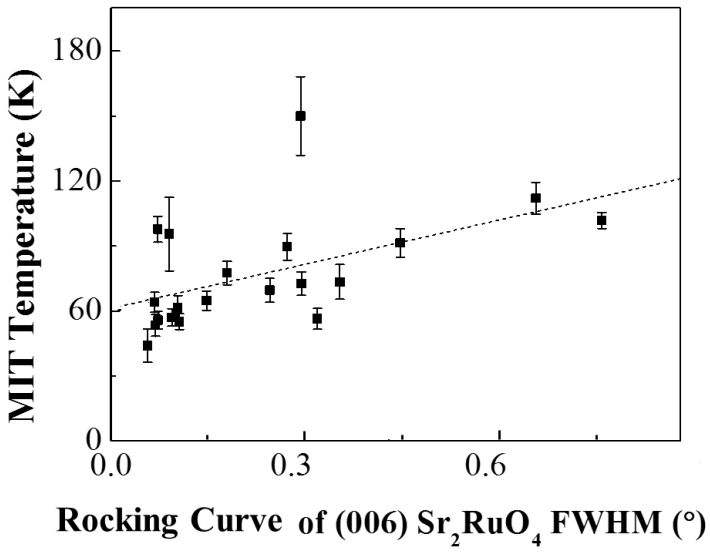

Figure 6.11 MIT temperature as a function of the FWHM of (0 0 6) Sr_2RuO_4 rocking curves for the metal-insulating Sr_2RuO_4 films. The dashed line is a linear fitting of all the data points shown, marking a trend of the MIT temperature dependency on the rocking curves.

From the distribution of the data points, a trend can be observed showing that the MIT temperature tends to be lower in Sr_2RuO_4 films with a smaller FWHM. This indicates that sample with lower FWHM (better structural quality) tends to have lower MIT temperature, which is not surprising because it was well studied in single crystal Sr_2RuO_4 that any structural imperfections may be detrimental to its transport properties.

6.2.2 Fine Tuning to Improve Transport of Sr_2RuO_4 Thin Films

From the above discussions, it is clear that the electrical transport quality of the initial Sr_2RuO_4 films was far from satisfactory. In order to suppress the MIT in the Sr_2RuO_4 thin films, the crystalline quality of the sample had to be improved. Therefore, experiments were carried out as how to improve the sample quality. Although in the previous section, four major deposition parameters have been coarsely optimized, resulting in the right Sr_2RuO_4 majority phase in the XRD, the eligible parameter ranges were still wide. Due to the nature of the plume generation in deposition, variations in deposition parameters could result in either inhomogeneity or off-stoichiometric composition of films. In the case of Sr_2RuO_4, these could lead to defects and mis-orientations and hence have a significant impact on the transport properties[128]. Therefore, fine tuning of the deposition parameters was necessary.

For fine tuning, oxygen pressure, laser fluence, deposition temperature, and ablation frequency were considered. The target to substrate distance was excluded mainly because it is not flexible to be adjusted in small scale during fine tuning. In the same way as before, only one deposition parameter was changed and the rest remained the same. The film thickness was controlled at about 100 ± 10 nm during fine tuning of all deposition parameters except ablation frequency. When using low ablation frequency (e.g. 1 Hz), it is experimentally impractical to grow 100 nm thick films as it would take at least 10000 pulses for optimized parameter growth rate which translates to about 3 hours deposition. Since the substrate heater was operating at near its maximum capability (e.g. 1000 °C), the best practice was to keep deposition duration to of 1 – 1.5 hours.

Oxygen Pressure

The Sr_2RuO_4 phase was found to appear in a range of oxygen pressures during the previous phase optimization, therefore, during the fine tuning, the oxygen pressure was adjusted from 0.4 mTorr to 15 mTorr, where Sr_2RuO_4 was most likely observed. After deposition, the FWHM of the (0 0 6) Sr_2RuO_4 rocking curves and the MIT temperatures were both measured. The results were plotted against the changes in oxygen pressure. In Figure 6.12, by slowly increasing the oxygen pressure, the FWHM of Sr_2RuO_4 first decreased to about 0.1°, then increased slightly to about 0.2°. MIT temperature of Sr_2RuO_4 films first decreases as the oxygen pressure increases. This observed behavior can be analyzed by taking into account that more oxygen during deposition is more favorable for formation of the Sr_2RuO_4 phase in the film, and vice versa. This is consistent with the trend discussed in the previous section. Additionally, Ru is important in constituting the RuO_2 plane, which is vital for the conductivity of Sr_2RuO_4.

Further increasing oxygen pressure leads to an increase in MIT temperature again. This may be associated with excess O_2, which would also cause a tendency for $SrRuO_3$ to form, as explained in the reaction equation 6.2 in the previous section, resulting in both inhomogeneity and off-stoichiometry in the film. Although a small amount of either inhomogeneity or off-stoichiometry could be hardly detected by XRD, this would inevitably distort the Sr_2RuO_4 microstructures. Consequently, this would not only result in the rocking curve FWHM broadening, but more importantly, results in poor electrical transport. This explains why the MIT temperature and the FWHM increased when the oxygen pressure is further increased.

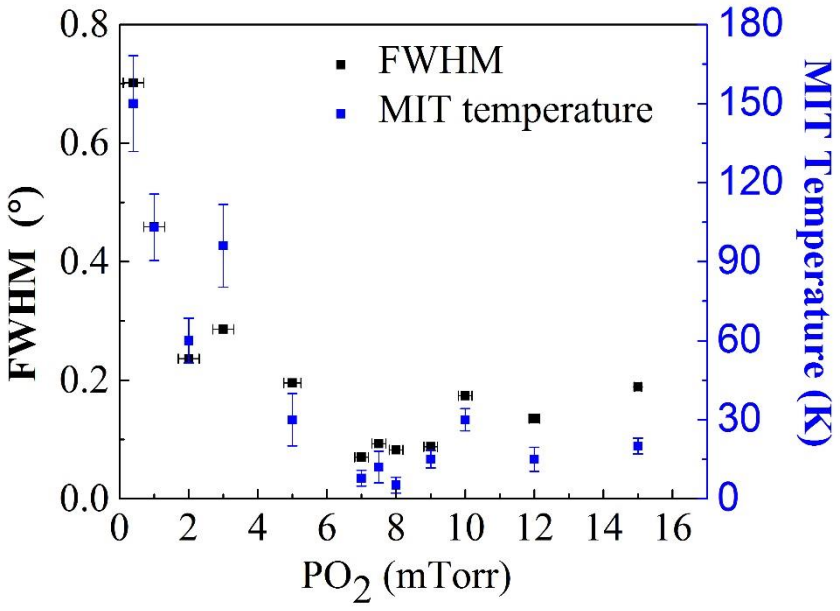

Figure 6.12 The FWHM of (0 0 6) Sr_2RuO_4 rocking curves and MIT temperatures for the metal-insulating Sr_2RuO_4 films as a function of the change in oxygen pressure. The oxygen pressure was fluctuating in a small range. This was observed as the fluctuation in the pressure meter, which is recorded as error bars. The deposition was carried out at temperature of 910 °C, laser fluence at 1.4 J/cm^2, and ablation frequency at 2 Hz, 10000 pulses. It should be noted that the temperature used in this oxygen pressure trials was only 910 °C. During those depositions the original heater was down and there was a shortage of wiring supply, and therefore the heater was only replaced with a thinner wire which can only withstand current to produce maximum temperature of 930 °C.

Laser Fluence

Similar to oxygen pressure, laser fluence was fine tuned to obtain good electrical transport properties. The FWHM of the (0 0 6) Sr_2RuO_4 rocking curves and the MIT temperatures were plotted against changes in laser fluence in Figure 6.13. Similar to the analysis in previous section, high laser fluence would favor $SrRuO_3$ (low Sr/Ru ratio) phase, while low laser fluence would favor Sr_2RuO_4 (high Sr/Ru ratio) phase. The deviation from an optimum laser fluence could lead to either Ru surplus or Sr surplus, and hence could have detrimental effect on electrical transport properties. In Figure

6.13, the FWHM of the rocking curves decreases with the increase in laser fluence. Similarly, the MIT temperature also decreases as the laser fluence increases and flatten out in the range between 1.3 J/cm^2 and 1.6 J/cm^2 where the MIT does not change much.

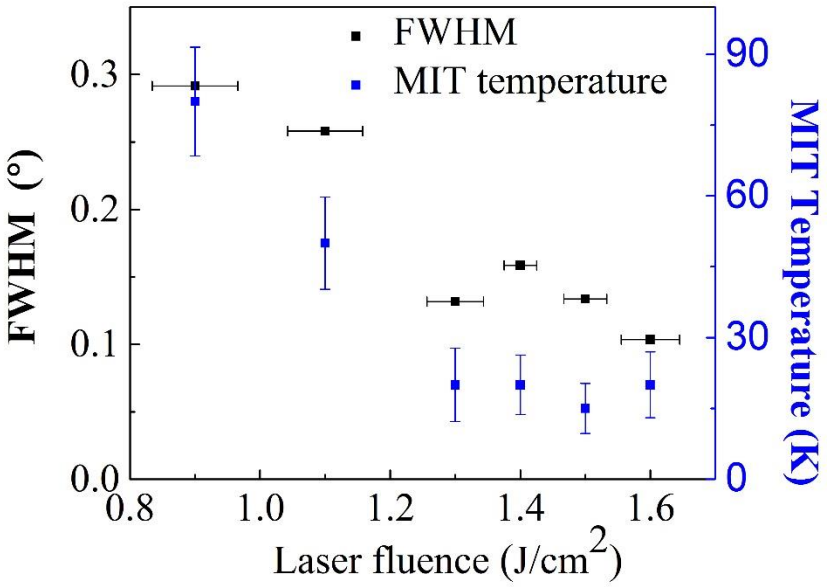

Figure 6.13 The FWHM of (0 0 6) Sr_2RuO_4 rocking curves and MIT temperatures for the metal-insulating Sr_2RuO_4 films as a function of the change in laser fluence. The laser energy was within some fluctuations. This fluctuation was observed from the laser control panel, and was taken into account in the error bars. The other growth conditions here are: deposition temperature 910 °C, oxygen pressure 10 mTorr, ablation frequency 2 Hz, and repetition 10000-18000 pulses. The heater was still using the thin wire, and thus temperature of only 910 °C was used.

Deposition Temperature

The deposition temperature range in the fine tuning was set from 900 °C to 960 °C. Similar to the previous parameters, the FWHM as a function of deposition temperature were shown in Figure 6.14. It has to be noted that two points were plotted at 910 °C. This is because during the deposition of sample 1, the target rotation motor encountered some problems and the Sr_2RuO_4 target stopped rotating. In order to maintain consistency and comparability with other samples, sample 2 was grown using the exact

same composition after the rotation motor was fixed.

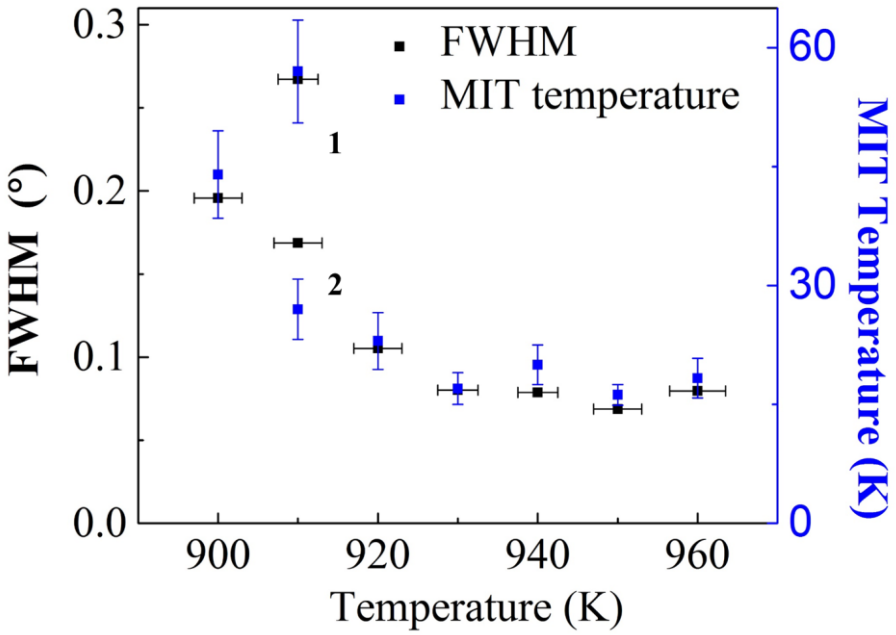

Figure 6.14 FWHM of (0 0 6) Sr_2RuO_4 rocking curves and the MIT temperatures for the metal-insulating Sr_2RuO_4 films as a function of the change in deposition temperature. As long as the silver paint used to stick the substrates on the heater surface was spread homogeneously throughout the back of the substrate, the temperature was homogeneous on the substrate surface. The temperature reading was from the pyrometer reading on the substrate before and after the deposition, which were the same. This was also compared with the reading from the thermometer coupled with the heater. The deviation observed between the pyrometer and the thermometer was recorded as the error bars in this work. Films were grown at oxygen pressure 10 mTorr, laser fluence of 1.4 J/cm^2, ablation frequency of 2 Hz, and repetition of 10000 pulses.

According to the study of Krockenberger[14], the growth window for a high quality Sr_2RuO_4 film is less than 10 °C. Therefore the temperature separation (step) in the fine tuning was set as 10 °C to capture the perfect window of growth. As can be seen in the experiments, with the increase in deposition temperatures, the FWHM of rocking curve gets smaller. The FWHM saturates from the range of 930 °C to 960 °C, and this is higher than the optimized deposition temperature of Krockenberger's superconducting

Sr_2RuO_4 film, which is 920 °C[14]. A high temperature not only guarantees enough activation energy for thin film nucleation, but also facilitates a layer-by-layer thin film growth[96]. In this sense, the number of defects and mis-orientation may be reduced, and hence the sample quality can be improved at higher growth temperature. Not surprisingly, the MIT temperature of Sr_2RuO_4 films also decreased with the increase in deposition temperature.

Ablation Frequency

Ablation frequency turns out to be important during the fine tuning of deposition parameters. An optimum ablation frequency between 2 to 4 Hz was observed to yield the minimum FWHM value, as shown in Figure 6.15. For ablation frequency higher than 4 Hz, the observed FWHM values are relatively higher than films grown at low frequency. This is because the elapsed time between each deposition pulse might have been too short for adatoms to undergo surface diffusion and form layer by layer growth. This is similar to the argument in kinetic factor in Chapter 4.1. Therefore, the surface roughness could be too high for the subsequent arriving atoms. This is shown in the AFM image in Figure 6.16(a), where big clusters can be seen on top of the sample surface. After many layers of deposition, it is highly likely to induce the generation of defects or inhomogeneities. This is one of the major reasons for rocking curve broadening at high ablation frequency, resulting in the high FWHM values in Figure 6.15. In this regard, a Sr_2RuO_4 film with high density of defects would be very likely to have high MIT temperatures, as shown in the blue data in Figure 6.15. As the ablation frequency was reduced to 2 Hz, the surface of the sample was smoother and no big clusters were observed, as shown in Figure 6.16(b). In addition, the FWHM of the rocking curve was also smaller as shown in Figure 6.15, indicating a better sample quality. However, as the ablation frequency was further reduced to the minimum achievable in the system, 1 Hz, the MIT transition temperature was observed to increase again. Figure 6.16(c) revealed the surface profile of this sample, which shows slightly higher roughness compared to the film grown at 2 Hz. This also corresponds to a higher

FWHM of the rocking curve in Figure 6.15. The reason for this is not exactly clear considering low frequency should promote smoother growth. However, taking into consideration of the fact that Ru is volatile in high temperature and oxygen atmosphere, part of Ru atoms on the substrate might have been evaporated during the time lapse between two pulses and can slightly affect the film stoichiometry, which may have generated defects and affect the surface roughness.

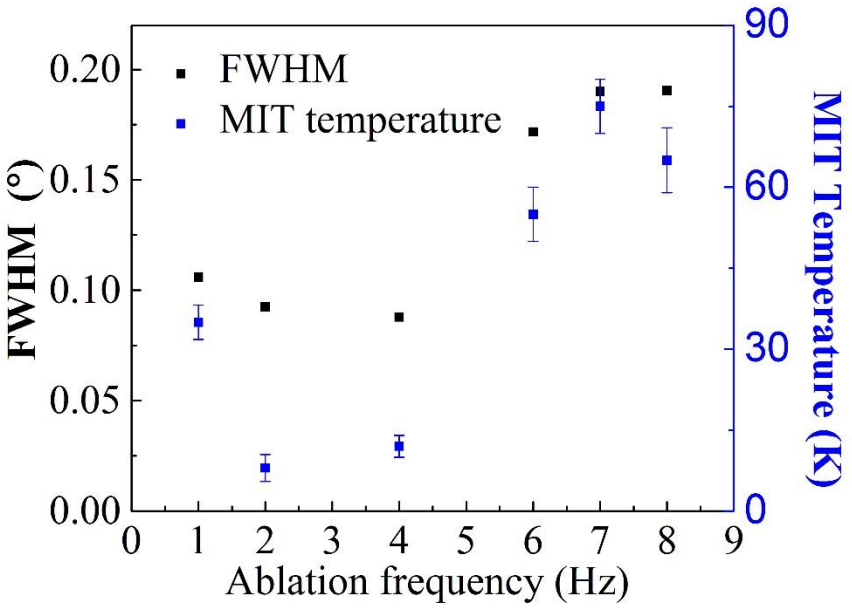

Figure 6.15 The FWHM of (0 0 6) Sr_2RuO_4 rocking curves and the MIT temperatures for the metal-insulating Sr_2RuO_4 films as a function of the change in ablation frequency. The ablation frequency was set by the laser control panel and is an integer. Therefore, no error bar was used for the laser frequency. The rest of the growth parameters are: deposition temperature 950 °C, oxygen pressure 7.5 mTorr, laser fluence 1.3 J/cm^2, and ablation repetition of 5000 pulses to give the film thickness of about ~50 nm.

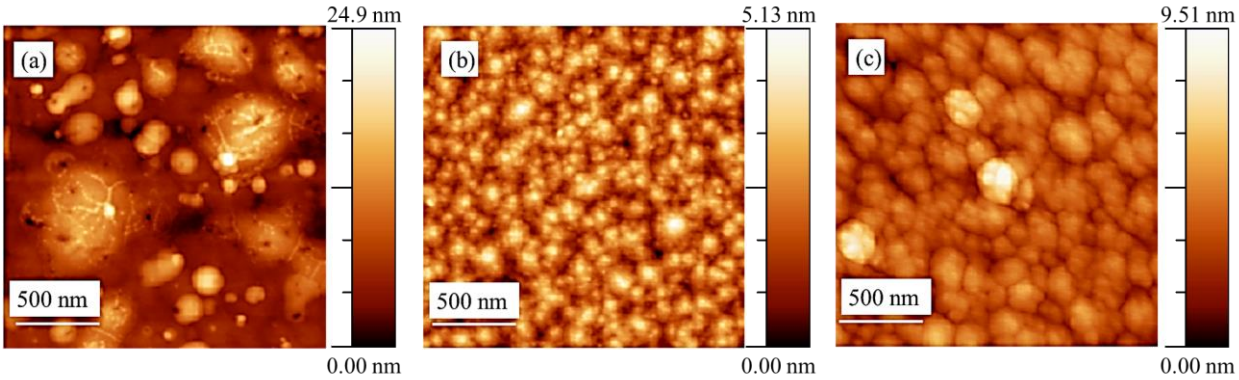

Figure 6.16 AFM images for three Sr_2RuO_4 thin films grown at different ablation frequency: (a) 8 Hz, the RMS surface roughness is about 3.719 nm, (b) 2 Hz, the RMS surface roughness is about 0.7 nm, and (c) 1 Hz, the RMS surface roughness is about 1.129 nm.

Substrate Annealing

In addition to the four parameters, another direct way to improve sample quality is substrate surface treatment. As discussed in Chapter 4, thin films grown on substrates with step-terraces or single terminations have high quality. It is known that smooth step-terraces can be created by annealing the substrates[129]. However, as LSAT is a complex material, which is consisted of La, Sr, Al, Ta, and O, it is difficult to achieve single terminations. Most annealing process have resulted in many SrO islands on the LSAT surface due to the volatility of La[130], this is shown in Figure 6.17(a). In the annealing trials in this work, the LSAT substrate was annealed in oxygen in order to make the annealing environment similar to the deposition environment. The island structure reported in the literature also happened and the result is shown in Figure 6.17(b). The island may act more like a hindrance rather than help with achieving high quality thin films. Therefore, to avoid too much complexity, LSAT substrates in my depositions were only carefully cleaned before deposition, without any other treatment.

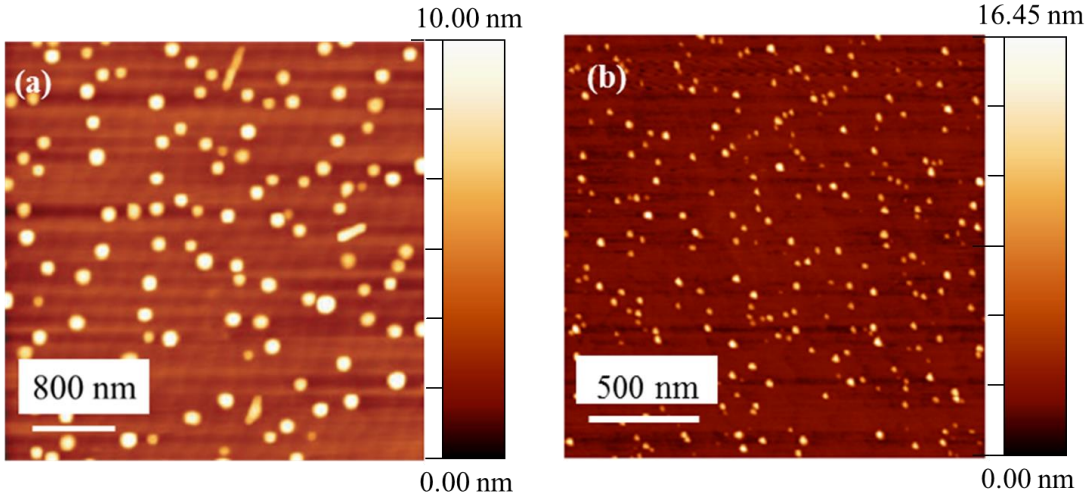

Figure 6.17 The AFM image of (a) Blank LSAT substrate annealed at 1100 °C for 30 min in air showing SrO islands from reference[130]. (b) Blank LSAT substrate after annealing in oxygen flow for 6 hours at 1000 °C.

6.2.3 Summary on The Transport Improvement of Sr_2RuO_4 Thin Films

After the fine tuning of the above four deposition parameters, all the FWHM values of (0 0 6) Sr_2RuO_4 rocking curves and their MIT temperatures have been plotted in Figure 6.18. A correlation between the two can be observed, which is consistent with the trend in Figure 6.11. High value of FWHM almost certainly results in high MIT temperature in Sr_2RuO_4 thin films. As the rocking curves get sharpened, the MIT temperatures are suppressed to lower values. This trend has not only highlighted the importance of high quality Sr_2RuO_4 films (low FWHM) to its transport [17, 60], but also pointed out an easy and straightforward way to improve the transport behavior through rocking curve FWHM analysis.

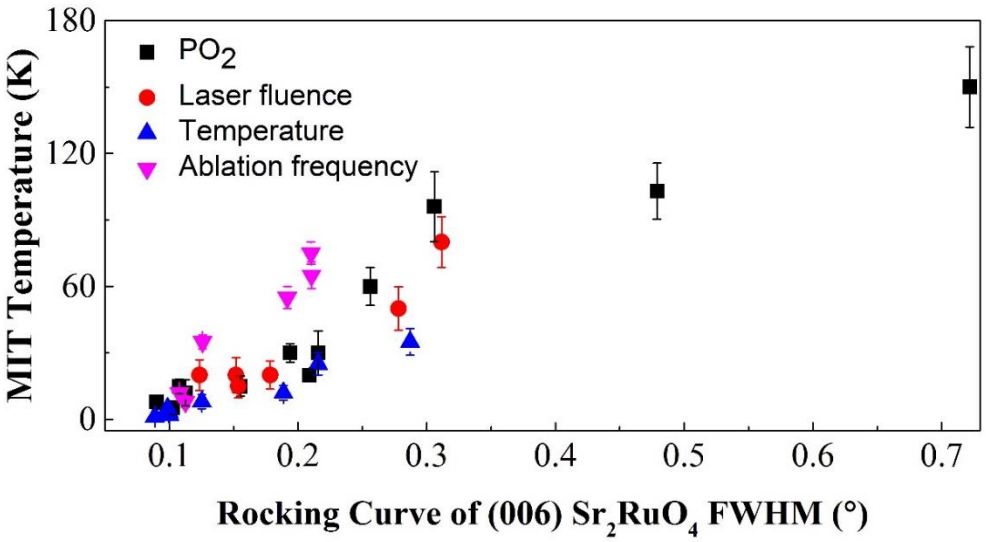

Figure 6.18 A summary of the link between MIT temperatures and the FWHM of the (0 0 6) Sr_2RuO_4 rocking curves based on the fine tuning of the four parameters: oxygen partial pressure, laser fluence, deposition temperature, and ablation frequency.

After the fine tuning of the four parameters, metallic c-axis oriented Sr_2RuO_4 films with very good epitaxy have been achieved, this is shown in Figure 6.19. The optimized deposition parameters for metallic Sr_2RuO_4 thin films are: deposition temperature

950 °C, oxygen pressure: 7 – 9 mTorr, target to substrate distance 7.5 cm, laser fluence 1.3 – 1.6 J/cm^2, and ablation frequency: 2 – 4 Hz. By using these optimized conditions, metallic film can be reproducibly obtained.

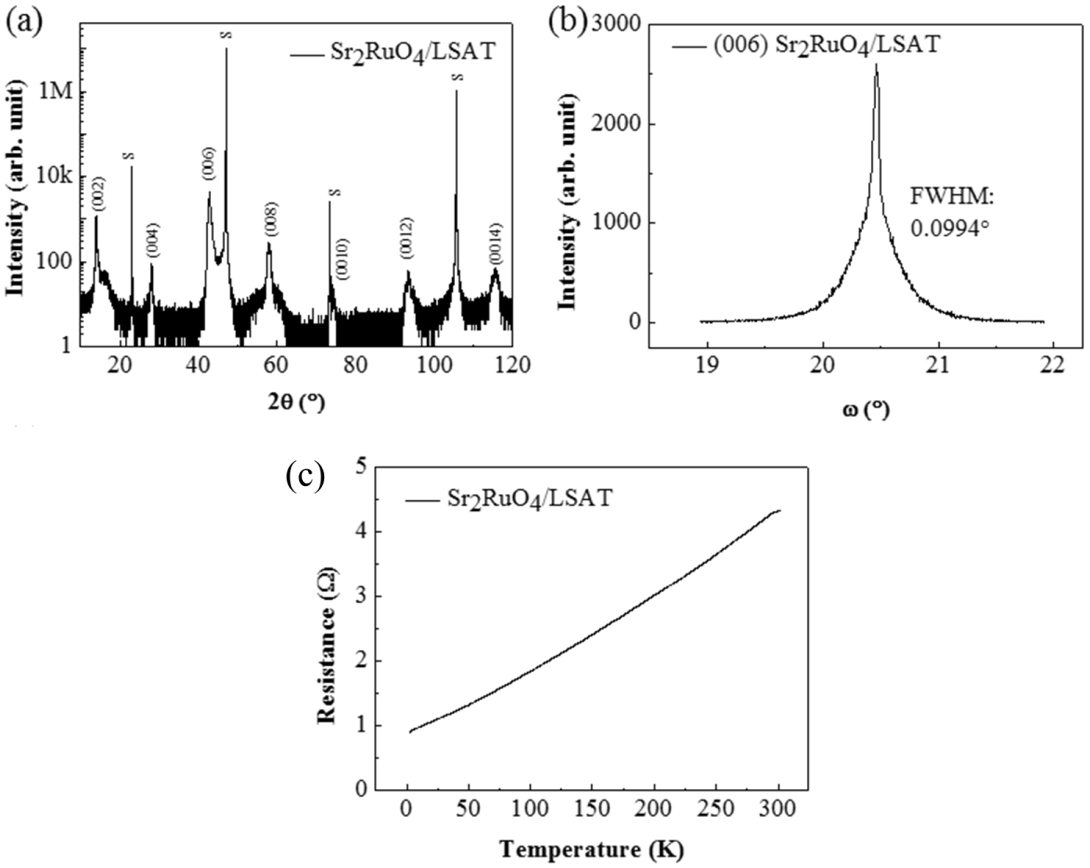

Figure 6.19 Optimized results for metallic Sr_2RuO_4/LSAT thin film. The growth condition for this sample is: deposition temperature 950 °C, oxygen pressure 7.5 mTorr, target to substrate distance 7.5 cm, laser fluence 1.3 J/cm^2, ablation frequency 2 Hz. (a) *θ-2θ* scan; (b) rocking curve of (0 0 6) Sr_2RuO_4; (c) *in-plane* resistance as a function of temperature.

6.2.4 Comment on the AFM Results of the Sr_2RuO_4 Thin Films

In general, it is difficult to draw a direct conclusion between the surface roughness and the transport properties. It cannot be said that film with a smooth surface would definitely have good (metallic) electrical transport behavior. However, it is clear that the metallic films have smooth surfaces, as compared to the MIT films. This is shown in Figure 6.20, where Figure 6.20(a) and (b) are metal-insulating films, and Figure 6.20(c) and (d) are metallic films.

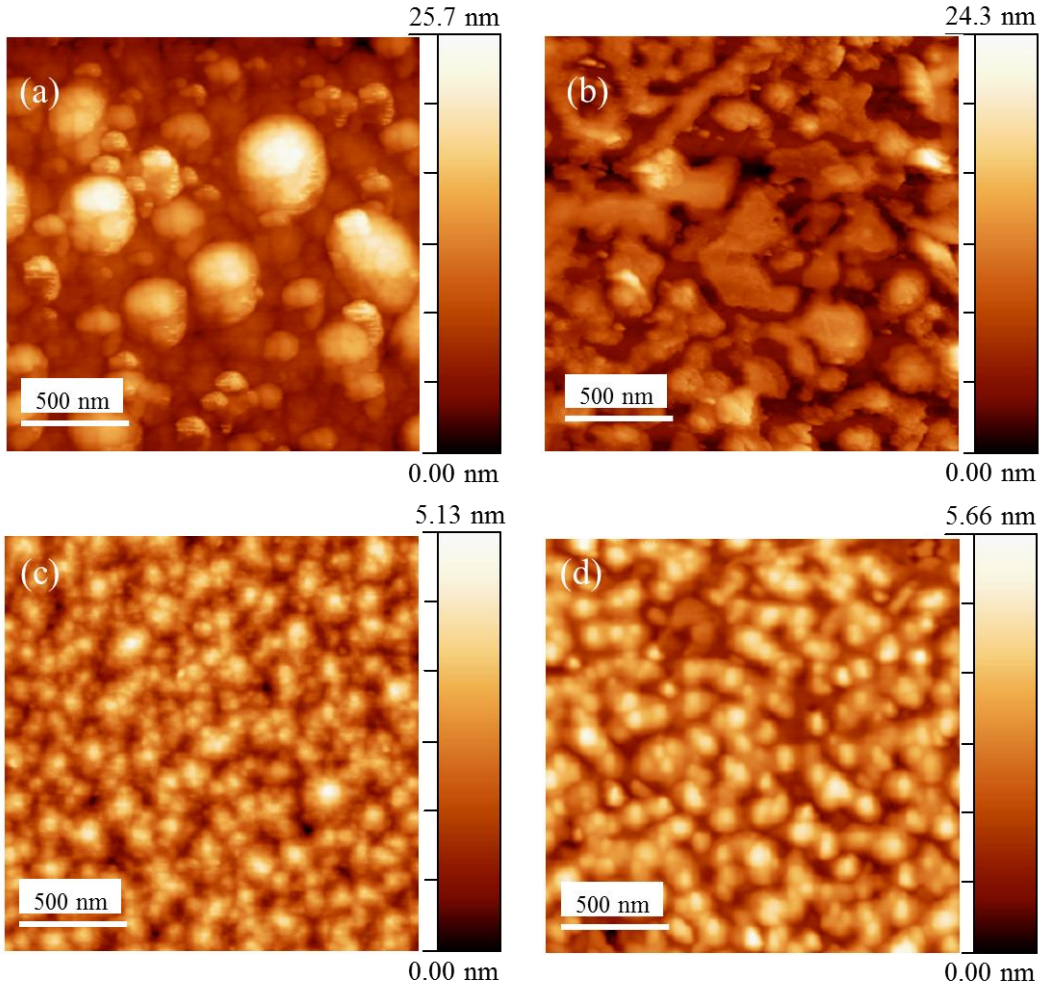

Figure 6.20 AFM topography image for four Sr_2RuO_4 thin films. (a) and (b) metal-insulating samples (c) and (d) metallic samples.

The growth conditions and other details have been summarized in Table 6.8. The AFM topography image of the two MIT thin films demonstrate very rough surface with

big clusters or islands. As discussed previously, this is detrimental to the transport properties of Sr_2RuO_4. In comparison, sample (c) and (d) are both metallic Sr_2RuO_4 thin films. The surface of the two samples are very smooth under the AFM, as shown in Figure 6.20 (c) and (d). The growth conditions for the two samples are quite similar and this demonstrates the reproducibility of the metallic thin film growth conditions obtained after the fine tuning.

Sample	a	b	c	d
Deposition Temperature (°C)	920	920	950	950
Oxygen pressure (mTorr)	10	10	7.5	8
Target to substrate distance (cm)	7.5	7.5	7.5	7.5
Laser fluence (J/cm^2)	0.9	1.6	1.3	1.4
Ablation frequency (Hz)	8	8	2	2
Thickness (nm)	40	46	50	53
RMS Roughness (nm)	4.1	3.97	0.7	0.83
MIT temperature (K)	90	62	metallic	metallic

Table 6.8 Details of the four Sr_2RuO_4 thin films shown in Figure 6.20.

It is worth noting that not many samples were characterized using AFM because the sample surface tends to get damaged/dirty if other characterization (wire bonding or XRD) was performed on the sample before AFM. As the goal of this work is to get good transport properties of the Sr_2RuO_4 thin films, transport measurement and XRD characterization were always prioritized. In addition, for sputtering systems, more than one substrate can be loaded in the chamber under optimized conditions. In contrast, in the PLD "106" system which I was using, the plume was concentrated and sharp, which means only one sample can be grown at one deposition. Therefore, not enough samples were characterized under AFM. The purpose of doing the comparison between metallic and MIT films in Figure 6.20 is to show that the surface of metallic film is smooth compared to MIT film. Nevertheless, this alone cannot form a firm correlation between surface roughness and electrical transport properties.

In summary, by fine tuning of the four different parameters, the metal-insulating transitions have been suppressed and metallic film can be reproducibly obtained. The ultimate challenge was to make another improvement from metallic Sr_2RuO_4 films to fully superconducting ones. Given the myriad of failures in current literature, it is an extremely challenging task.

In the next chapter, the focus is on reporting the analysis of the localized superconductivity in Sr_2RuO_4 thin films grown on LSAT substrate.

Chapter 7 Enhanced Localized Superconductivity of Sr_2RuO_4 Thin Film on LSAT

In the previous chapter, we reported the optimization of the phase and transport properties of c-axis oriented Sr_2RuO_4 thin films on LSAT substrates. The electrical properties have been improved from metal-insulating to fully metallic through fine-tuning deposition conditions. Although superconducting Sr_2RuO_4 thin films were also obtained, no definite parameters could be found to consistently achieve superconducting Sr_2RuO_4 thin films. Given the fact that superconducting Sr_2RuO_4 thin film is very rare and tricky to grow, as evidenced in the report in 2010[14], it is hardly surprising that this is only the second report amongst the research community at superconducting Sr_2RuO_4 films. It is therefore necessary to delve deeper into the in-depth structural parameters in relation to the low temperature behavior of superconducting Sr_2RuO_4 thin films.

7.1 XRD Characterization of Superconducting Sr_2RuO_4 Thin Films

An ablation frequency of 2 Hz and laser fluence of 1.5 J/cm^2 was fired at the rotating target during deposition. The target to substrate distance was 7.5 cm. As high temperature is favorable to getting both phase-stable and structurally perfect films, the deposition temperature was optimized at 950 °C. The O_2 pressure was kept at 7.5 mTorr throughout the deposition and during cooling to room temperature after growth.

XRD was first carried out to study the structural properties and phase purity of the superconducting Sr_2RuO_4 thin films. As shown in the θ-2θ scan in Figure 7.1(a), the dominant phase in the film is Sr_2RuO_4, and all the (0 0 l) peaks indicates a c-axis orientation. Thickness fringes were observed around the (0 0 6) Sr_2RuO_4 peak, as shown in Figure 7.1(b). Such fringes are constructive interferences, resulting from uniform

film thickness, regular lattice periodicity, smooth film surface, and clear film-substrate interface over the x-ray illuminated volume[117]. The simulation curve based on equation:

$$thickness = \frac{\lambda}{2\Delta\theta * cos\theta} \quad (7.1)$$

matches well with the experimental data, as can be seen in Figure 7.1(b). In this equation, λ is the wavelength of the x-ray (0.15418 nm), θ is the Bragg angle in radians, and $\Delta\theta$ is the separation between adjacent fringes. By calculation, the thickness of the film is about 31 nm ± 2 nm, the estimation of the thickness error can be found in Appendix I.

As shown in Table 6.1 in Chapter 6, the *in-plane* lattice parameter of LSAT substrate is 0.54682 ± 0.00015 nm (JCPDS No. 01-086-1840) and the *in-plane* lattice parameter of bulk Sr_2RuO_4 is 0.38730 ± 0.00003 nm (JCPDS No. 01-082-1096). Therefore, a minimum lattice mismatch of only 0.16% can be achieved by the 45° *in-plane* rotation of Sr_2RuO_4 ($\sqrt{2}$ x 0.38730 nm = 0.54772 nm) with respect to LSAT (0.54682 nm). The small lattice mismatch between LSAT substrate and Sr_2RuO_4 is important in that it can almost eliminate possible lattice distortion or disorder due to strain relaxation. As shown in Figure 7.1(c), the four sharp peaks of Sr_2RuO_4 lie 45° away from those of the LSAT substrate, indicating not only the perfect c-axis oriented growth of Sr_2RuO_4 on LSAT substrate, but also an *in-plane* epitaxy relation of [1 1 0] Sr_2RuO_4 || [1 0 0] LSAT. This is shown in Figure 7.1(d).

Figure 7.1(e) shows the reciprocal space map (RSM) of the (1 0 11) Sr_2RuO_4 and (1 1 6) LSAT reflections. As expected, the Sr_2RuO_4 thin film is fully strained *in-plane* with respect to the LSAT substrate, as indicated by the dotted line.

In short, these different XRD scanning modes indicate a near-perfect Sr_2RuO_4 crystal structure over a large area of the film.

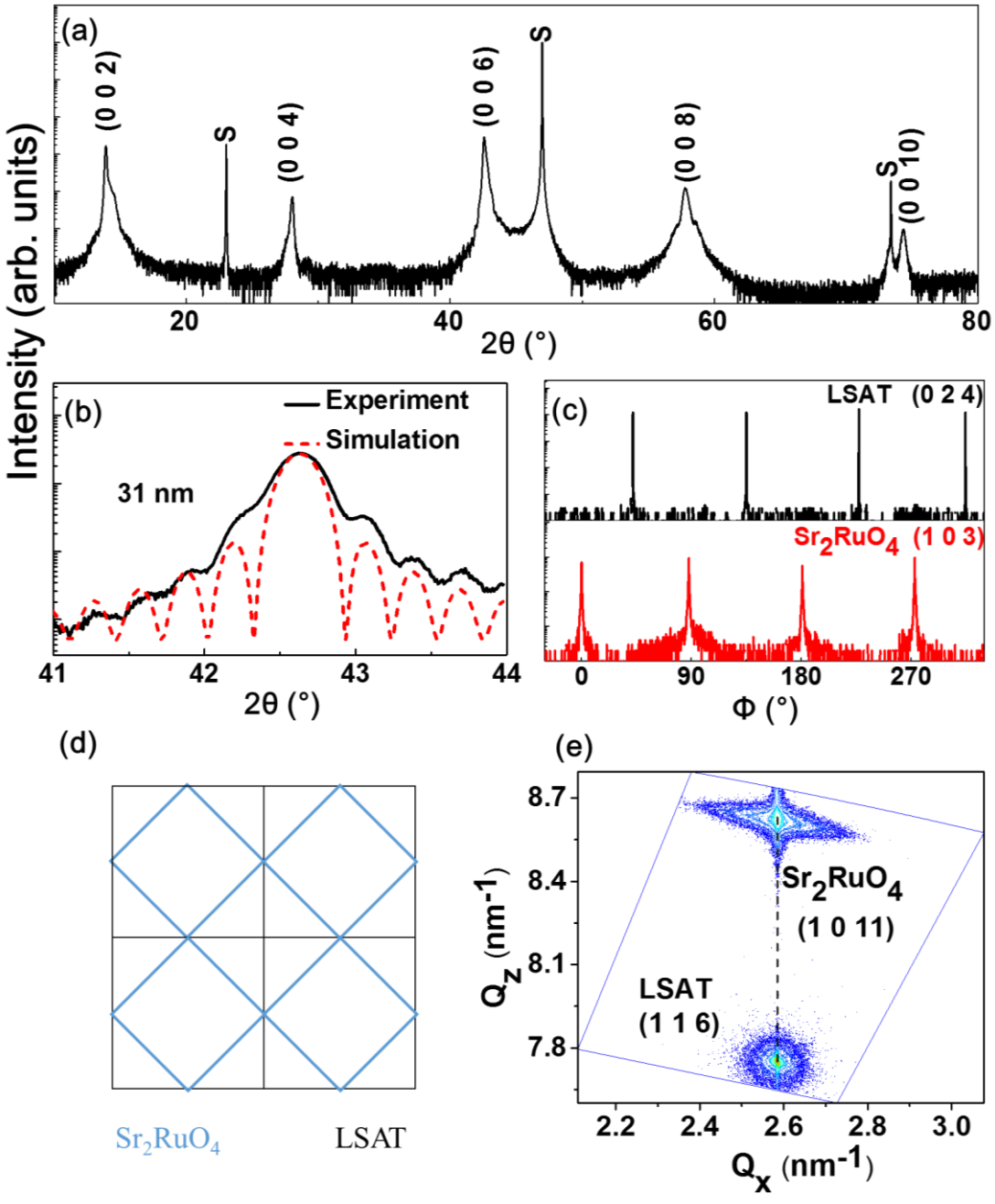

Figure 7.1 (a) *θ-2θ* result of Sr_2RuO_4 thin film grown on (0 0 1) oriented LSAT substrate. (b) Thickness fringes and simulation result near (0 0 6) Sr_2RuO_4. (c) *Φ* scan of (1 0 3) Sr_2RuO_4 and (0 2 4) LSAT. (d) Illustration of the crystal *in-plane* lattice matching between Sr_2RuO_4 and LSAT. One square denotes one unit cell. Blue stands for Sr_2RuO_4 and black for LSAT. (e) RSM of (1 0 11) Sr_2RuO_4 and (1 1 6) LSAT.

7.2 Transport Measurement of Superconducting Sr_2RuO_4 Thin Films

In relation to the XRD results, it is interesting to study the electrical transport behavior of the superconducting Sr_2RuO_4 films. The low-temperature measurements were performed in Napoli under the help from Prof. Francesco Tafuri and Dr. Davide Massarotti, using a helium-3 refrigerator by a four point probe *in-plane* geometry. The refrigerator was equipped with a room temperature electromagnetic interference filter stage followed by low-pass RC filters anchored at 1.5 K, with a cut-off frequency of about 1 MHz, and by copper powder filters anchored at the sample stage, with a cut-off frequency of about 1 GHz.

In order to get a thorough understanding of the transport behavior, Sr_2RuO_4 thin films with metal-insulating and fully metallic behavior were compared. The resistance as a function of temperature plot for the three representative films is shown in Figure 7.2(a). The residual resistivity ratios (RRR) $R_{300K}/R_{4.2K}$ for superconducting, metallic, and metal-insulating Sr_2RuO_4 film are shown in Table 7.1, where R_{300K} is the resistance at 300 K, and $R_{4.2K}$ is the resistance at 4.2 K. At low temperatures, the resistance of a material is mainly due to the impurity or defect scattering of electrons. In this sense, high RRR values are associated with pure samples. Therefore, RRR can be used as a rough indicator of the sample overall quality.

sample	Superconducting Sr_2RuO_4 thin film	Metallic Sr_2RuO_4 thin film	Metal-insulating Sr_2RuO_4 thin film
RRR	6.3	5	1.8

Table 7.1 RRR from 300 K to 4.2 K for superconducting, metallic, and metal-insulating Sr_2RuO_4 films.

The results in Table 7.1 demonstrate that the superconducting Sr_2RuO_4 thin film has the highest RRR, with the metal-insulating Sr_2RuO_4 thin film having the lowest RRR. This suggests that films with a higher RRR generally are more likely to show

superconductivity. Taking into consideration of the fact that superconductivity in Sr_2RuO_4 is sensitive to impurities and defects[15], the correlation between a high RRR and the superconductivity revealed in this study is self-evident. In comparison, a much higher RRR of 80 was reported for the previous superconducting Sr_2RuO_4 thin film (onset T_c at 0.9 K)[14]. Interestingly, superconductivity was still observed in my film despite a relatively lower RRR value.

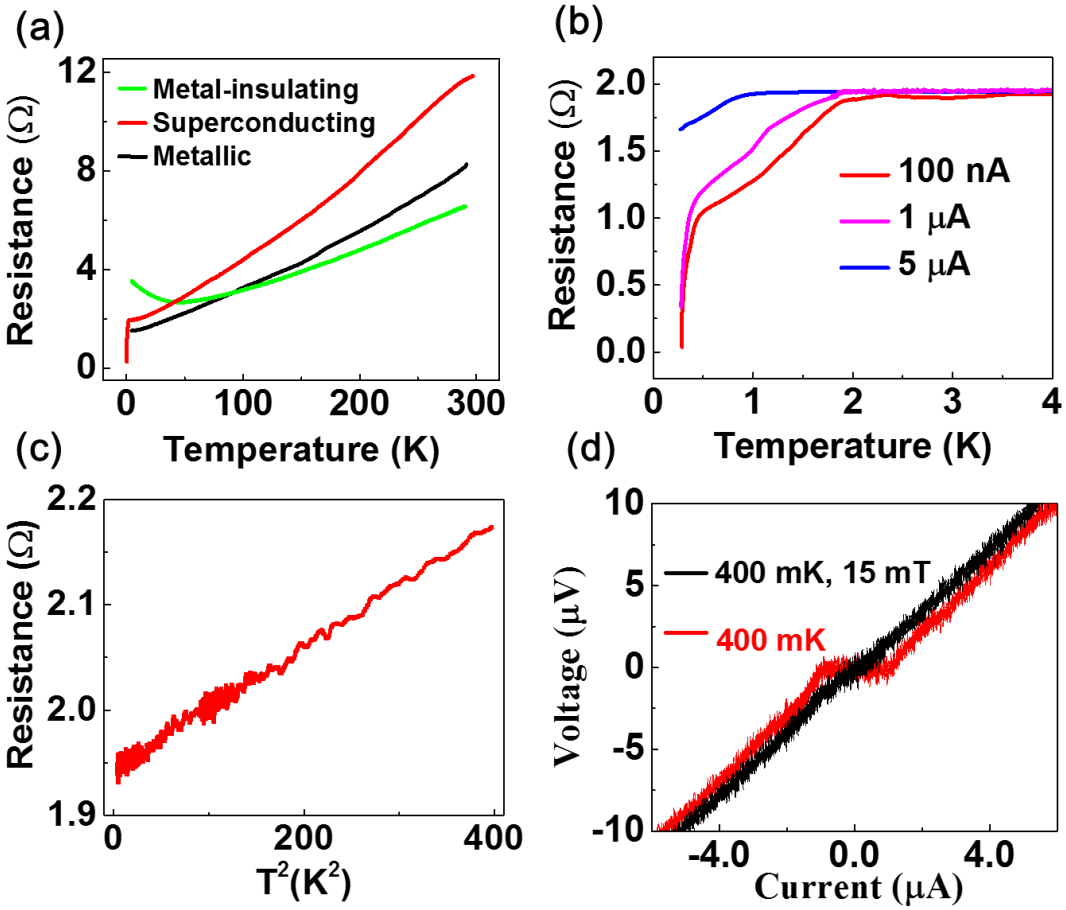

Figure 7.2 (a) *In-plane* resistance as a function of temperature for metal-insulating, metallic and superconducting Sr_2RuO_4 thin films from 300 K to 0.3 K with the bias current of 1 μA. (b) *In-plane* resistance as a function of temperature for the superconducting Sr_2RuO_4 thin film under bias currents of 100 nA, 1μA, and 5 μA, from 4 K to 0.3 K. (c) A quadratic correlation between resistance and temperature for superconducting Sr_2RuO_4 thin film between 20 K and 2 K. (d) Current-voltage characteristics of superconducting Sr_2RuO_4 thin film at 400 mK with and without an *in-plane* magnetic field of 15 mT.

We further measured the low temperature behavior of the superconducting Sr_2RuO_4 thin films. Below 4 K, the *in-plane* resistance of the superconducting Sr_2RuO_4 thin film is measured with different bias currents, as shown in Figure 7.2(b). As expected, the superconducting transition is suppressed to lower temperatures as the bias current increases. Zero resistance was observed when using the bias current of 100 nA. This is shown in the red curve. Two features in the plot need to be mentioned. The first one is the superconducting broad transition before 0.5 K, which could be due to the sample inhomogeneity and defects. The other one is the slight enhancement of the superconducting onset transition temperature, which is 1.9 K. In comparison, the highest T_c for pure Sr_2RuO_4 single crystal is only 1.5 K[16]. The possible reason for this enhanced superconductivity is discussed in the next section.

In addition, similar to the correlation found for superconducting Sr_2RuO_4 single crystal discussed in Chapter 3, there is also a quadratic correlation for my superconducting Sr_2RuO_4 film between the *in-plane* resistance and temperature between 20 K and 2 K. This is shown in Figure 7.2(c). It indicates a Fermi-liquid[4] behavior similar to in the superconducting Sr_2RuO_4 single crystals, in which the electron–electron interaction dominates the resistivity[45] of a material.

Last but not least, a zero-voltage supercurrent was observed at 400 mK, and the critical current was found at about 1 μA. This is shown in Figure 7.2(d). After the magnetic field of 15 mT was applied along the *in-plane* direction, the current–voltage characteristic of the superconducting Sr_2RuO_4 thin film becomes linear. This implies the B_{c2} for this superconducting Sr_2RuO_4 thin film is not bigger than 15 mT.

7.3 Structural and Transport Analysis Showing Localized Enhanced Superconductivity

Based on the data from both XRD and transport studies of my film, a few deductions can be made regarding the nature of its superconductivity. But before arriving at any conclusion, it is important to note that when measuring the transport properties of the sample, more than four wire bonds were used. This is shown in Figure 7.3. Although only four wire bonds are needed In four-point probe geometry measurement, the extra bonds can be served as backup connections in case of wire breaking. More importantly, different combinations of wire bonds offer an alternative to check the transport homogeneity of the sample. Therefore, data can be collected from different areas in one sample.

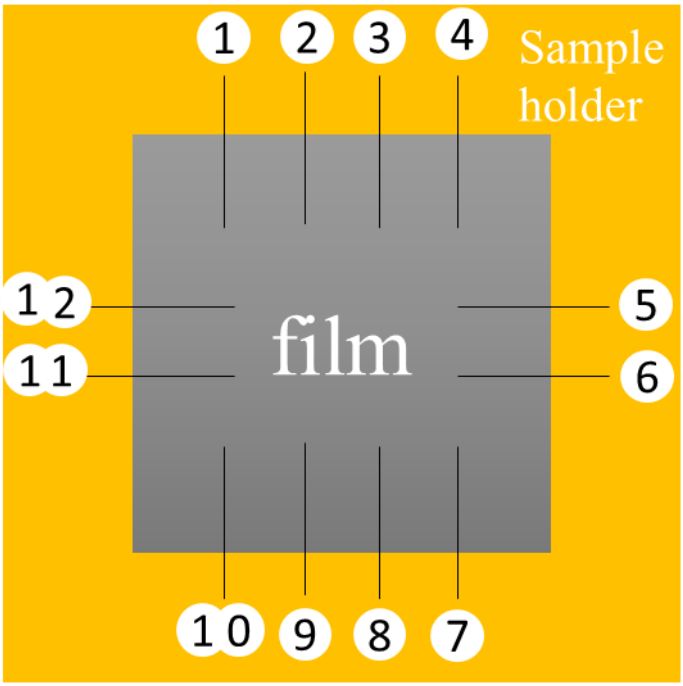

Figure 7.3 Illustration of the wire bonding locations on film. Orange represents the sample holder, grey represents the film, and black lines represent the wire bonds.

As a matter of fact, not all combinations of wire bonds on the sample showed superconducting behavior. Some regions of the thin film were non-superconducting

(metallic) down to 0.3 K while some other regions were superconducting. As an example, when the part from wire bonds combination (1, 2, 3, 4) or (4, 5, 6, 7) are superconducting; while those from (7, 8, 9, 10) or (10, 11, 12, 1) are not superconducting, this means that the superconductivity was not homogeneously distributed throughout the film, but rather a localized phenomenon. This is similar to the case observed in my real metallic films. In other words, while some parts of the film were sufficiently free of defects to maintain superconductivity, some were not. The exact length scale of the localized area is unknown, because it is experimentally challenging to cover the whole film with wire bonds. The fact that the average spacing between wire bonds in the experiment is about 1 mm shows that the dimension of the localized area is at least commensurate to the wire bond spacing (e.g. 1 mm).

Moreover, both the relatively small RRR and the broad superconducting transition in Figure 7.2(a) and 7.2(b) indicate that defects are present. As already known, Sr_2RuO_4 is highly sensitive to defects and impurities[15]. In a perfect Sr_2RuO_4 crystal where the *in-plane* coherence length is 66 nm[16], the superconductivity is easily destroyed by any defect within the length scale. Besides, an *in-plane* magnetic field of only 15 mT is enough to suppress the superconductivity. This is much lower than the B_{c2}//ab (1.5 T)[4] in bulk Sr_2RuO_4 crystal. Therefore, the superconductivity observed in the film was localized and much weaker.

In addition, two possible mechanisms commonly seen in the literature that could be responsible for the observed enhanced T_c of 1.9 K in my film were considered. They are the presence of a secondary phase (Ru)[8] and structural defects[90, 131]. On the first sight, the second possibility seems to contradict the fact that defects are known to destroy superconductivity in Sr_2RuO_4. It will be explained in the following part. Before we go any further, it helps to first examine the existence of secondary phase. As described in Chapter 3, the onset T_c can be enhanced to 3 K in the Sr_2RuO_4–Ru eutectic system, where Ru lamellae are embedded in the Sr_2RuO_4 matrix[8]. However, from the structural data presented so far, no obvious sign of a secondary phase has been observed in my film. Nevertheless, there are some asymmetries in the profiles of Sr_2RuO_4 peaks

in Figure 7.1(a), which can be identified more as structural defects rather than secondary phases.

In other studies on the growth of Sr-Ru-O thin films, similar asymmetries on the XRD scan were also reported[80], as shown in Figure 7.4(a). There is a gradual change in the phases of the films. The major phase in the film changes from $Sr_3Ru_2O_7$ to some other intermediate phases and finally to the Sr_2RuO_4 phase. As Sr-Ru-O series are layered structured, it is reasonable to think the difference between those intermediate phases are only difference in the number of sub-unit cell layers, which caused the change in the unit cell c lattice parameter values of certain regions in the films. A close comparison between the XRD scan of Sr_2RuO_4 in my project in Figure 7.1(a) and the scan in Figure 7.4(a) indicated some similarities.

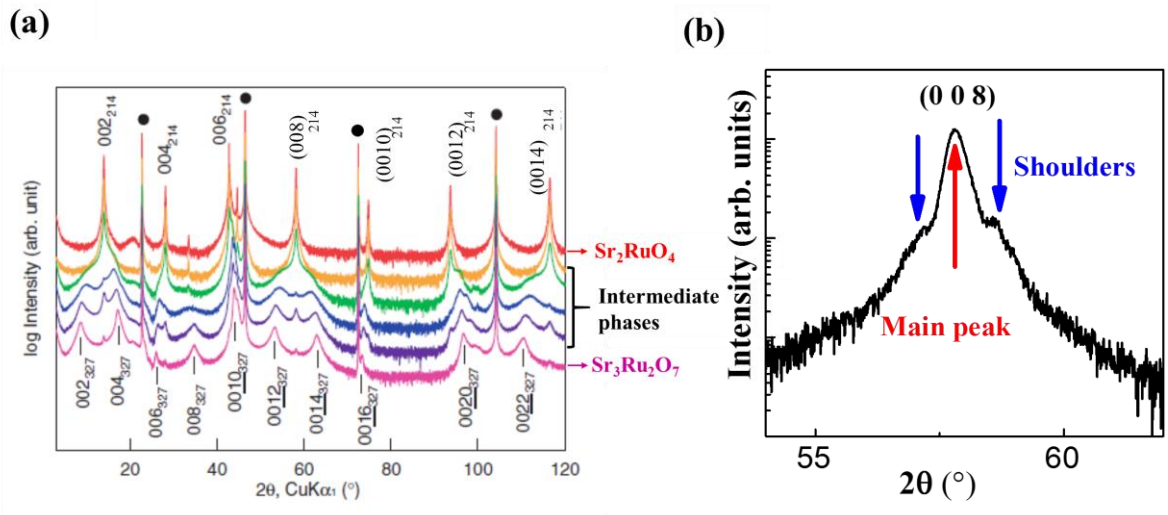

Figure 7.4 (a) XRD scan of a series of Sr-Ru-O films grown by pulsed laser deposition[80]. (b) An example of how the main peaks and shoulders in the analysis are defined.

Take the example of the (0 0 8) peak, as shown in Figure 7.4(b), which clearly consisted of two weaker peaks around a strong peak. This is similar to the green colour plot in Figure 7.4(a). The two weak peaks were named as shoulders, whereas the strong peak was the main peak, which can be de-convoluted by peak profile fitting using XRD data analysis software Highscore. In fact, the asymmetries can be interpreted as variations in the (0 0 *l*) plane d-spacing of the Sr_2RuO_4 thin film. According to:

$$c_l = l \times d_l \quad (7.2),$$

where c_l and d_l are the c-axis value and the d-spacing obtained from the (0 0 *l*) reflection, the asymmetries can also be regarded as the c-axis variations in different regions of the film.

Before trying to calculate the c lattice parameter values, the sample displacement error during XRD measurement caused by sample unevenness has to be eliminated. As a matter of fact, the bottom of the sample is usually not flat but with many dirt, which is due to the dried silver paint used in PLD. This results in the displacement error in the XRD. There is a correction equation for the sample displacement error:

$$\frac{\Delta d_l}{d_l} \propto \frac{cos^2\theta}{sin\theta} \quad (7.3)^{[132]},$$

where Δd_l are the change or error in the d-spacing of the (0 0 *l*) reflection, and θ is the Bragg angle. Now combining equation (7.2) and (7.3),

we get

$$\frac{\Delta c_l}{c_l} \propto \frac{cos^2\theta}{sin\theta} \quad (7.4),$$

where Δc_l is the change or error in the c-axis of the (0 0 *l*) reflection. By extrapolation $cos^2\theta/sin\theta$ to zero, c-axis value without the displacement error can be obtained. Ideally, the c-axis of a perfect film and substrate with a sample displacement error have a linear dependency on $cos^2\theta/sin\theta$, and so the extrapolation $cos^2\theta/sin\theta \rightarrow 0$ produces the most accurate c lattice parameter values.

The c lattice parameter values of the superconducting Sr_2RuO_4 thin film, metallic Sr_2RuO_4 thin film, and the LSAT substrate determined from the asymmetric main peaks are plotted as a function of $cos^2\theta/sin\theta$, as shown in Figure 7.5(a). A linear trend is found for the LSAT substrate and the main peaks of the two thin films. The extrapolation to 0 is shown by the three dashed lines in Figure 7.5(a). This linear dependency can be attributed to the structurally perfect regions in the thin films.

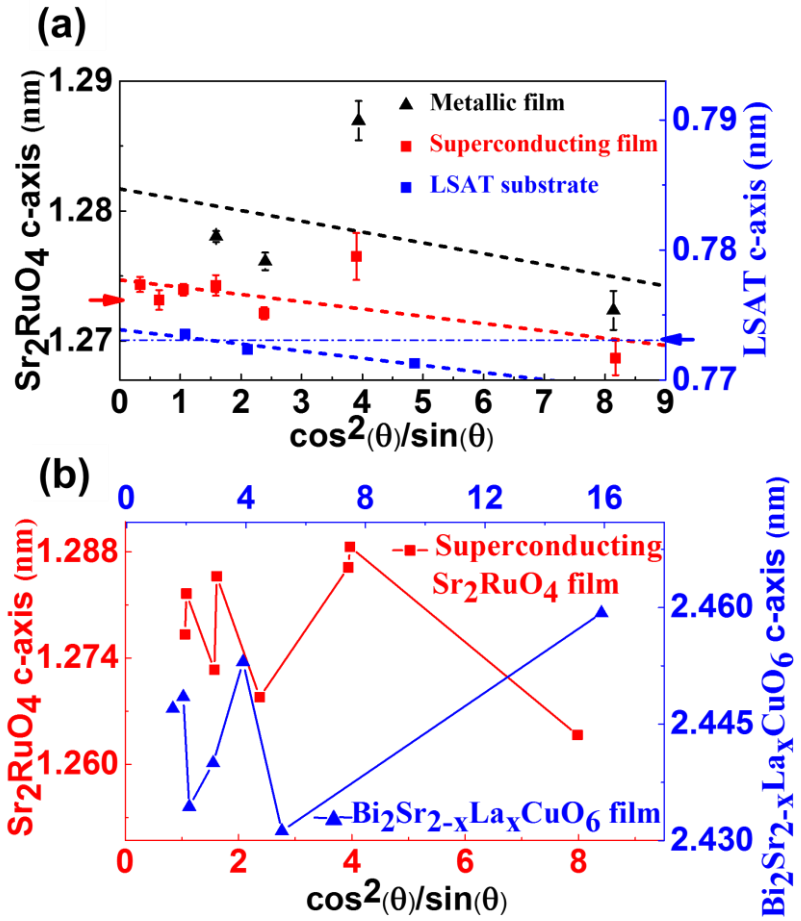

7.5 (a) Comparison of the c-axis of main peaks in superconducting Sr_2RuO_4 thin film, metallic Sr_2RuO_4 thin film, and the LSAT substrate. The short dashed lines are extrapolations to zero using the sample displacement error correction equation. The red arrow indicates the bulk c-axis value for Sr_2RuO_4 and the blue arrow for bulk LSAT. (b) c-axis of shoulder oscillation in superconducting Sr_2RuO_4 film and $Bi_2Sr_{2-x}La_xCuO_6$ film. The $Bi_2Sr_{2-x}La_xCuO_6$ data points were reprinted from reference[133].

Furthermore, the c lattice parameter values for the LSAT substrate, and the main (0 0 *l*) peaks for the metallic and superconducting Sr_2RuO_4 thin films based on the extrapolation in Figure 7.5(a) are compared and shown in Table 7.2. As expected, the c-axis for LSAT is close to its standard value (0.7729 ± 0.0003 nm, JCPDS No. 01-086-1840). However, the c-axes for both the metallic and superconducting Sr_2RuO_4 thin films are larger than those for bulk single crystals (1.27323 ± 0.0009 nm, JCPDS No. 01-082-1096). Moreover, both of the *in-plane* strain and *out-of-plane* strain have

been calculated for superconducting and metallic Sr_2RuO_4 thin films using equation (4.4) discussed in Chapter 4. The *out-of-plane* strain for the two films is bigger than that of an ideal fully strained film on LSAT as shown in Table 7.2. This implies the presence of defects, albeit at a much lower level in the superconducting Sr_2RuO_4 than in the metallic Sr_2RuO_4.

Sample	c lattice parameter values (nm)	*In-plane* strain (%)	*Out-of-plane* strain (%)
LSAT	0.7735	N.A.	N.A.
Ideal Sr_2RuO_4 grown on LSAT	N.A.	-0.16	0.064
Superconducting Sr_2RuO_4 film	1.2747	-0.16	0.12
Metallic Sr_2RuO_4 film	1.2817	-0.16	0.67

Table 7.2 Strain of an ideal Sr_2RuO_4 film on LSAT, the superconducting Sr_2RuO_4 film, and the metallic Sr_2RuO_4 film. All of the films were fully strained to LSAT and the *out-of-plane* strain for the ideal Sr_2RuO_4 film was calculated using the Poisson ratio of bulk Sr_2RuO_4 (0.4)[90].

In addition, a similar plot has been done for the asymmetric shoulders of the superconducting Sr_2RuO_4 film in Figure 7.5(b). However, no correlation can be observed and the fitting does not converge as $cos^2\theta/sin\theta \rightarrow 0$. For comparison, a very similar non-correlated variation of the c lattice parameter as a function of $cos^2\theta/sin\theta$ is also seen in $Bi_2Sr_{2-x}La_xCuO_6$ thin films, as shown in Figure 7.5(b)[133]. Similar to the analysis in reference for the $Bi_2Sr_{2-x}La_xCuO_6$ films[133], the sporadic deviation of the shoulder peaks in my superconducting Sr_2RuO_4 thin film suggests the existence of localized regions whose c lattice parameter differs from the rest of the matrix.

There are several possibilities that can cause c lattice parameter expanding, such as *out-of-plane* strain due to *in-plane* compression, vacancies due to off-stoichiometry, intergrowth or stacking faults which are common in complex oxides. First, the films were tensile fully strained *in-plane* to the LSAT substrate, which would more likely to cause c lattice parameter compression other than expansion. Second, it is true that

vacancies on a particular sub-lattice can cause variations on the c lattice parameter values. The most probable vacancies in oxide materials would be oxygen vacancy. However, films grown in slightly higher oxygen pressure also have similar shoulders as shown in Figure 7.4(b). Therefore, this possibility is less likely. Finally, due to the very similar structural relationship among the Sr-Ru-O series, this c lattice parameter expansion is highly possibly due to some extra sub-unit cell layers along the c-axis. In other words, this can be interpreted as containing extra (0 0 *l*) layers or intergrowth, which are common defects in layered materials[133, 134].

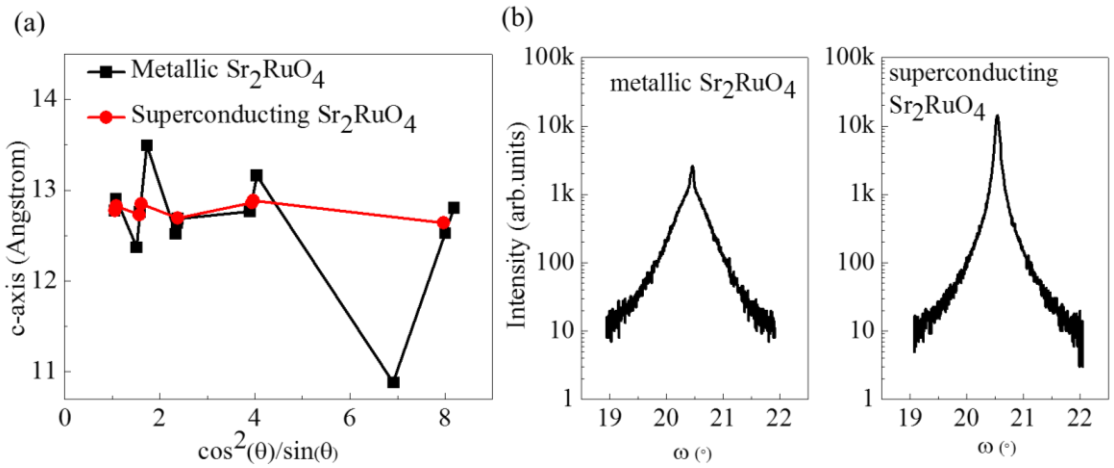

Figure 7.6 (a) c lattice parameter of shoulder oscillation in metallic and superconducting Sr_2RuO_4 film; (b) (0 0 6) rocking curve of both metallic and superconducting Sr_2RuO_4 film, with the FWHM 0.0994° and 0.0844°, respectively.

On the other hand, the metallic film has a much more sporadic c lattice parameter as a function of $cos^2\theta/sin\theta$ profile, as shown in Figure 7.6(a). For comparison, the superconducting data already shown in Figure 7.5(b) were also added in Figure 7.6(a), which have almost been linear compared to the oscillation of the metallic data. In addition, the (0 0 6) rocking curves of both the metallic and the superconducting Sr_2RuO_4 were shown in Figure 7.6(b). The broader FWHM in the metallic Sr_2RuO_4 film obviously implies a higher level of defects.

In general, defect formation can be associated with both the layered-structure nature and the fabrication process of Sr_2RuO_4. As has been described in Chapter 6, PLD is known as a non-equilibrium growth technique[135]. Although stoichiometric material

ablation is guaranteed during target ablation, the process in which the plume deposits onto the substrate may not be stoichiometric, and can be affected by many deposition factors: target to substrate distance, laser fluence, deposition temperature, gas pressure, laser ablation frequency[133].

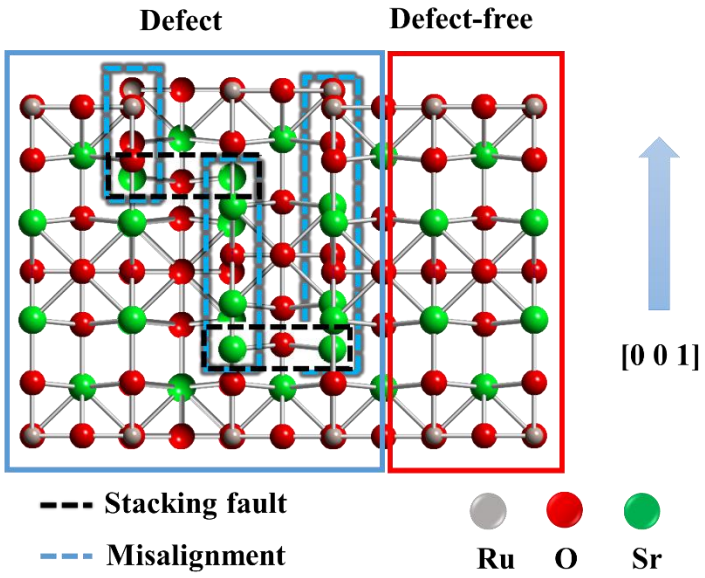

Figure 7.7 A schematic drawing of the Sr_2RuO_4 crystal showing a defect-free region as well as an area with defects where misalignment was caused by stacking faults.

As shown in Figure 7.7, Sr_2RuO_4 has a layered structure. Therefore, during deposition, it is highly possible to have structural defects in the form of stacking faults. When neighboring regions of the film with stacking faults coincide, the atomic bonding can create a slight *out-of-plane* misalignment. This could disrupt the continuity in the RuO_2 plane, which is likely to be detrimental to superconductivity[17]. That is why the RRR of my Sr_2RuO_4 thin film is relatively lower, and the superconductivity is localized.

On the other hand, the presence of coherent structural defects with a different d-spacing will also inevitably create micro-strained regions of structurally perfect material. Uniaxial strain as small as 0.3% has been found to greatly enhance the T_c onset up to 1.9 K[90, 136, 137]. The overall lattice mismatch strain is biaxial. However, the *out-of-plane* strain that arises due to elastic coupling with the biaxial strain is uniaxial, which could have partly contributed to the enhancement of T_c as discussed in Chapter 3. In addition, the localized strain associated with the included stacking faults can also

be expected to have a uniaxial nature[84] and consequently could contribute to T_c enhancement. Additionally, extra layers like a stacking fault itself can also lead to edge dislocations. It has been reported that dislocations in Sr_2RuO_4 crystals can result in enhanced T_c and step-like transition[131], which is consistent with my superconducting thin film. The much smaller B_{C2}//ab and the small value of the critical current deduced in Figure 7.2(e) suggest that the superconducting regions are only weakly coupled in this sample.

In summary, localized superconductivity has been observed in my epitaxial c-axis oriented Sr_2RuO_4 metallic thin film on LSAT grown by pulsed laser deposition. The superconducting onset is 1.9 K, which is higher than the maximum bulk value. In addition, the observed superconductivity in the film was localized. The variations from the analysis of the c lattice parameter values indicate the existence of defects, which could be the reason for the localized nature of the superconductivity. On the other hand, the defect can induce micro-strain around it, which is thought to be related to the enhanced superconductivity.

In my samples, it is hard to see how many samples displayed superconductivity. Since the superconductivity was localized as discussed in this chapter, and it is impractical to measure every point on the film. Since the superconductivity is localized, the wire bonding location has to be exactly coincide with the perfect region in the sample to show superconductivity. Thus, the possibility that localized superconductivity also exists in those metallic films cannot be excluded. Therefore, it is difficult to conclude about how reproducible the superconducting Sr_2RuO_4/LSAT film is, because only this sample was rigorously measured, which took huge resource and time commitments.

Nevertheless, as mentioned in Chapter 6 conclusion, the reproducibility of metallic samples is not a problem as long as the deposition parameters fall within the optimized range.

Despite the localized nature of superconductivity, this work delivers hope and opens an exciting possibilities for further explorations of superconducting Sr_2RuO_4 thin

films because superconductivity was shown to be possible in the film. This result, albeit a big step forward in this area of research, still implies that the bottleneck for further study of Sr_2RuO_4 lies in the fabrication process. The problem of the localization of superconductivity needs to be solved. Therefore, finding a simple, consistent and relatively larger error tolerance way of fabrication is of paramount importance for my subsequent study. In the next chapter, a more consistent way to grow superconducting Sr_2RuO_4 thin films is discussed.

Chapter 8 Partial Superconducting Sr_2RuO_4 Thin Films on Nb-$SrTiO_3$

In the previous chapter, superconductivity has been observed in Sr_2RuO_4 thin films grown on LSAT substrate. Despite the achievement, inconsistency in the film quality is still the biggest problem concerning the growth of superconducting Sr_2RuO_4 thin films. Specifically, the localization of superconductivity in the superconducting Sr_2RuO_4 thin films and the poor reproducibility have made it difficult to do further processing with the superconducting Sr_2RuO_4 thin films. Therefore, a more reliable method is welcome. In this study, partially superconducting Sr_2RuO_4 thin films have been consistently grown by PLD following the optimization process in Chapter 6.

8.1 Characterization of Sr_2RuO_4 Thin Films on Nb-$SrTiO_3$

Previously in the optimization of c-axis oriented Sr_2RuO_4 thin films, LSAT was chosen as the substrate because of its small lattice mismatch with Sr_2RuO_4, which is also intuitive for epitaxial thin film growth. However, given the fruitless optimizations to obtain consistent superconducting Sr_2RuO_4 thin films on LSAT substrates, it is necessary to devise a new method.

Apart from the deposition parameters mentioned in Chapter 6, substrate condition is no less important for high quality epitaxial thin film growth. Similar to LSAT, STO also has a perovskite structure. The unit cell of STO is cubic, and the cell parameter is 0.3905 nm, as can be found in Table 6.1. Unfortunately, my optimizations of Sr_2RuO_4 thin films on the STO substrates only yielded metallic films, at best.

There are several reports[138, 139] on high quality FeSe thin films grown on Nb doped STO (Nb-STO) compared to the normal insulating STO. Nb-STO is made from substituting Ti^{4+} in the normal insulating STO matrix using Nb^{5+}[140]. This makes Nb-STO electrically conductive, and also brings about other improved properties like

thermoelectric property[141]. Inspired by the literature, 5wt% Nb doped STO substrates were used for the growth of Sr_2RuO_4 thin films. The optimized growth conditions for the superconducting Sr_2RuO_4 thin films on Nb-STO substrates were found to be: deposition temperature 950 °C, oxygen pressure 7.5 mTorr, target to substrate distance 7.5 cm, laser fluence 1.5 J/cm^2, ablation frequency 2Hz, which is nearly identical to the growth conditions optimized on LSAT.

After deposition, XRD was first used to identify the phase composition and epitaxy of the as-deposited thin films. All the peaks from the *θ-2θ* scan in Figure 8.1(a) can be identified to the (0 0 *l*) families of Sr_2RuO_4 and/or Nb-STO substrate, suggesting the c-axis orientation. Figure 8.1(b) demonstrates the rocking curves of both the (0 0 6) Sr_2RuO_4 and (0 0 2) Nb-STO. The FWHM of Sr_2RuO_4 rocking curve is only 0.06° against that of Nb-STO, which is about 0.02°. This confirms the good epitaxial growth of c-axis oriented Sr_2RuO_4 on Nb-STO even though the lattice mismatch between Sr_2RuO_4 and Nb-STO is bigger than Sr_2RuO_4 and LSAT.

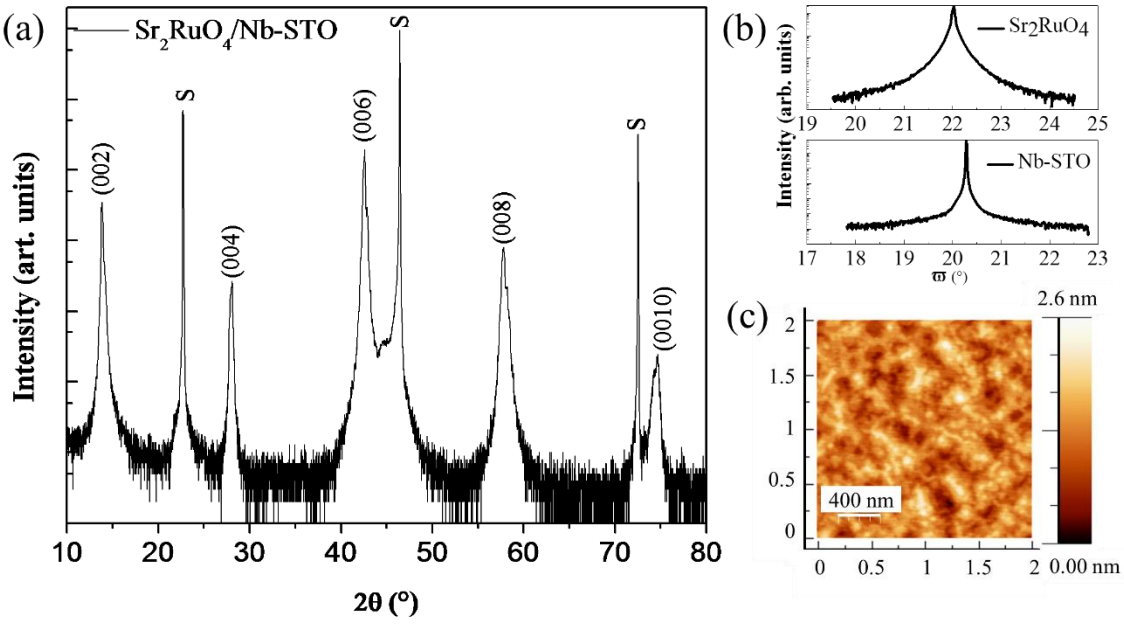

Figure 8.1 (a) *θ-2θ* pattern of a typical Sr_2RuO_4 thin film grown on Nb-STO substrate; (b) rocking curve of (0 0 6) Sr_2RuO_4 and (0 0 2) Nb-STO; (c) The AFM topography of the Sr_2RuO_4 film grown on Nb-STO with the thickness of about 60 nm.

In addition, a very smooth surface of the as-deposited Sr_2RuO_4 thin films has been observed under AFM. As seen from Figure 8.1(c), for a Sr_2RuO_4 thin film with the thickness of 60 nm, the root mean square (RMS) roughness is about 0.35 nm. This is smoother compared to the surface roughness in the previous chapters, which is about 0.8 nm.

Atomic resolution scanning transmission electron microscopy (STEM) with high-angle annular dark-field imaging (HAADF) was used to characterize the cross sectional microstructures of the Sr_2RuO_4 thin film grown on Nb-STO. This was carried out in collaboration with Prof. Kelvin Hongliang Zhang, Dr. Daniel Pingstone and Dr. Vlado Lazarov from University of York. After receiving the data, I made the following analysis and the model based on the results. The interface between the Sr_2RuO_4 thin film and the Nb-STO substrate was first investigated in Figure 8.2(a). An abrupt interface can be observed, with atoms from the Sr_2RuO_4 thin film matching well with those from the Nb-STO substrate, demonstrating the good epitaxial growth.

The body of the Sr_2RuO_4 thin film was subsequently investigated. Large perfect areas with the layer-structures characteristic of Sr_2RuO_4 have been observed. An example is shown in Figure 8.2(b). A much closer inspection in the left side of Figure 8.2(c) revealed the microstructure formed by well-ordered atoms. The periodic patterns marked by the black line along the c-axis direction consists the regular crystal lattice of Sr_2RuO_4, which is the octahedral site of Ru-O and two layers of Sr-O. Next to it is the crystal representation of Sr_2RuO_4. The red lines demonstrate the well-matched structure of my Sr_2RuO_4 thin film with its crystal representation. It should be noted that oxygen atoms are not clearly visible here due to the Z^2 contrast dependence in HAADF, where Z denotes the atomic number. Z of oxygen atom is significantly lower in comparison to that of Sr, Ti, and Ru. As a further step, the cationic crystal representation of Sr_2RuO_4 perfectly overlaps on top of the real Sr_2RuO_4 film structure in [100] viewing direction, as shown in Figure 8.2(d). This clearly demonstrates the good orientation and well-ordered lattice structure in my Sr_2RuO_4 thin film.

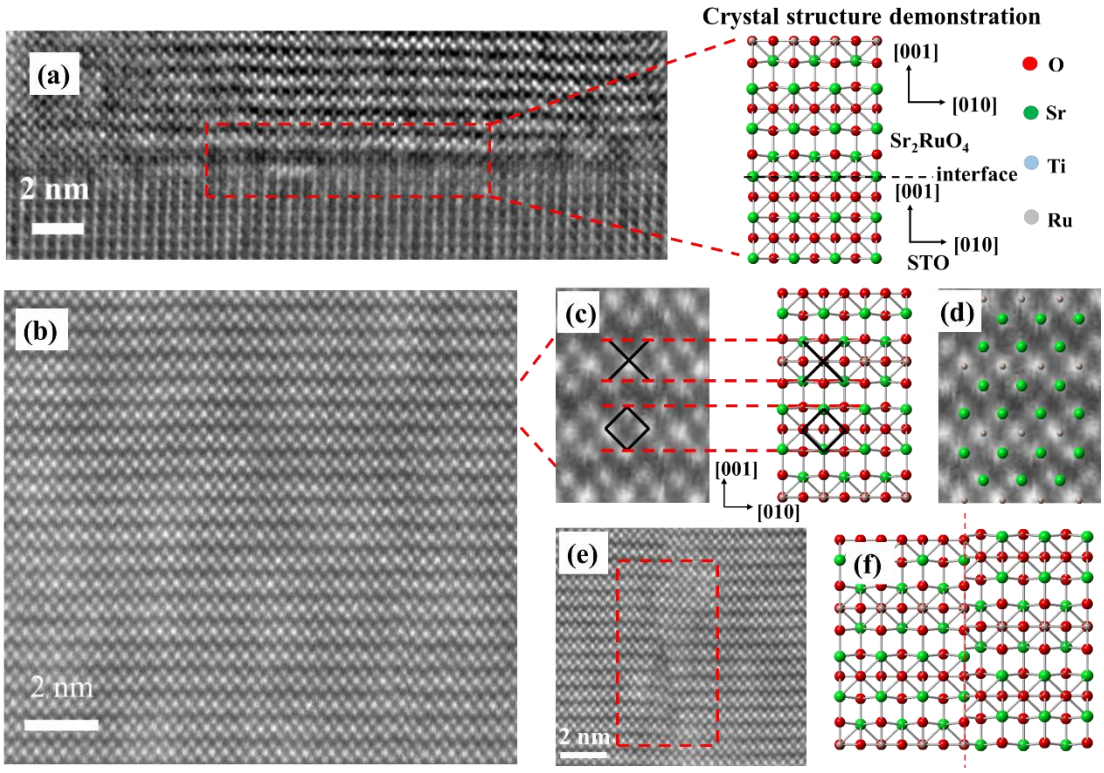

Figure 8.2 STEM-HAADF cross sectional image of Sr_2RuO_4/Nb-STO. (a) The interface between Sr_2RuO_4 and Nb-STO, the right side is the crystal representation of both Sr_2RuO_4 and Nb-STO; (b) An overview of the Sr_2RuO_4 film microstructure; (c) Close-up view of the microstructure and crystal representation of Sr_2RuO_4; the black line represents the periodic patterns; (d) Overlap of the Z-contrast HAADF result and crystal atoms of Sr_2RuO_4, note that oxygen atoms are intentionally omitted; (e) Defects in Sr_2RuO_4 films; (f) A model demonstrating the OPB defect in a crystal.

Although the majority of the Sr_2RuO_4 thin film is free from defects, some localized defects were observed, as shown in Figure 8.2(e). This kind of defect is called the out-of-phase boundary (OPB), where adjacent regions in the crystal are out of registry by a fraction of unit cell parameter. An atomic model of the OPB defect is demonstrated in Figure 8.2(f). In my case as shown in Figure 8.2(e), the adjacent Sr_2RuO_4 areas shifted some distances along [0 0 1] direction, and the magnitude of which is much less than the c-axis parameter. OPBs are common structural defects that occur both in complex oxide thin film and bulk[82, 142, 143]. The nucleation of OPBs could be due to film-

substrate interface misfit or volatile component decomposition[82]. Given the clear interface shown in Figure 8.2(a), the nucleation of OPB in my Sr_2RuO_4 thin film is likely to be from the loss of Ru, which is also very common during Sr_2RuO_4 single crystal fabrication[7]. Unlike the reported OPBs in Sr_2RuO_4 thin films, which propagated into the whole part of the films and destroyed the superconductivity[17], the observed OPB is localized within fraction of film thickness, and the overall lattice is not affected.

8.2 Transport Measurement on Sr_2RuO_4 Thin Films Grown on Nb-$SrTiO_3$ Substrate

The transport properties were measured in our helium-3 probe equipped in the mini-cryofree system from 300 K to 0.3 K. From 300 K downwards, Sr_2RuO_4/Nb-STO is metallic followed by a superconducting transition at low temperature. This is shown in Figure 8.3(a). As a matter of fact, 5%wt Nb doped STO is highly conductive and also superconducting. Although all the wire bonds were made onto the film as shown in the inset in Figure 8.3(a), part of the current can still travel along the c-axis direction down to Nb-STO substrate. In this sense, Nb-STO inevitably contributes to the total observed resistance.

To better interpret the results, a control sample was grown, which is more like an annealed Nb-STO. The process is described in the following. A piece of pure Nb-STO substrate was loaded into the high vacuum PLD chamber. Every step and parameter was exactly the same as the deposition of the Sr_2RuO_4 thin film, including the heating process and the gas pressure, except that no real deposition was done. After this, the transport of the control sample was measured and its resistance as a function of temperature is also shown in Figure 8.3(a), marked in blue. Compared to the Sr_2RuO_4/Nb-STO sample, the much bigger resistance drop in the control sample between 300 K and 2 K indicated that the control sample is much more conductive than Sr_2RuO_4/Nb-STO. In addition, a superconducting transition in the control sample is observed. Compared to the small resistance of the control sample, the much higher resistance of the Sr_2RuO_4/Nb-STO sample implies that a large interface resistance exists between the Sr_2RuO_4 thin film and the Nb-STO substrate.

In Figure 8.3(b), a more detailed investigation of the low temperature resistance as a function of temperature for both Sr_2RuO_4/Nb-STO and the control sample was demonstrated. A very sharp superconducting transition is seen at about 0.4 K in the control sample, which is consistent with the literature records on Nb-STO[144, 145]. In comparison, the plot for Sr_2RuO_4/Nb-STO is different. A step-feature with two resistance drops was observed. The first resistance drop is abrupt, starting at about 1.3

K, corresponding to the T_c of single crystal Sr_2RuO_4. On the other hand, the second resistance drop is more gentle. The resistance slowly decreases over the rest of the temperature range to a finite value. Thus, the terminology partial superconductivity was used instead of superconductivity (to confirm superconductivity, the resistance has to fall to zero). After applying an *in-plane* magnetic field up to 200 mT, the onset T_c of

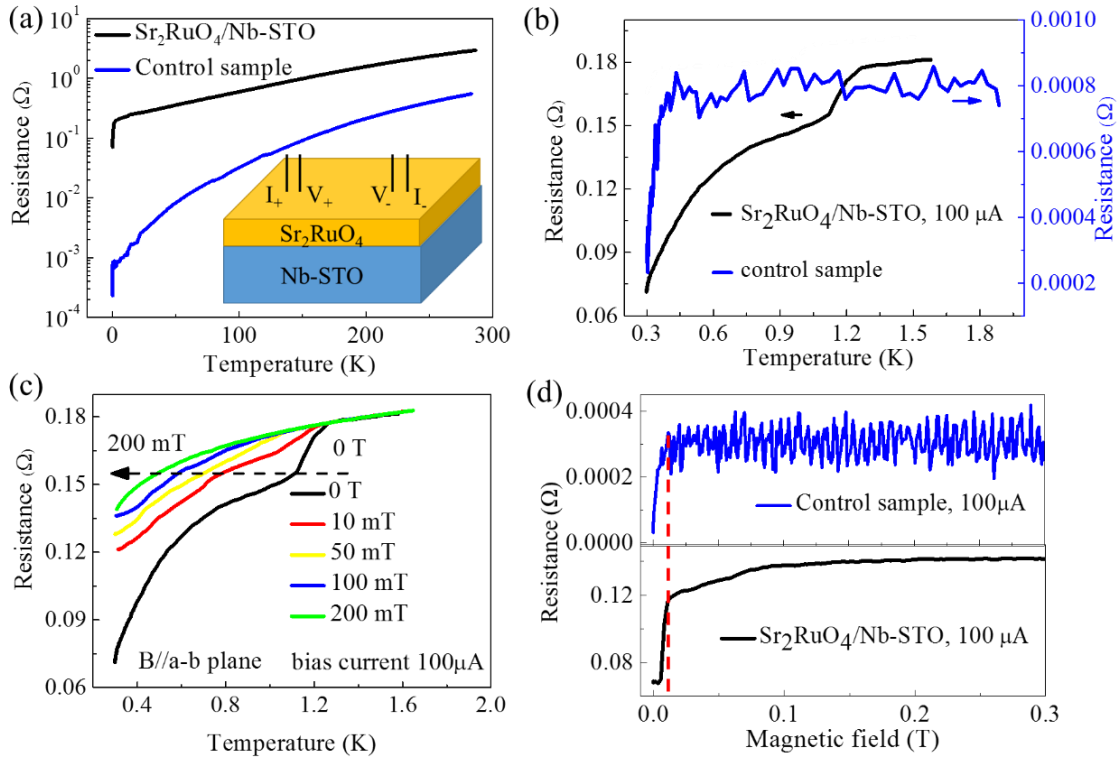

Figure. 3 (a) Resistance as a function of temperature plot of superconducting Sr_2RuO_4/Nb-STO and the control sample from 300 K to 0.3 K. Both the two curves are plotted on a log scale to better resolve the difference. Inset shows the four-point probe geometry for the Sr_2RuO_4/Nb-STO sample. (b) Resistance as a function of temperature curve for both Sr_2RuO_4/Nb-STO and the control sample from 2 K to 0.3 K. (c) Resistance as a function of temperature for Sr_2RuO_4/Nb-STO under different magnetic field between 0.3 K and 1.6 K. (d) Resistance as a function of *in-plane* magnetic field for the control sample (upper panel) and Sr_2RuO_4/Nb-STO (lower panel) at 0.3 K.

Sr_2RuO_4/Nb-STO is suppressed to lower temperatures, as shown in Figure 8.3(c). From the comparison of the resistance plots, it is clear that the broad and much higher

temperature superconducting transition in Sr_2RuO_4/Nb-STO is associated with the superconducting Sr_2RuO_4 thin film, rather than Nb-STO. The partial superconductivity and the step-feature in the superconducting transition could be due to the quality variations in the sample, which can be associated with the localized defects observed in Figure 8.3(e).

To further confirm the presence of superconductivity in Sr_2RuO_4 thin film, the resistance of both the Sr_2RuO_4/Nb-STO and control sample at 0.3 K were measured with an *in-plane* magnetic field. The results are shown in Figure 8.3(d). In the upper panel in Figure 8.3(d), superconductivity of the control sample was completely suppressed at about 10 mT. This magnitude is close to the reported upper critical field (B_{c2}) of Nb-STO[146] at 0.3 K. In comparison, the magnetoresistance of Sr_2RuO_4/Nb-STO is obviously different, as shown in the lower panel of Figure 8.3(d). The resistance starts to decrease gradually below about 150 mT. Then at about 15 mT, roughly the magnitude of the B_{c2} of the control sample, a faster decrease in the resistance is observed. Hence, it can be deduced that the resistance decrease starting at about 150 mT is associated with the superconducting Sr_2RuO_4 thin film, while the sudden drop at about 15 mT can be associated to Nb-STO. In addition, given the large bias current used in my experiments, it can be deduced that the B_{c2} of the Sr_2RuO_4 film should be higher than 150 mT. Although it is still small compared to the B_{c2} of single crystal Sr_2RuO_4 (1.5 T)[16], this is much higher than the previous result, which is only about 15 mT[76]. This once again confirms the superior quality of Sr_2RuO_4 thin films grown on Nb-STO compared to Sr_2RuO_4 thin films grown on LSAT.

8.3 Further Analysis and Conclusions

The above results all confirmed the partial superconductivity in the Sr_2RuO_4 thin films grown on the Nb-STO substrate. Moreover, several different wire bond locations of the same sample have been measured, consistent with the way the measurement was done for the previous localized superconducting Sr_2RuO_4 thin film on LSAT. In Sr_2RuO_4/Nb-STO, partial superconducting transitions (where superconducting transition was observed, but not to zero resistance value) were observed for all wire bond locations (e.g. 1 mm spacing between each wire bond). Although wire bonds cannot cover the whole area of the films, the fact that partial superconductivity was observed on all measured locations suggests that superconductivity in Sr_2RuO_4/Nb-STO was relatively **homogeneous** compared to films grown on LSAT in chapter 7.

As a further step, the consistency of superconducting Sr_2RuO_4 thin films on Nb-STO was also investigated. Specifically, two more Sr_2RuO_4 thin films with similar thickness (about 60 nm) to the one discussed so far were grown on Nb-STO. For better comparison, the resistance as a function of temperature of the three samples were shown in Figure 8.4(a), with the name as S3, S2, and S1. The profiles were similar with two resistance drops at similar temperatures. To better resolve the differences, their temperature derivatives of resistance were plotted in the lower panel in Figure 8.4(a). It is clear that the first resistance drops occur at about 1.3 K, followed by the second resistance drops at about 0.8 K. This strongly demonstrates that superconducting Sr_2RuO_4 films can be consistently grown on Nb-STO.

In addition, Sr_2RuO_4 thin films with different thicknesses were grown on Nb-STO to study the effect of film thickness on the their T_c values. The results are shown in Figure 8.4(b). It is clear that as the film thickness increases, the T_c decreased, and vice versa. This can be understood in terms of strain development in thin films as discussed in Chapter 4. Very thin films remain highly strained by the substrate even in the presence of big lattice mismatch between the film and substrate. As the film continues growing, strain relaxation occurs in the form of dislocations and/or other defects, which

releases the strain energy caused by the lattice mismatch. Therefore, in this sense, thicker films inevitably have more defects compared to thinner ones. For Sr_2RuO_4, the superconductivity of which is highly sensitive to defects and impurities[15], therefore it is not hard to see that a thicker film has a lower T_c.

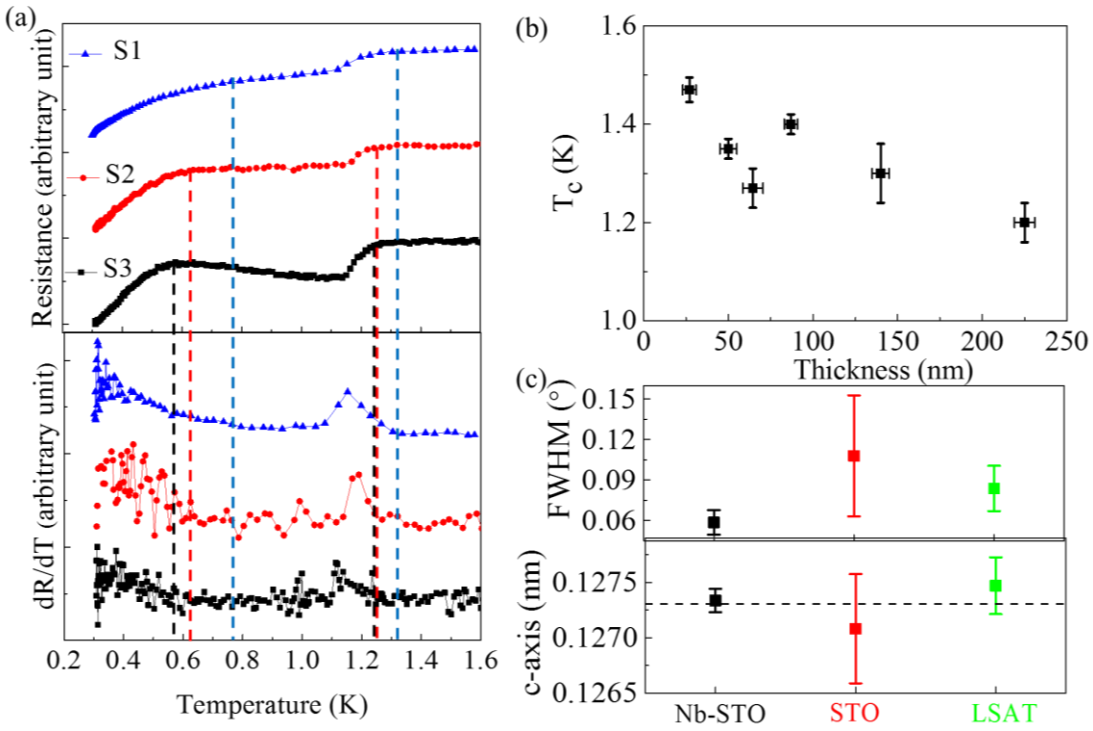

Figure 8.4 (a) Resistance as a function of temperature for three Sr_2RuO_4/Nb-STO samples (upper panel) and temperature derivative of resistance as a function of temperature for them (lower panel). S1 is the sample discussed from the beginning of this chapter. (b) T_c values of several superconducting Sr_2RuO_4/Nb-STO as a function of film thickness. (c) Upper panel: A comparison of the FWHM of the rocking curves of (0 0 6) Sr_2RuO_4 thin films grown on Nb-STO, STO, and LSAT. Lower panel: a comparison of the c-axis values of Sr_2RuO_4 thin films grown on Nb-STO, STO, and LSAT. The dashed line indicated the bulk c-axis value for Sr_2RuO_4. The Sr_2RuO_4 films grown on STO were grown using the same condition as the ones on Nb-STO and LSAT: deposition temperature 950 °C, oxygen pressure 7.5 mTorr, target to substrate distance 7.5 cm, laser fluence 1.5 J/cm^2, ablation frequency 2Hz.

Lastly, it is very interesting to mention that compared to other substrates like LSAT

and insulating STO, superconducting Sr_2RuO_4 film grows consistently on Nb-STO. The exact mechanism is still unknown yet and there is still a lack of research on this. It is known that Nb-STO is a good thermoelectrical material[141], which is very different from LSAT or the undoped STO. Thermoelectrics material has the property that the temperature difference on two sides of the material would lead to voltage difference[147]. In the case of thin film depositions, the bottom side of the substrate is sticking on the heater surface using silver paint, while the upper side of the substrate is the surface where thin film grows. Due to the temperature gradient between the bottom side which is in contact with the heater and the top side of the substrate, a slight voltage difference may be built up between the two sides of the substrate. During deposition, both anions and cations exist in the plume species[96]. A charged substrate would undoubtedly alter the preference of the sequence of charged particles on substrate. In the case of Sr_2RuO_4, Sr^{2+} and Ru^{4+} are positively charged with different amount of charges, while O^{2-} is negatively charged. This way, the growth of Sr_2RuO_4 thin films can be mediated by the appearance of the charged substrate, which help organize the growth sequence and avoid defect growth. However, further study needs to be developed to further verify and understand the growth mechanism of Sr_2RuO_4 films. A study of other superconducting films grown on Nb-STO substrate revealed that Nb-STO offers a flatter and homogeneous surface compared to other insulating substrates, which is necessary for high quality film growth[138, 139].

In my case, Sr_2RuO_4 thin films grown on several substrates were compared: Nb-STO, LSAT, and normal insulating STO. Some correlations between superconductivity and film quality were found. Recalling that rocking curves can be an indicator of how good the transport is for Sr_2RuO_4 thin films in Chapter 6, the FWHM of Sr_2RuO_4 rocking curves on the three substrates were compared here. This is shown in the upper panel of Figure 8.4(c). The difference is obvious: both of the value and range of the FWHM values for Sr_2RuO_4 films on the three different substrates are different. Sr_2RuO_4 films on Nb-STO substrate have smaller FWHM values and narrower range compared to those on STO or LSAT. Therefore, a smaller FWHM value appears to be a

prerequisite for superconductivity in Sr_2RuO_4. In addition, the c-axis values of Sr_2RuO_4 thin films on the three substrates were also investigated. The results were shown in the lower panel in Figure 8.4(c). It is clear that the c-axis value of Sr_2RuO_4 grown on Nb-STO is the closest to that of the single crystal, indicating fewer defects in the film. Therefore, we can say Sr_2RuO_4 films grown on Nb-STO have higher quality than those grown on STO or LSAT. In this sense, superconductivity is more reliably observed.

In summary, the introduction of Nb-STO as a substrate to grow superconducting Sr_2RuO_4 thin films has made obtaining good quality film much easier compared to growing on LSAT. Consistent partial superconductivity has been observed, rather than the localized superconductivity seen on LSAT films. This results undoubtedly opens a whole new chapter of exciting possibilities to not only in the study of superconducting Sr_2RuO_4 thin films growth, but also on the understanding of the superconducting nature of Sr_2RuO_4.

Chapter 9 Conclusions and Future Work

9.1 Conclusions

Sr_2RuO_4 is a very promising candidate to study *p*-wave spin-triplet superconductivity. In addition to the current results on Sr_2RuO_4 single crystals both experimentally and theoretically, much more work needs to be carried out on Sr_2RuO_4 thin films, which could guarantee high quality interfaces or junctions. Therefore, it is very desirable to have a method to consistently grow superconducting Sr_2RuO_4 thin films. This is also the focus of this PhD research.

This thesis covers the understanding of the key pulsed laser deposition parameters and their influences on Sr_2RuO_4 film compositions and transport properties. The study mainly consists of four progressive steps.

The first step was the optimization of c-axis oriented Sr_2RuO_4 thin films using pulsed laser deposition. Sr_2RuO_4 is a member of the Sr-Ru-O series and has a narrow growth window in terms of the deposition parameters. Therefore, it is prone to involuntarily introduce other phases in the series like SrO or $SrRuO_3$ into the films during growth. Clean single phase Sr_2RuO_4 films can be obtained by adjusting the four major deposition parameters including background oxygen pressure, deposition temperature, target to substrate distance, and laser fluence. This step is highly reproducible, as discussed in section 6.1.5.

Secondly, after obtaining the phase pure c-axis oriented Sr_2RuO_4 phase, the transport properties were investigated. Although the earlier c-axis oriented Sr_2RuO_4 thin films were all metal-insulating at low temperatures, some evidence was found showing the connection between the FWHM of the Sr_2RuO_4 (0 0 6) rocking curves and the metal-insulating transition temperatures. Small FWHM values are associated with low metal-insulating transition temperatures, and vice versa. Given the fact that the growth window in terms of the deposition parameters are still wide, fine tuning was

carried out on the four deposition parameters including the oxygen pressure, laser fluence, deposition temperature, and ablation frequency. All these factors are important in improving the film quality in terms of reducing the FWHM of the Sr_2RuO_4 rocking curves, and hence suppressing the metal-insulating transition temperatures of Sr_2RuO_4 thin films. Subsequently, fully metallic Sr_2RuO_4 thin films without metal-insulating transitions were obtained. Similar to first step, this step is also reproducible as long as the growth parameters fall into the narrow range as discussed.

Thirdly, during the fine tuning process, localized superconductivity was also observed in my Sr_2RuO_4 metallic thin films grown on LSAT substrates. However, no obvious deposition parameters could be used to consistently achieve homogeneous superconductivity in the whole Sr_2RuO_4 thin films. Given the fact that the report of superconducting Sr_2RuO_4 thin film is rare with only one report[14] before this work, the low temperature transport behaviors and the structures of my superconducting Sr_2RuO_4 thin films were investigated. It was found that the superconductivity is localized and has an enhanced T_c. Analysis on the c-axis calculations suggests the existence of stacking faults or intergrowth, which may be responsible for the localized superconductivity. It has been indirectly deduced that defects in superconducting Sr_2RuO_4 thin films are much lower than metallic Sr_2RuO_4 thin films, indicating defect is the main factor which suppresses the consistent and homogeneous emergence of superconductivity in Sr_2RuO_4 thin films. In this step, so far I have not grown any films showing homogeneous superconductivity throughout the film.

Last but not least, Nb doped STO substrate was used to consistently grow partially superconducting Sr_2RuO_4 thin films. We observed that by using 5%wt Nb doped STO as substrate, superconductivity in Sr_2RuO_4 thin films can be consistently and reliably achieved. The T_c onset values ranged from 1.20 K to 1.47 K for films with the thickness from 30 nm to 225 nm. A further comparison of the FWHM in Sr_2RuO_4 (0 0 6) rocking curve grown on several substrates revealed that films grown on Nb-STO has better c-axis alignment. In addition, the c-axis deviation from the standard bulk value for Sr_2RuO_4 films on Nb-STO is smaller than films grown on the other substrates.

Therefore, it can be concluded that Sr_2RuO_4 films grown on Nb-STO substrates have higher quality and this accounts for the consistency in transport properties of the superconducting Sr_2RuO_4 thin films.

In summary, partially superconducting Sr_2RuO_4 thin films have been consistently and reliably grown by pulsed laser deposition. Although there is still a lot of work need to be further carried on, this result of no doubt opens up a whole new chapter of interesting possibilities that can be further explored in relation to superconductivity in Sr_2RuO_4 thin films, which is briefly discussed in the next section.

9.2 Future Work

The consistent growth of superconducting Sr_2RuO_4 thin films by pulsed laser deposition will no doubt bring a huge step forward to a more complete understanding of Sr_2RuO_4 itself, and more importantly, towards an in-depth understanding and completion of the exotic superconductivity theories, that have puzzled scientists for a long time. Progressive work can be done based on superconducting Sr_2RuO_4 thin films.

Firstly, although superconducting Sr_2RuO_4 thin films can be consistently grown as demonstrated in this thesis, it is very interesting to understand the growth mechanism of superconducting Sr_2RuO_4 thin films on Nb-STO substrate as compared to other substrates. This may lead to a systematic way of substrate selection for superconducting Sr_2RuO_4 thin film growth.

Secondly, there have been several reports [90, 136, 137] on the pressure or strain effect on the T_c enhancement on Sr_2RuO_4 single crystals. However, due to the disadvantages of Sr_2RuO_4 single crystals as described in Chapter 1, neither Sr_2RuO_4 single crystal selection nor strain orientation can be easily realized[84]. It is very interesting to grow superconducting Sr_2RuO_4 thin films on different substrates with different lattice parameters and conduct a systematic study on the strain effect on superconductivity in Sr_2RuO_4. By taking advantage of the lattice mismatch between film and different substrates, strain is naturally induced in the Sr_2RuO_4 thin films. In this way, the consequent strain effect on the T_c enhancement and whether this can change their electronic structures can be measured and studied.

Thirdly, because the superconductivity of Sr_2RuO_4 is extremely sensitive to structural disorders, besides the XRD analysis done in this work, it would be interesting to systematically study the microstructures of Sr_2RuO_4 thin films using TEM. By using TEM, it would be possible to detect localized structural disorders which otherwise cannot be detected using XRD. In addition, the elemental analysis or chemical characterization of the thin films can be performed on Energy-dispersive X-ray spectroscopy (EDS) or Rutherford backscattering spectrometry (RBS). Thus,

combining the microstructures and the chemical composition analysis can provide a better understanding of the superconducting Sr_2RuO_4 thin films.

Fourthly, it is very interesting to repeat some of the previous junctions made on single crystal Sr_2RuO_4 using superconducting Sr_2RuO_4 films, the results of which were once clouded by the presence of Ru or a poor interface. Moreover, junctions are not limited to the previous ones. More junctions using superconducting Sr_2RuO_4 films can be made to settle the disputes behind the spin triplet superconductivity[11].

Last but not least, it is known that spin triplet pairing can be induced at the interface between a spin singlet superconductor and a ferromagnet by some magnetic inhomogeneity[43]. Now with the ease of superconducting Sr_2RuO_4 film, which is a spin triplet superconductor, the effort to fabricate magnetic inhomogeneity can be dramatically reduced. For instance, it will be straightforward to fabricate Sr_2RuO_4 films and other ferromagnetic layers to see the long range proximity effect.

Apart from the aforementioned possibilities, there are many more exciting experiments that can be done not only on superconducting Sr_2RuO_4 thin films, but also on fully metallic Sr_2RuO_4 thin films, which will help to improve the understanding of Sr_2RuO_4.

Reference

[1] K. Ishida, H. Mukuda, Y. Kitaoka, K. Asayama, Z. Mao, Y. Mori, Y. Maeno, Nature 1998, 396, 658.

[2] R. Jin, Y. Liu, Z. Mao, Y. Maeno, Europhysics Letters 2000, 51, 341.

[3] Y. Maeno, S. Kittaka, T. Nomura, S. Yonezawa, K. Ishida, Journal of the Physical Society of Japan 2011, 81, 011009.

[4] A. P. Mackenzie, Y. Maeno, Reviews of Modern Physics 2003, 75, 657.

[5] G. Luke, Y. Fudamoto, K. Kojima, M. Larkin, J. Merrin, B. Nachumi, Y. Uemura, Y. Maeno, Z. Mao, Y. Mori, Nature 1998, 394, 558.

[6] R. Jin, Y. Zadorozhny, Y. Liu, D. Schlom, Y. Mori, Y. Maeno, Physical Review B 1999, 59, 4433.

[7] Z. Mao, Y. Maenoab, H. Fukazawa, Materials research bulletin 2000, 35, 1813.

[8] Y. Maeno, T. Ando, Y. Mori, E. Ohmichi, S. Ikeda, S. NishiZaki, S. Nakatsuji, Physical review letters 1998, 81, 3765.

[9] A. Damascelli, D. Lu, K. Shen, N. Armitage, F. Ronning, D. Feng, C. Kim, Z.-X. Shen, T. Kimura, Y. Tokura, Physical review letters 2000, 85, 5194.

[10] R. Matzdorf, Z. Fang, J. Zhang, T. Kimura, Y. Tokura, K. Terakura, E. Plummer, Science 2000, 289, 746.

[11] K. Nelson, Z. Mao, Y. Maeno, Y. Liu, Science 2004, 306, 1151.

[12] A. Haghiri-Gosnet, J. Renard, Journal of Physics D: Applied Physics 2003, 36, R127.

[13] F. Lichtenberg, A. Catana, J. Mannhart, D. Schlom, Applied Physics Letters 1992, 60, 1138.

[14] Y. Krockenberger, M. Uchida, K. S. Takahashi, M. Nakamura, M. Kawasaki, Y. Tokura, Applied Physics Letters 2010, 97.

[15] A. Mackenzie, R. Haselwimmer, A. Tyler, G. Lonzarich, Y. Mori, S. Nishizaki, Y. Maeno, Physical review letters 1998, 80, 161.

[16] T. Akima, S. NishiZaki, Y. Maeno, Journal of the Physical Society of Japan

1999, 68, 694.

[17] M. A. Zurbuchen, Y. F. Jia, S. Knapp, A. H. Carim, D. G. Schlom, L. N. Zou, Y. Liu, Applied Physics Letters 2001, 78, 2351.

[18] S. Madhavan, D. G. Schlom, A. Dabkowski, H. A. Dabkowska, Y. Liu, Applied Physics Letters 1996, 68, 559.

[19] J. F. Annett, *Superconductivity, superfluids and condensates*, Vol. 5, Oxford University Press, 2004.

[20] W. Meissner, R. Ochsenfeld, Naturwissenschaften 1933, 21, 787.

[21] M. Tinkham, *Introduction to superconductivity*, Courier Corporation, 1996.

[22] M. Cyrot, D. Pavuna, *Introduction to superconductivity and high-Tc materials*, World Scientific, 1992.

[23] A. Pippard, "An experimental and theoretical study of the relation between magnetic field and current in a superconductor", presented at *Proceedings of the Royal Society of London A: Mathematical, Physical and Engineering Sciences*, 1953.

[24] W. Buckel, *Superconductivity, Fundamentals and applications*, Wiley, 1984.

[25] J. Bardeen, L. N. Cooper, J. R. Schrieffer, Physical Review 1957, 108, 1175.

[26] L. N. Cooper, Physical Review 1956, 104, 1189.

[27] L. P. Gor'kov, Sov. Phys. JETP 1959, 9, 1364.

[28] J. G. Bednorz, K. A. Müller, Zeitschrift für Physik B Condensed Matter 1986, 64, 189.

[29] G. Stewart, Z. Fisk, J. Willis, J. Smith, in *Ten Years of Superconductivity: 1980–1990*, Springer, 1984, 85.

[30] B. Powell, R. H. McKenzie, Journal of Physics: Condensed Matter 2006, 18, R827.

[31] Y. Maeno, H. Hashimoto, K. Yoshida, S. Nishizaki, T. Fujita, J. Bednorz, F. Lichtenberg, Nature 1994, 372, 532.

[32] Y. Kamihara, T. Watanabe, M. Hirano, H. Hosono, Journal of the American Chemical Society 2008, 130, 3296.

[33] H. Tou, Y. Kitaoka, K. Asayama, N. Kimura, Y. Ōnuki, E. Yamamoto, K.

Maezawa, Physical review letters 1996, 77, 1374.

[34] H. Tou, Y. Kitaoka, K. Ishida, K. Asayama, N. Kimura, E. Yamamoto, Y. Haga, K. Maezawa, Physical review letters 1998, 80, 3129.

[35] J. Chipman, Metallurgical Transactions 1972, 3, 55.

[36] H. K. D. H. Bhadeshia, I. O. Materials, *Bainite in steels*, Inst. of Metals, 1992.

[37] J. F. Annett, Contemporary Physics 1995, 36, 423.

[38] R. M. Bozorth, Ferromagnetism, by Richard M. Bozorth, pp. 992. ISBN 0-7803-1032-2. Wiley-VCH, August 1993. 1993, 992.

[39] R. Keizer, S. Goennenwein, T. Klapwijk, G. Miao, G. Xiao, A. Gupta, Nature 2006, 439, 825.

[40] J. Linder, J. W. Robinson, Nature Physics 2015, 11, 307.

[41] M. Anwar, F. Czeschka, M. Hesselberth, M. Porcu, J. Aarts, Physical Review B 2010, 82, 100501.

[42] F. Bergeret, A. Volkov, K. Efetov, Physical review letters 2001, 86, 4096.

[43] J. Robinson, J. Witt, M. Blamire, Science 2010, 329, 59.

[44] J. J. Randall, R. Ward, Journal of the American Chemical Society 1959, 81, 2629.

[45] F. Lichtenberg, Progress in solid state chemistry 2002, 30, 103.

[46] T. Rice, M. Sigrist, Journal of Physics: Condensed Matter 1995, 7, L643.

[47] D. G. Schlom, S. B. Knapp, S. Wozniak, L. N. Zou, J. Park, Y. Liu, M. E. Hawley, G. W. Brown, A. Dabkowski, H. A. Dabkowska, R. Uecker, P. Reiche, Superconductor Science and Technology 1997, 10, 891.

[48] P. Allen, H. Berger, O. Chauvet, L. Forro, T. Jarlborg, A. Junod, B. Revaz, G. Santi, Physical Review B 1996, 53, 4393.

[49] S. Grigera, R. Perry, A. Schofield, M. Chiao, S. Julian, G. Lonzarich, S. Ikeda, Y. Maeno, A. Millis, A. Mackenzie, Science 2001, 294, 329.

[50] M. Crawford, R. Harlow, W. Marshall, Z. Li, G. Cao, R. Lindstrom, Q. Huang, J. Lynn, Physical Review B 2002, 65, 214412.

[51] M. Udagawa, T. Minami, N. Ogita, Y. Maeno, F. Nakamura, T. Fujita, J.

Bednorz, F. Lichtenberg, Physica B: Condensed Matter 1996, 219, 222.

[52] S. Nishizaki, Y. Maeno, T. Fujita, Journal of the Physical Society of Japan 1996, 65, 1876.

[53] J. Routbort, S. Rothman, Journal of applied physics 1994, 76, 5615.

[54] J. Tallon, C. Bernhard, H. Shaked, R. Hitterman, J. Jorgensen, Physical Review B 1995, 51, 12911.

[55] R. Cava, B. Batlogg, C. Chen, E. Rietman, S. Zahurak, D. Werder, Nature 1987, 329, 423.

[56] S. Tozer, A. Kleinsasser, T. Penney, D. Kaiser, F. Holtzberg, Physical review letters 1987, 59, 1768.

[57] S. Martin, A. Fiory, R. Fleming, L. Schneemeyer, J. Waszczak, Physical review letters 1988, 60, 2194.

[58] N. Hussey, A. Mackenzie, J. Cooper, Y. Maeno, S. Nishizaki, T. Fujita, Physical Review B 1998, 57, 5505.

[59] Y. Maeno, K. Yoshida, H. Hashimoto, S. Nishizaki, S.-i. Ikeda, M. Nohara, T. Fujita, A. P. Mackenzie, N. E. Hussey, J. G. Bednorz, Journal of the Physical Society of Japan 1997, 66, 1405.

[60] Z. Mao, Y. Mori, Y. Maeno, Physical Review B 1999, 60, 610.

[61] S. NishiZaki, Y. Maeno, Z. Mao, Journal of Low Temperature Physics 1999, 117, 1581.

[62] K. Yoshida, Y. Maeno, S. Nishizaki, T. Fujita, Physica C: Superconductivity 1996, 263, 519.

[63] H. Suderow, J. Brison, J. Flouquet, A. Tyler, Y. Maeno, Journal of Physics: Condensed Matter 1998, 10, L597.

[64] A. Mackenzie, S. Julian, A. Diver, G. McMullan, M. Ray, G. Lonzarich, Y. Maeno, S. Nishizaki, T. Fujita, Physical review letters 1996, 76, 3786.

[65] A. Abrikosov, Soviet Phys. JETP 12 1961, 1243.

[66] Y. Inoue, M. Hara, Y. Koyama, Y. Maeno, T. Fujita, in *Advances in Superconductivity VIII*, Springer, 1996, 243.

[67] S. NishiZaki, Y. Maeno, Z. Mao, Journal of the Physical Society of Japan 2000, 69, 572.

[68] I. Bonalde, B. D. Yanoff, M. Salamon, D. Van Harlingen, E. Chia, Z. Mao, Y. Maeno, Physical review letters 2000, 85, 4775.

[69] K. Ishida, H. Murakawa, H. Mukuda, Y. Kitaoka, Z. Mao, Y. Maeno, Journal of Physics and Chemistry of Solids 2008, 69, 3108.

[70] L. Hebel, C. P. Slichter, Physical Review 1959, 113, 1504.

[71] J. Xia, Y. Maeno, P. T. Beyersdorf, M. Fejer, A. Kapitulnik, Physical review letters 2006, 97, 167002.

[72] D. Van Harlingen, Reviews of Modern Physics 1995, 67, 515.

[73] C. Tsuei, J. Kirtley, Reviews of Modern Physics 2000, 72, 969.

[74] Y. Liu, New Journal of Physics 2010, 12, 075001.

[75] W. Tian, J. Haeni, D. Schlom, E. Hutchinson, B. Sheu, M. Rosario, P. Schiffer, Y. Liu, M. Zurbuchen, X. Pan, Applied Physics Letters 2007, 90, 022507.

[76] J. Cao, D. Massarotti, M. Vickers, A. Kursumovic, A. Di Bernardo, J. Robinson, F. Tafuri, J. MacManus-Driscoll, M. Blamire, Superconductor Science and Technology 2016, 29, 095005.

[77] D. G. Schlom, Y. Jia, L. N. Zou, J. H. Hanei, S. Briczinski, M. A. Zurbuchen, C. W. Leitz, S. Madhavan, S. Wozniak, Y. Liu, M. E. Hawley, G. W. Brown, A. Dabkowski, H. A. Dabkowska, R. Uecker, P. Reiche, Superconducting and Related Oxides: Physics and Nanoengineering III 1998, 3481, 226.

[78] M. A. Zurbuchen, Y. F. Jia, S. Knapp, A. H. Carim, D. G. Schlom, X. Q. Pan, Applied Physics Letters 2003, 83, 3891.

[79] D. Reisinger, B. Blass, J. Klein, J. B. Philipp, M. Schonecke, A. Erb, L. Alff, R. Gross, Applied Physics a-Materials Science & Processing 2003, 77, 619.

[80] T. Ohnishi, K. Takada, Applied Physics Express 2011, 4.

[81] Y. Takahashi, S. Chakraverty, M. Kawasaki, H. Hwang, Y. Tokura, Physical Review B 2014, 89, 165116.

[82] M. Zurbuchen, W. Tian, X. Pan, D. Fong, S. Streiffer, M. Hawley, J. Lettieri,

Y. Jia, G. Asayama, S. Fulk, Journal of materials research 2007, 22, 1439.

[83] P. Gordon, Mcgraw Hill, New York. 1968, 232 P 1968.

[84] S. Kittaka, H. Taniguchi, S. Yonezawa, H. Yaguchi, Y. Maeno, Physical Review B 2010, 81, 180510.

[85] O. Dix, A. Swartz, R. Zieve, J. Cooley, T. Sayles, M. Maple, Physical review letters 2009, 102, 197001.

[86] C. Campos, J. Brooks, P. Van Bentum, J. Perenboom, S. Klepper, P. Sandhu, S. Valfells, Y. Tanaka, T. Kinoshita, N. Kinoshita, Physical Review B 1995, 52, R7014.

[87] D. Jin, S. Carter, B. Ellman, T. Rosenbaum, D. Hinks, Physical review letters 1992, 68, 1597.

[88] M. Braden, W. Reichardt, S. Nishizaki, Y. Mori, Y. Maeno, Physical Review B 1998, 57, 1236.

[89] S. Kittaka, H. Yaguchi, Y. Maeno, Journal of the Physical Society of Japan 2009, 78, 103705.

[90] C. W. Hicks, D. O. Brodsky, E. A. Yelland, A. S. Gibbs, J. A. Bruin, M. E. Barber, S. D. Edkins, K. Nishimura, S. Yonezawa, Y. Maeno, Science 2014, 344, 283.

[91] D. L. Smith, *Thin-film deposition: principles and practice*, Vol. 108, McGraw-Hill New York etc, 1995.

[92] M. Ohring, *Materials science of thin films*, Academic press, 2001.

[93] J. Venables, G. Spiller, M. Hanbucken, Reports on Progress in Physics 1984, 47, 399.

[94] J.-H. Park, T. Sudarshan, *Chemical vapor deposition*, Vol. 2, ASM international, 2001.

[95] R. Eason, *Pulsed laser deposition of thin films: applications-led growth of functional materials*, John Wiley & Sons, 2007.

[96] D. B. Chrisey, G. K. Hubler, *Pulsed laser deposition of thin films*, Wiley-Blackwell, 1994.

[97] S. Li, E. Arenholz, J. Heitz, D. Bäuerle, Applied Surface Science 1998, 125, 17.

[98] H. Zeng, W. R. Lacefield, Biomaterials 2000, 21, 23.

[99] H. Tabata, H. Tanaka, T. Kawai, Applied physics letters 1994, 65, 1970.

[100] Y. E. Lee, C. M. Rouleau, C. Park, D. P. Norton, MRS Online Proceedings Library Archive 1999, 560.

[101] L. You, N. T. Chua, K. Yao, L. Chen, J. Wang, Physical Review B 2009, 80, 024105.

[102] D. H. Lowndes, D. Geohegan, A. Puretzky, D. Norton, C. Rouleau, Science 1996, 273, 898.

[103] J. Zheng, H. S. Kwok, Applied physics letters 1993, 63, 1.

[104] R. Castro-Rodriguez, D. R. Coronado, A. Iribarren, B. Watts, F. Leccabue, J. Pena, Applied Physics A 2005, 81, 1503.

[105] A. Mostako, A. Khare, Applied Nanoscience 2012, 2, 189.

[106] A. K. Panda, A. Singh, M. Mishra, R. Thirumurugesan, P. Kuppusami, E. Mohandas, Laser and Particle Beams 2014, 32, 429.

[107] S. Wicklein, A. Sambri, S. Amoruso, X. Wang, R. Bruzzese, A. Koehl, R. Dittmann, Applied physics letters 2012, 101, 131601.

[108] H. Kim, H. S. Kwok, Applied Physics Letters 1992, 61, 2234.

[109] H. S. Kwok, H. Kim, D. Kim, W. Shen, X. Sun, R. Xiao, Applied surface science 1997, 109, 595.

[110] S.-M. Park, T. Ikegami, K. Ebihara, Thin Solid Films 2006, 513, 90.

[111] D. Geohegan, D. Mashburn, R. Culbertson, S. Pennycook, J. Budai, R. Valiga, B. Sales, D. Lowndes, L. Boatner, E. Sonder, Journal of Materials Research 1988, 3, 1169.

[112] M. Yeh, K. Liu, I. Lin, Thin solid films 1995, 258, 82.

[113] M. Lippmaa, N. Nakagawa, M. Kawasaki, S. Ohashi, H. Koinuma, Applied Physics Letters 2000, 76, 2439.

[114] D. Montiel, J. Müller, E. C. Poiré, Journal of Physics: Condensed Matter 2001, 14, L49.

[115] B. D. Cullity, *Elements of X-ray Diffraction*, Pearson, 2001.

[116] M. Vickers, X-ray and Neutron Diffraction Methods, http://intranet.msm.cam.ac.uk/xray/camonly/Grad_Xray_Lectures_3- 8_Handout_FINAL.pdf. 2017.

[117] P. F. Fewster, Reports on Progress in Physics 1996, 59, 1339.

[118] P. Eaton, P. West, *Atomic force microscopy*, Oxford University Press, 2010.

[119] I. Horcas, R. Fernández, J. Gomez-Rodriguez, J. Colchero, J. Gómez-Herrero, A. Baro, Review of Scientific Instruments 2007, 78, 013705.

[120] O. Chmaissem, J. Jorgensen, H. Shaked, S. Ikeda, Y. Maeno, Physical Review B 1998, 57, 5067.

[121] B. Chakoumakos, D. Schlom, M. Urbanik, J. Luine, Journal of Applied Physics 1998, 83, 1979.

[122] C. Mallika, O. Sreedharan, Journal of alloys and compounds 1993, 191, 219.

[123] S. Saito, K. Kuramasu, Japanese journal of applied physics 1992, 31, 135.

[124] M. Tyunina, J. Levoska, S. Leppävuori, Journal of applied physics 1998, 83, 5489.

[125] M. Pley, M. S. Wickleder, Journal of Solid State Chemistry 2005, 178, 3206.

[126] R. J. Kline, M. D. McGehee, M. F. Toney, Nature Materials 2006, 5, 222.

[127] P. K. Nayak, L. Barnea-Nehoshtan, R. S. Kim, A. Shu, G. Man, A. Kahn, D. Lederman, Y. Feldman, D. Cahen, Energy & Environmental Science 2013, 6, 3272.

[128] A. Ojeda-GP, C. W. Schneider, M. Döbeli, T. Lippert, A. Wokaun, Applied surface science 2015, 336, 150.

[129] F. Sánchez, C. Ocal, J. Fontcuberta, Chemical Society Reviews 2014, 43, 2272.

[130] J. H. Ngai, T. C. Schwendemann, A. E. Walker, Y. Segal, F. J. Walker, E. I. Altman, C. H. Ahn, Advanced Materials 2010, 22, 2945.

[131] Y. Ying, N. Staley, Y. Xin, K. Sun, X. Cai, D. Fobes, T. Liu, Z. Mao, Y. Liu, Nature communications 2013, 4.

[132] J. S. Kasper, *International Tables for X-ray Crystallography. Vol. 2. Mathematical Tables*, Kynoch P XIX, 1972.

[133] C. Cancellieri, P. Lin, D. Ariosa, D. Pavuna, Physical Review B 2007, 76,

174520.

[134] A. Iyo, Y. Tanaka, Y. Kodama, H. Kito, K. Tokiwa, T. Watanabe, Physica C: Superconductivity and its applications 2006, 445, 17.

[135] T. Ohnishi, K. Shibuya, T. Yamamoto, M. Lippmaa, Journal of Applied Physics 2008, 103, 103703.

[136] Y.-T. Hsu, W. Cho, A. F. Rebola, B. Burganov, C. Adamo, K. M. Shen, D. G. Schlom, C. J. Fennie, E.-A. Kim, Physical Review B 2016, 94, 045118.

[137] B. Burganov, C. Adamo, A. Mulder, M. Uchida, P. King, J. Harter, D. Shai, A. Gibbs, A. Mackenzie, R. Uecker, Physical review letters 2016, 116, 197003.

[138] J.-F. Ge, Z.-L. Liu, C. Liu, C.-L. Gao, D. Qian, Q.-K. Xue, Y. Liu, J.-F. Jia, Nature materials 2015, 14, 285.

[139] Y. Sun, W. Zhang, Y. Xing, F. Li, Y. Zhao, Z. Xia, L. Wang, X. Ma, Q.-K. Xue, J. Wang, Scientific reports 2014, 4.

[140] J. Karczewski, B. Riegel, M. Gazda, P. Jasinski, B. Kusz, Journal of Electroceramics 2010, 24, 326.

[141] S. Ohta, T. Nomura, H. Ohta, K. Koumoto, Journal of applied physics 2005, 97, 034106.

[142] K. P. McKenna, F. Hofer, D. Gilks, V. K. Lazarov, C. Chen, Z. Wang, Y. Ikuhara, Nature Communications 2014, 5.

[143] D. Gilks, L. Lari, J. Naughton, O. Cespedes, Z. Cai, A. Gerber, S. Thompson, K. Ziemer, V. Lazarov, Journal of Physics: Condensed Matter 2013, 25, 485004.

[144] C. Koonce, M. L. Cohen, J. Schooley, W. Hosler, E. Pfeiffer, Physical Review 1967, 163, 380.

[145] E. Pfeiffer, J. Schooley, Physics Letters A 1969, 29, 589.

[146] E. Ambler, J. Colwell, W. Hosler, J. Schooley, Physical Review 1966, 148, 280.

[147] H. J. Goldsmid, *Introduction to thermoelectricity*, Vol. 121, Springer, 2010.

Appendix I Thickness Calculation and Experimental Errors

An example of how thin film thickness and errors are calculated is given below:

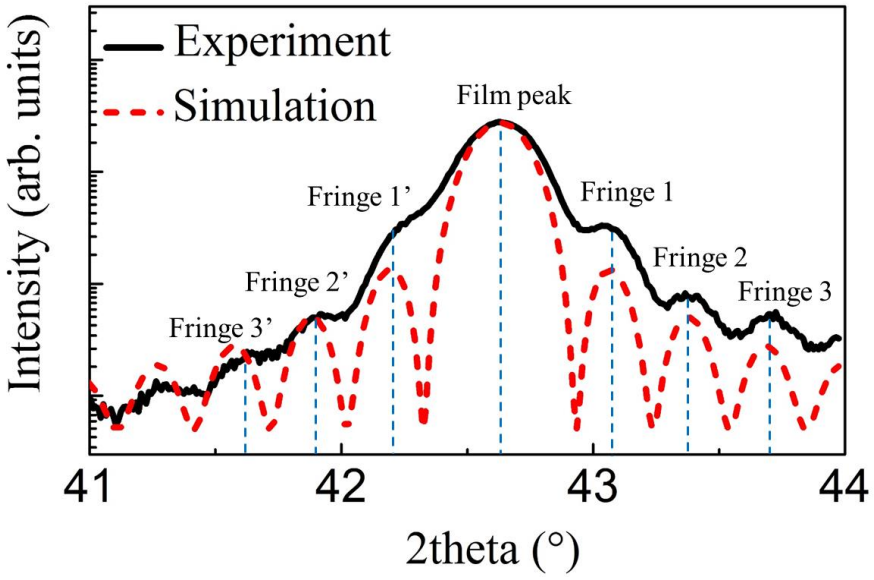

Figure A1 Thickness fringes of a sample and the simulation result based on the experimental data. The blue dashed lines marked both the film peak and the fringes in the experimental data.

As already discussed in Chapter 5, film thickness can be calculated by measuring the period distance between two adjacent fringes, and use the following equation:

$$thickness = \frac{\lambda}{2\Delta\theta * cos\theta} \quad (1)$$[115].

In experimental data, the fringe periods are not evenly spaced due to random variations. Therefore, there is a slight difference between the fringe periods. The result is shown in Table A1, where each fringe period corresponds to a calculated thickness value. The thickness of the sample is taken as the average value of the four values of fringe spacing, whereas the error of the thickness is taken as the absolute error of the data (e.g. by subtracting the highest and lowest thickness values in the table) which gives an average thickness of about 30 nm with an error of about ± 2 nm, rounded to the nearest integer.

In addition, the simulation also gives the result of about 30 nm, matches well with the experimental result.

It has to be mentioned that in this method, we used adjacent fringes spacing instead of the overall spacing of all the fringes, say, Fringe 3' to Fringe 3 in this case. The reason for this is that the overall spacing of all the fringes include the film peak, which cannot be considered as a fringe peak. Equation (1) is only valid when the spacing is between two fringe peaks. Therefore, using individual fringe peak spacing is more preferable in this case.

Adjacent Fringes	Fringe period (°)	Calculated thickness (nm)
Fringe 3' to Fringe 2'	0.14130	31.863
Fringe 2' to Fringe 1'	0.15660	28.672
Fringe 1 to Fringe 2	0.14783	30.416
Fringe 2 to Fringe 3	0.15293	29.371

Table A1 Fringe period and corresponding thicknesses.

Appendix II Bragg Equation

Possible outcomes of equation (7.3) in Chapter 7 are illustrated in Figure 1.

$$\frac{\Delta d}{d} \propto \frac{cos^2\theta}{sin\theta}$$

1. When there is no sample displacement error, the c-axis or d-spacing calculated from symmetrical 2θ-ω scans is constant – see Figure 1(a).
2. When there is a sample displacement error, which normally occurs due to sample mounting as mentioned in Chapter 7, the c-axis values have a linear dependency on $\cos^2\theta/\sin\theta$, as shown in Figure 1(b). In this case, the relative slope of the linear fitting function for both the film and the substrate are the same.
3. When there is not only a sample displacement error, but also some intergrowth or stacking faults exist in the sample, the layers along the c-axis would be disrupted and therefore cause inconsistency in c-axis values. In Figure 1(c), the linear trend for the substrate does indicate a sample displacement error. However, the c-axis values for the film does not show any correlation with $\cos^2\theta/\sin\theta$. In this case, as illustrated in reference[133], it indicates a sample with intergrowth/stacking faults.

For each of the films, the substrate can be used as a reference for the sample displacement error, and assuming that the main peaks originate from regions of high quality epitaxy, the error should also equivalently affect these film peaks.

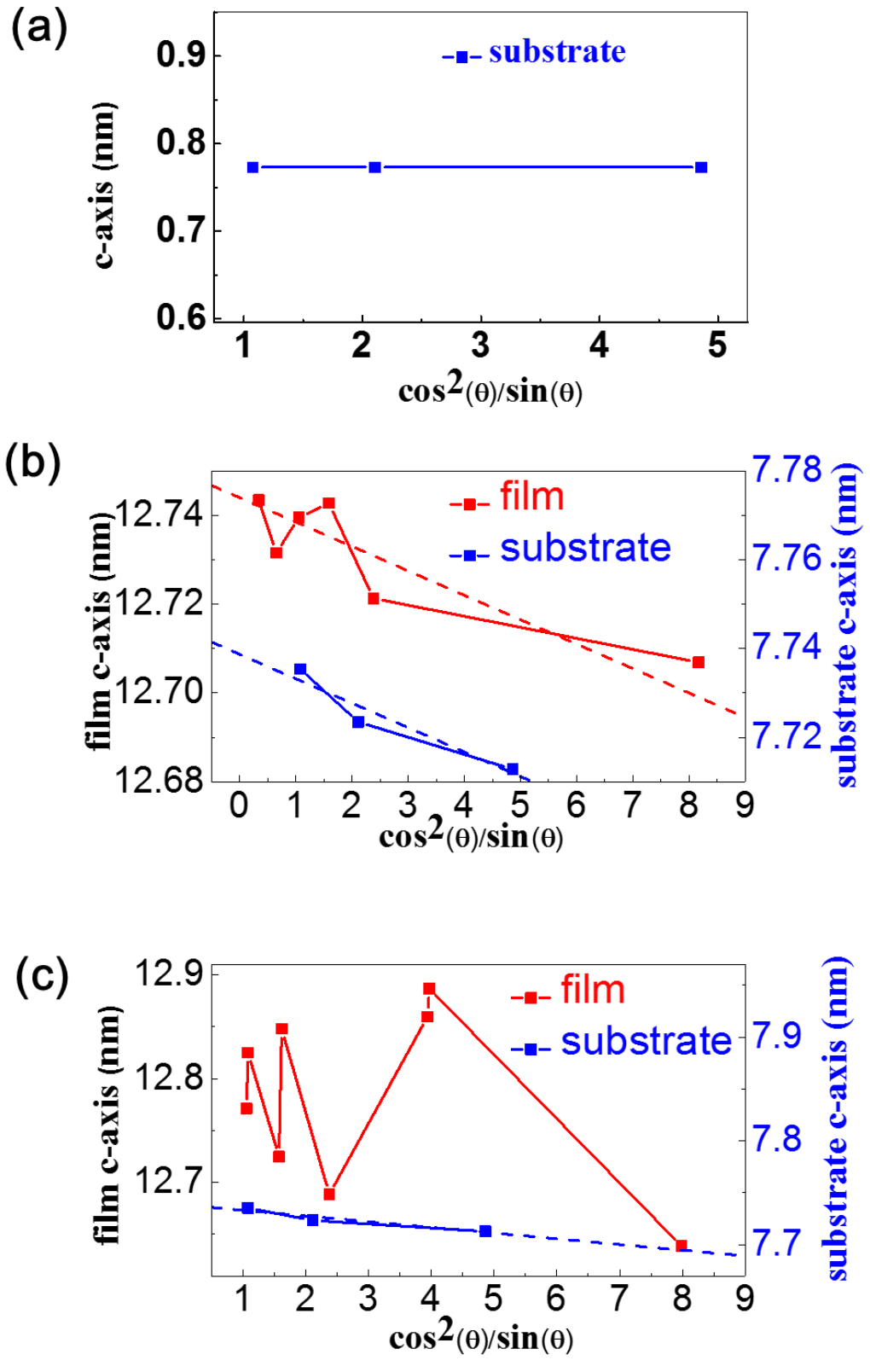

Figure 1. The explanation of the sample height error equation (1). (a) No sample height error. (b) With sample height error. (c) Sample height error with intergrowth/stacking faults within the layers in the film.